

X-ray survey of the North-America and Pelican star-forming complex (NGC7000/IC5070)

Francesco Damiani¹, Ignazio Pillitteri^{1,2}, and Loredana Prisinzano¹

¹ INAF - Osservatorio Astronomico di Palermo G.S.Vaiana, Piazza del Parlamento 1, I-90134 Palermo, Italy
e-mail: damiani@astropa.inaf.it

² Harvard-Smithsonian Center for Astrophysics, 60 Garden St., Cambridge MA 02138 USA.

Received date / Accepted date

ABSTRACT

Aims. We present the first extensive X-ray study of the North-America and Pelican star-forming region (NGC 7000/IC 5070), with the aim of finding and characterizing the young population of this cloud.

Methods. X-ray data from Chandra (four pointings) and XMM-Newton (seven pointings) were reduced and source detection algorithm applied to each image. We complement the X-ray data with optical and near-IR data from the IPHAS, UKIDSS, and 2MASS catalogs, and with other published optical and Spitzer IR data. More than 700 X-ray sources are detected, the majority of which have an optical/NIR counterpart. This allows to identify young stars in different stages of formation.

Results. Less than 30% of X-ray sources are identified with a previously known young star. We argue that most X-ray sources with an optical/NIR counterpart, except perhaps for a few tens at near-zero reddening, are likely candidate members of the star-forming region, on the basis of both their optical/NIR magnitudes and colors, and of X-ray properties like spectrum hardness or flux variations. They are characterized by a wide range of extinction, and sometimes near-IR excesses, both of which prevent derivation of accurate stellar parameters. The optical color-magnitude diagram suggests ages between 1-10 Myrs. The X-ray members have a very complex spatial distribution with some degree of subclustering, qualitatively similar to that of previously known members. The detailed distribution of X-ray sources relative to the objects with IR excesses identified with Spitzer is sometimes suggestive of sequential star formation, especially near the “Gulf of Mexico” region, probably triggered by the O5 star which illuminates the whole region. We confirm that around this latter star no enhancement in the young star density is found, in agreement with previous results. Thanks to the precision and depth of the IPHAS and UKIDSS data used, we also determine the local optical/IR reddening law, and compute an updated reddening map of the entire region.

Key words. Open clusters and associations: individual (NGC7000, IC5070) – stars: pre-main-sequence – X-ray: stars

1. Introduction

The star-formation region associated with the North-America (NGC 7000) and Pelican (IC 5070) Nebulae in Cygnus have received increased attention in the last decades. The two nebulae are catalogued as separate objects because of their visual appearance, but are now commonly regarded as parts of the same physical gas and dust cloud. The properties of the region were reviewed by Reipurth and Schneider (2008). The ionizing source of the nebulae has remained a mystery for decades, but was at last identified with a highly reddened O5 star (2MASS J20555125+4352246, $A_V \sim 9.6$) by Comerón and Pasquali (2005), hidden by the dark dust cloud LDN935, lying between NGC 7000 and IC 5070. This star is remarkably isolated according to these authors: there are no other massive stars close to it, or they would have been easily detected even if highly obscured.

Since the work of Herbig (1958, henceforth H58) it was known that several tens young pre-main-sequence (PMS) stars are found in this region. Welin (1973) presented also an objective-spectra study of emission-line stars in the region, and a few more young stars were studied spectroscopically by Corbally, Straizys and Laugalys (2009). Narrow-band filter studies have also revealed many emission-line star candidates (e.g. Witham et al. 2008, Armond et al. 2011), as well as many Herbig-Haro flows (Bally and Reipurth 2003, Armond et al. 2011, and also Bally et al. 2014). The strong obscuration to-

wards many parts of the cloud undoubtedly prevents many other PMS stars to be found optically, but was no obstacle for the sensitive survey for Young Stellar Objects (YSOs) made with the Spitzer Space Observatory (IRAC camera, Guieu et al. 2009; IRAC+MIPS, Rebull et al. 2011, henceforth RGS11). Cambrésy et al. (2002) also studied this region using 2MASS data, tracing spatial extinction variations, and finding nine clusters of near-IR (NIR) objects.

The distance of the cloud was estimated to be in the range 500-600 pc by Laugalys et al. (2006, 2007). The line of sight towards Cygnus is tangent to the corresponding spiral arm, and therefore objects at vastly different distance from the Sun can appear visually close in the sky: the Cyg OB2 association for example, only a few degrees away from NGC7000, lies at a much larger distance ~ 1.5 kpc. In the direction of the North-America/Pelican (NAP), Straizys, Corbally and Laugalys (2008) find a larger-than-typical $E(J - H)/E(H - K)$ ratio of 2.0.

The NAP region is also known to host two PMS stars in the FU Ori class: V1057 Cyg and V2493 Cyg. This latter was only known as a Classical T Tauri star (CTTS) named HBC722 before its outburst in 2010, and intensively studied thereafter (Semkov et al. 2010, Covey et al. 2011, Aspin 2011, Miller et al. 2011, Green et al. 2011, Kóspál et al. 2011, 2013, Dunham et al. 2012, Semkov et al. 2012, Liebhart et al. 2014, and Lee et al. 2015). V1057 Cyg was observed in X-rays (but not detected) by Skinner

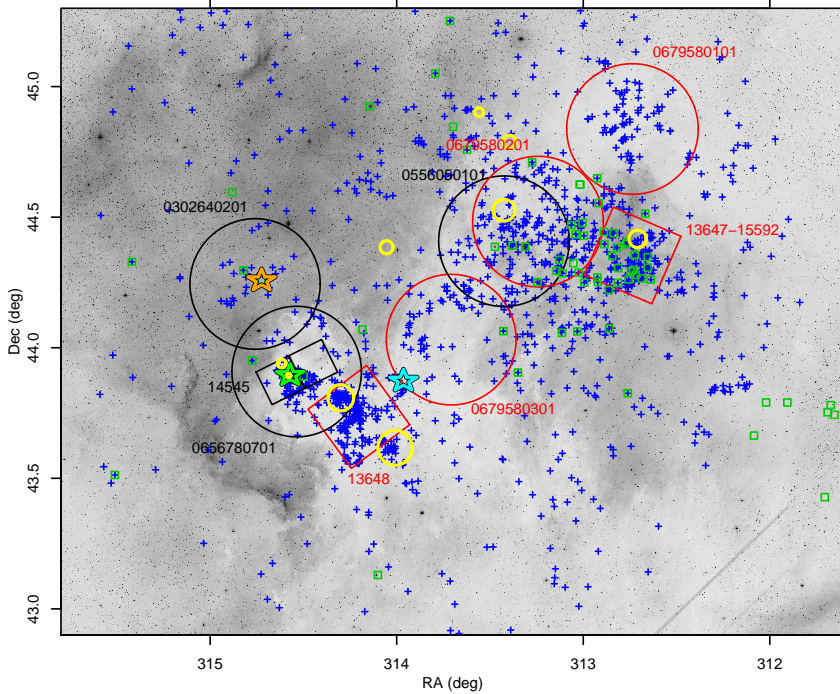


Fig. 1. Digital-Sky-Survey II red image of the North-America and Pelican nebulae (inverted greyscale), with overlaid the regions covered by XMM-Newton observations (big circles), and Chandra ACIS observations (squares), each labeled with its ObsId number. X-ray fields of view are drawn in red for new data, and black for archive data. ACIS-I ObsIds 13467 and 15592 share the same pointing direction and roll angle. Archive XMM ObsIds 0656780701 and 0656781201 also share the same pointing direction, but with a slightly different roll angle; only 0656780701 is labeled in the Figure. Small green squares are the H58 emission-line stars; blue crosses are YSOs from RGS11. Yellow circles indicate positions and approximate sizes of the Cambrésy et al. (2002) clusters of 2MASS NIR sources. The three bigger star symbols indicate respectively the O5 star 2MASS J2055125+4352246 (cyan), the FU Ori object candidate HBC722 (= V2493 Cyg = 2MASS J20581702+4353433, green), and the FU Ori star V1057 Cyg (= 2MASS J20585371+4415283, orange).

et al. (2007), while a positive X-ray detection of V2493 Cyg was presented by Liebhart et al. (2014). No other published X-ray study exists of this region, to our knowledge.

The strong and nonuniform obscuration towards the cloud, and its large size ($\sim 2^\circ$) are formidable difficulties when attempting to characterize the global young-star population of this star-forming region. The Spitzer RGS11 study of YSOs is extremely important in this respect, since it covered basically all the cloud, and was sensitive to even highly obscured objects. Since the selection of YSOs in RGS11 is based on the existence of non-photospheric excess IR emission from circumstellar dust (disks), it is however biased against diskless PMS stars (Class III objects in the SED-based nomenclature, or Weak-line T Tauri stars - WTTS, as opposed to CTTS - in the spectroscopic nomenclature). At typical ages of PMS stars, both CTTS and WTTS are however bright X-ray sources (with X-ray luminosities in the range $\log L_X \sim 29 - 31$ erg/s). Therefore, we have obtained new X-ray observations at selected positions in the NAP Nebula, using both XMM-Newton and Chandra X-ray observatories, with the purpose of obtaining a more complete and unbiased census of the PMS population of this star-forming region. In addition, we analyze here other X-ray datasets from these observatories, which were only partially examined in the published literature.

Moreover, we take advantage of two important wide-area optical and NIR surveys: IPHAS (Drew et al. 2005) and UKIDSS (Lawrence et al. 2007), covering the entire cloud, with limiting magnitudes far deeper than most other optical/NIR catalogues available in the same region.

This paper is structured as follows: Section 2 describes the X-ray data presented, and Section 3 their analysis. Section 4 describes the optical/NIR data also used in this work. Section 5 presents all results obtained. Section 6 is a discussion of the results, and Section 7 summarizes our conclusions.

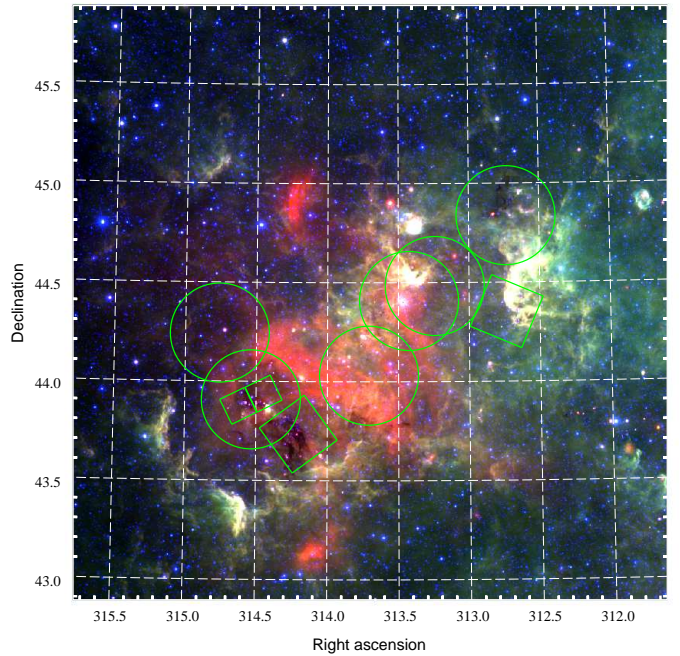


Fig. 2. True-color WISE image of the region. Red: 22μ , green: 12μ , and blue: 4.6μ channels, respectively. The big circles and squares indicates the X-ray FOVs as in Fig. 1. North is up and East to the left. At a distance of 560 pc, the 3-degree sky region shown measures 29.3 pc on a side.

2. X-ray observations

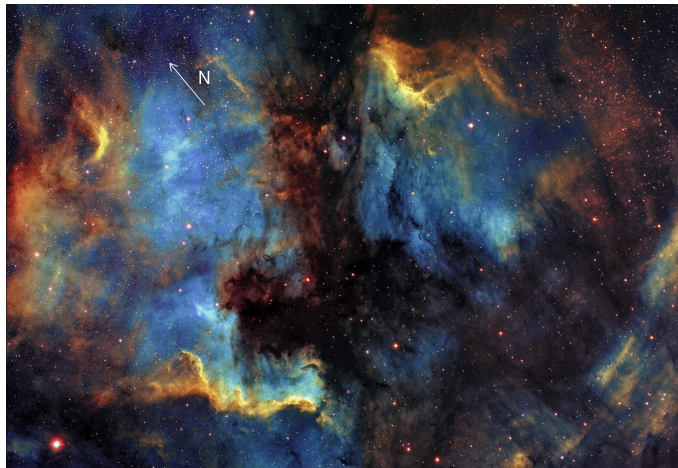
The log of the X-ray observations used in this work is reported in Tables 1 and 2. We obtained three new XMM-Newton EPIC observations and two new Chandra ACIS-I observations (ACIS-I ObsIds 13467 and 15592 are in fact the same observation split in two segments, while 13648 is a distinct pointing). Four archive

Table 1. XMM-Newton observing log. Dates are UT, exposure times t_{exp} in seconds.

ObsId	RA	Dec	PI	PN start date	PN t_{exp}	MOS start date	MOS t_{exp}
0679580101	312.7004	44.85204	Damiani	2011-11-24,00:13:45	25591	2011-11-23,23:51:28	30239
0679580201	313.2083	44.49669	Damiani	2011-11-24,10:32:48	13750	2011-11-24,09:34:44	19092
0679580301	313.6737	44.04564	Damiani	2011-11-24,18:48:44	23827	2011-11-24,18:26:25	28239
0302640201	314.7238	44.25789	Skinner	2005-11-26,21:12:19	21027	2005-11-26,20:50:00	23733
0556050101	313.4454	44.38394	Motch	2008-05-02,11:27:25	14498	2008-05-02,10:58:53	17392
0656780701	314.5710	43.89539	Schartel	2010-11-25,19:29:52	15968	2010-11-25,19:07:30	18237
0656781201	314.5710	43.89539	Schartel	2011-05-26,12:47:35	17560	2011-05-26,12:25:15	21327

Table 2. Chandra observing log. Dates are UT, exposure times t_{exp} in seconds.

ObsId	RA	Dec	PI	Detector	Start date	t_{exp}
13648	314.2114	43.74551	Damiani	ACIS-I	2011-12-26,20:43:50	44588
13647	312.7507	44.35863	Damiani	ACIS-I	2012-11-20,03:37:14	22766
15592	312.7507	44.35863	Damiani	ACIS-I	2012-11-21,17:52:27	20792
14545	314.5673	43.89382	Guedel	ACIS-S	2013-07-17,06:16:36	29677

**Fig. 3.** Optical emission-line image of part of the region (courtesy Ondřej Podlucky), in the lines of [O III] (blue), H α (green) and [S II] (red), showing increasing ionization towards a location behind the obscuring dust. The white arrow indicates North.

XMM-Newton observations are also analyzed (of which ObsIds 0656780701 and 0656781201 nearly co-pointed), as well as one ACIS-S observation; this latter has a different field of view (FOV) than the ACIS-I detector, and a slightly different sensitivity. All XMM-Newton observations, made with the EPIC camera, are composed by a set of three simultaneous observations with the PN, MOS1, and MOS2 detectors, approximately co-pointed but having different FOV shapes; PN is the most sensitive of the three, while the MOS1 (MOS2) effective area is comparable to that of ACIS-I. All XMM-Newton observations were made using the Medium filter. The Chandra ACIS images have an on-axis PSF much narrower (~ 0.5 arcsec) than XMM-Newton EPIC images (~ 4 arcsec): this implies not only a better spatial resolving power, but also that less counts are needed for a significant source detection (~ 4 X-ray counts vs. ~ 40 for the PN+MOS combination) because the background contribution in the EPIC images is usually non-negligible, while it is in ACIS images. Far from optical axis, the PSF degrades sensibly in ACIS images, while that of XMM-Newton images is rather uniform across the FOV.

We tried to optimize our X-ray pointings, guided by the large-scale distribution and local spatial density of YSOs from

Guieu et al. (2009). Therefore, we have chosen ACIS-I where the YSO density was highest, but preferred XMM-Newton with its larger FOV for the sparser regions. Figure 1 shows a Digital-Sky-Survey (DSS) red image of the region, with indicated all the X-ray observations studied here, and also the RGS11 YSOs, and H58 PMS stars; the illuminating O5 star, and the two FU Ori objects are also indicated, as well as the NIR clusters found by Cambrésy et al. (2002). The sub-regions with the highest YSO density are the so-called “Gulf of Mexico”, covered by our ACIS field 13648, and the “Pelican”, covered by our ACIS fields 13647 and 15592. The less-obscured part of the cloud containing V1057 Cyg, covered by XMM-Newton archive ObsId 0302640201, contains only few YSOs.

Besides the studies mentioned above, more evidences can be presented in favour of the North-America and Pelican Nebulae being part of the same cloud; this is especially important in this part of the sky because of the mentioned tangent-arm geometry, and in this particular nebula to ascertain that the foreground obscuring cloud is physically associated with the bright nebulae and is not much closer along the line of sight. For example, the WISE (Wright et al. 2010) images in four NIR bands at 3.4, 4.6, 12, and 22μ demonstrate the presence of dense, hot dust behind the dark nebula LDN935 (Figure 2), with a geometry approximately centered on the illuminating O5 star. The distance of the dark cloud from us is therefore the same as the distance of the bright nebulae obscured by it. The region with the highest YSO density, just S-E of the O5 star and inside our ACIS 13648 field, is also seen in the WISE image to be one of highest obscuration.

The same qualitative conclusion that the North-America and Pelican Nebulae are the same physical cloud is reached by inspecting an optical emission-line image, obtained using narrow-band filters centered at the [O III], H α , and [S II] optical lines, shown in Figure 3. The ionization (highest for [O III]) has a global pattern, centered close to the O5 star; there is no other obvious ionization center, based on the optical-line image.

All X-ray images studied here are shown in Figures 4, 5, and 6. In these true-color images, the red (green, blue) intensity is proportional to detected X-ray counts in the soft (medium, hard) X-ray band. Blue sources are typically highly absorbed objects, with a strong low-energy cutoff in their X-ray spectrum. The Chandra FOVs are indicated, as well as the O5 star and the FU Ori objects.

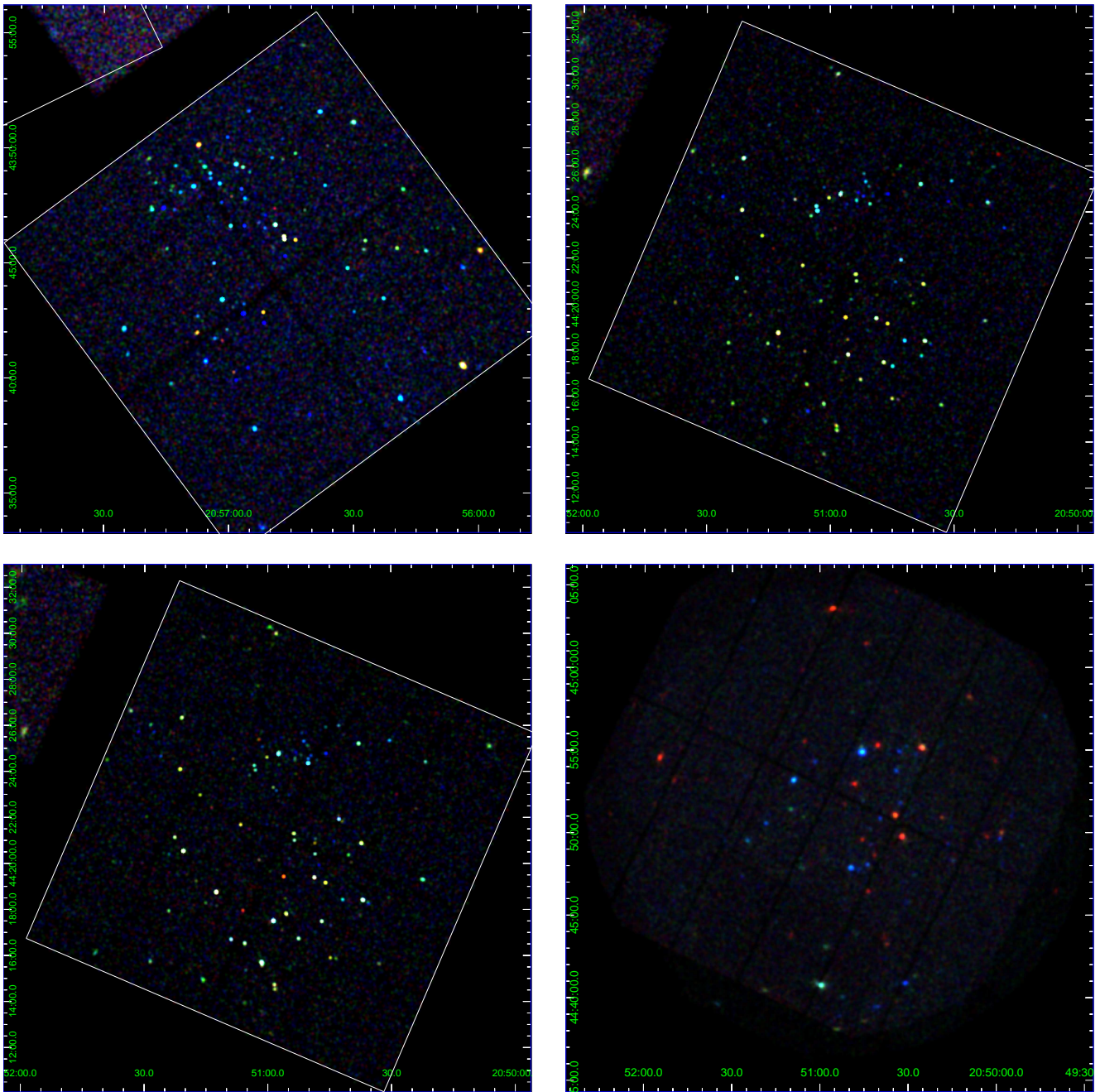


Fig. 4. True-color X-ray images of individual observations, slightly smoothed to emphasize point sources. Red: 0.4-1.2 keV; green: 1.2-2.4 keV; blue: 2.4-7.9 keV. Panel *a*, upper left: ACIS-I ObsId 13648 (in the “Gulf of mexico”). The ACIS-I FOV size is 16.9 arcmin on a side. *b*, upper right: ACIS-I ObsId 13647 (“Pelican”). *c*, lower left: ACIS-I ObsId 15592, with same pointing as ObsId 13647 (panel *b*). Comparison with this latter ObsId makes source variability very evident. *d*, lower right: XMM-Newton ObsId 0679580101 (“Pelican hat”). In all XMM-Newton images shown here, MOS1,2 and PN data are combined together.

3. X-ray data analysis

The X-ray datasets were processed using standard software packages (CIAO v4.8 for Chandra and SAS v11 for XMM-Newton data), and exposure maps at a representative energy of 1 keV were computed using the same packages. Source detection was made using PWXdetect (v1.3.2) for Chandra data, and its XMM-Newton analogue PWXdetect (Damiani et al. 1997a,b). The front- and back-illuminated chips of ACIS-S ObsId 14545 were analyzed separately. ACIS-I ObsIds 13647 and 15592, sharing the same pointing direction and roll angle, were

only analyzed jointly. This was also the case for archive XMM ObsIds 0656780701 and 0656781201. Spurious detections associated with diffraction spikes or out-of-time events (Fig. 5, panel *a*; Fig. 6, panel *a*) were manually eliminated. We then merged all individual X-ray detection lists according to computed position errors, separately for XMM-Newton and Chandra, giving priority to highest-significance detections. Thus, each detected X-ray source receives its IAU-recommended instrument-specific designation. The match and merging of XMM-Newton and Chandra detection lists was made in a subsequent step, taking in mind the much better spatial resolution of this latter, and therefore giving

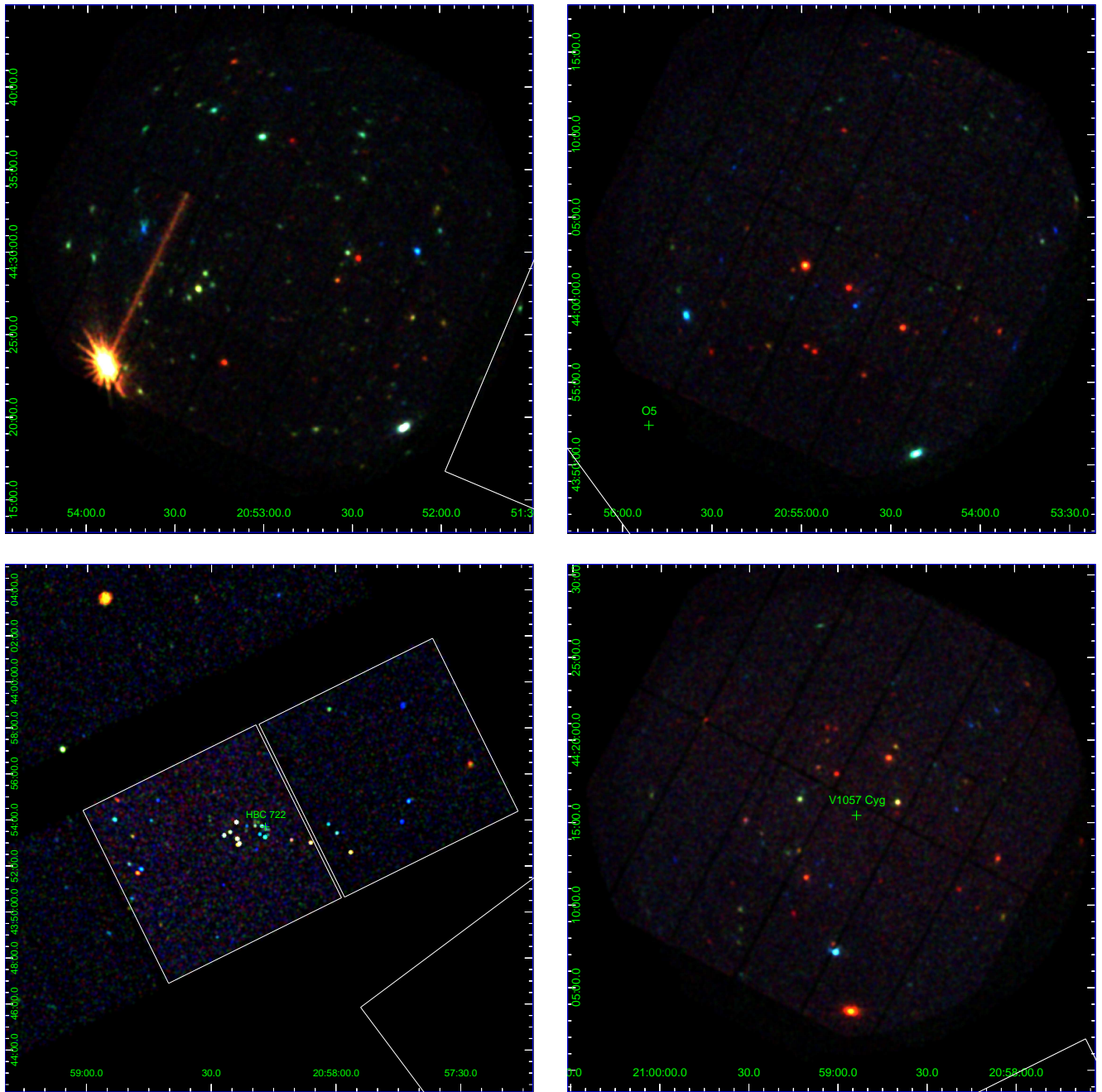


Fig. 5. X-ray images as in Fig. 4. Panel *a*, upper left: XMM-Newton ObsId 0679580201. The brightest source (2XMM J205347.0+442301) (classified as a star by Lin et al. 2012) produces both diffraction spikes and a stripe of out-of-time events, accumulated during CCD readout. The white line outlines the eastern part of ACIS ObsId 13647 FOV. *b*, upper right: XMM-Newton ObsId 0679580301, towards the highly obscured region LDN 935. The plus sign labeled “O5” is the O star 2MASS J20555125+4352246 from Comerón and Pasquali (2005). *c*, lower left: Archive ACIS-S ObsId 14545. The two white squares indicate ACIS-S chips 6 (front-illuminated, right) and 7 (back-illuminated, left), which have different sensitivities and are analyzed separately. This ObsId also has data from chips 2, 3, and 8, shown in the same Figure; however the sensitivity and/or spatial resolution of these chips is inferior, and they are not considered further here. Near the center of the image, the green plus sign indicates the new FU Ori candidate HBC 722. To the SW a part of ACIS 13648 FOV can be seen. *d*, lower right: Archive XMM-Newton ObsId 0302640201, just north of ACIS-S ObsId 14545 (seen in lower-right corner). Near image center the FU Ori star V1057 Cyg is labeled.

priority to the Chandra source positions and properties in ambiguous cases (see e.g. the tight group of sources near HBC 722 in Fig. 5, panel *c*, which is unresolved by XMM-Newton in Fig. 6, panel *b*). The final X-ray source list comprises 721 objects, of which 378 ACIS detections (of which 34 with an XMM-Newton counterpart), and 343 XMM-Newton-only detections. The chosen detection threshold, corresponding to approximately

one spurious detection per field, ensures that no more than ~ 10 of the 721 detections are spurious. The positions of all X-ray detections are shown in Figure 7.

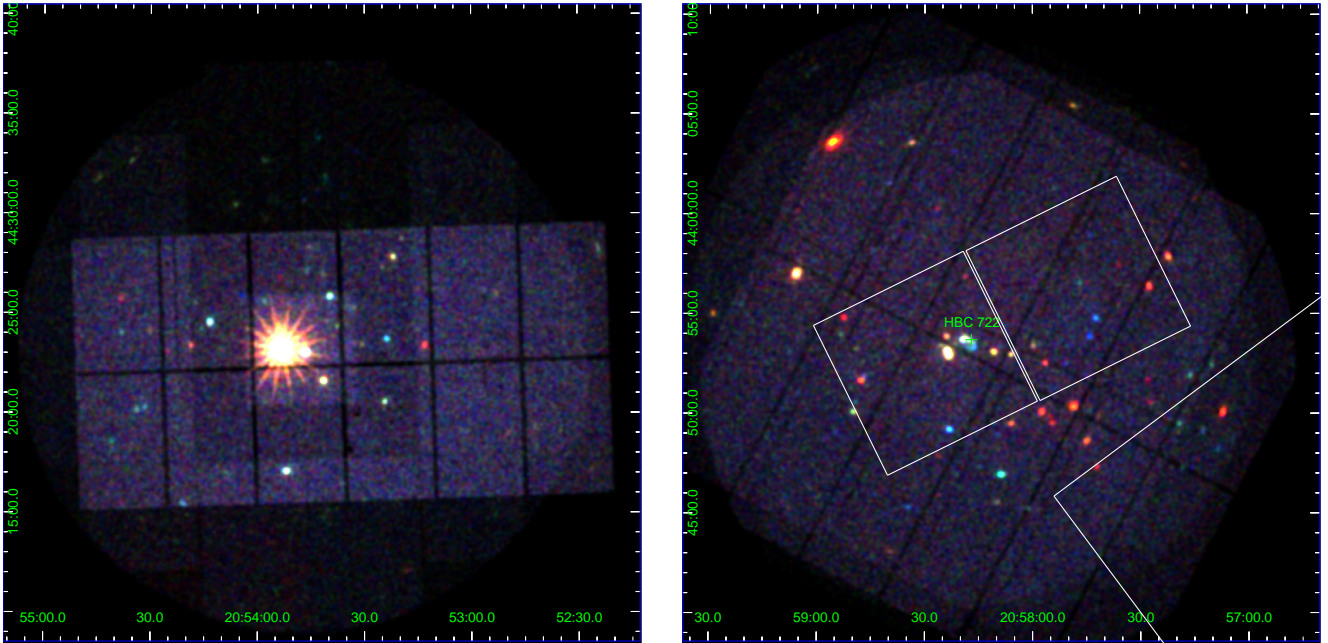


Fig. 6. X-ray images as in Fig. 4. Panel *a*, left: Archive XMM-Newton ObsId 0556050101, overlapping XMM ObsId 0679580201 of Fig. 5, panel *a*. The bright source is the same as in that Figure. The distribution of background emission seen here is caused by the small-window mode used here for the MOS cameras (not for the PN camera). *b*, right: Archive XMM-Newton ObsId 0656780701+0656781201. The slight pointing difference between the two ObsIDs causes the inter-chip gap pattern seen in the Figure. The image overlaps completely with the ACIS 14545 FOV, and partially with ACIS 13648 FOV in the lower right corner. The tight group of X-ray sources surrounding HBC 722 (Fig. 5, panel *c*) is unresolved here.

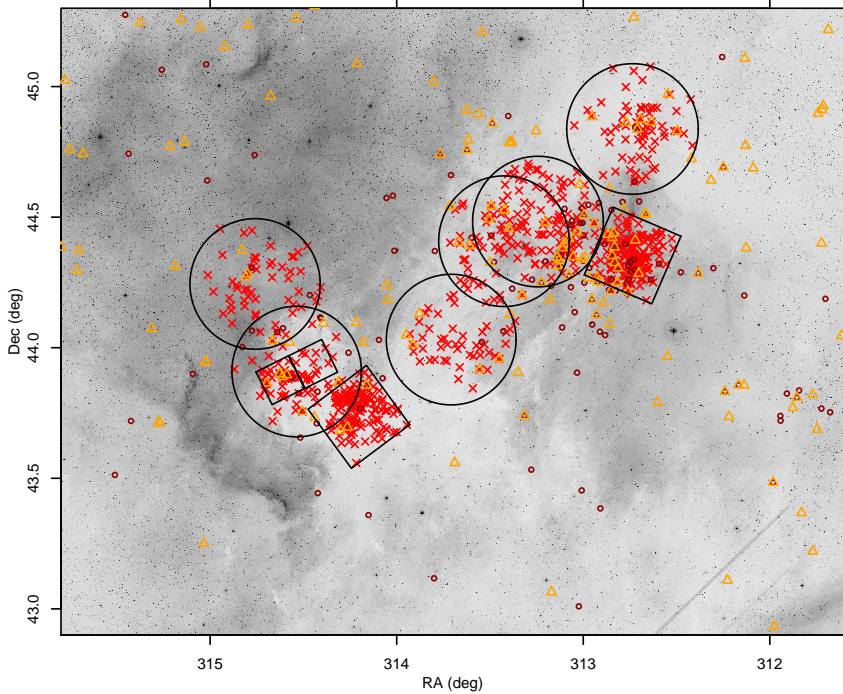


Fig. 7. Same field and background image as in Fig. 1, with small symbols now indicating: X-ray detected sources (red crosses), near-IR excess objects (orange triangles), and H α -excess objects (dark-red circles). Big circles/squares are X-ray FOVs as in Fig. 1.

4. Auxiliary data: optical and near-IR

We have complemented the X-ray data with data taken from the IPHAS DR2 (Barentsen et al. 2014), 2MASS PSC, and UKIDSS DR10plus GPS (Lawrence et al. 2007; table “reliableGpsPointSource”). All of these surveys cover the entire spatial region considered here. We extracted sources from a re-

gion of radius 1.5° centered on $(RA, Dec) = (313.7, 44.4)$. This yielded 1117062 IPHAS sources, however after applying the recommended screening (keeping only sources with flags $a10=1$ and $a10point=1$, i.e. point-like sources with high signal-to-noise ratio in all bands) their number reduces to 161635 sources.

The screened 2MASS PSC source list (flag *ph_qual* different from *E,F,U,X*, flag *cc_flg* different from *p,d,s*) contains 339774 sources. The UKIDSS source list instead contains 980770 sources. This is much larger than the number of 2MASS sources because of the greater depth of the UKIDSS survey; however, the UKIDSS data do not supersede the 2MASS data, since they saturate at the bright end ($J \leq 12$), where 2MASS still contains reliable data. We therefore use both sets of data, after an examination of their agreement on the sources common to both (see Appendix A). For these latter, the photometric errors are much lower in the UKIDSS than in the 2MASS magnitudes, so we adopt the UKIDSS ones whenever available. At large reddening, often found in this region, the UKIDSS photometry differs from 2MASS, so a slight recalibration was applied to agree with the 2MASS system (Appendix A).

We matched each of these source catalogs with our X-ray source list, up to a maximum offset of 4σ , where σ is the combined positional error from our X-ray detection code, from the 2MASS PSC error *err_maj*, or set fixed to $0.07''$ for the IPHAS and UKIDSS sources. There are 568 2MASS, 235 IPHAS, and 300 UKIDSS counterparts to our X-ray sources. The number of total counterparts using the combined NIR catalog is instead 548, lower than the 2MASS counterparts alone because of incomplete sets of magnitudes for several stars. 115 X-ray sources remained unidentified. The number of spurious matches between X-ray and optical/NIR sources is difficult to evaluate, since assumptions usually made to compute it (uniform spatial distributions of the two matched sets) are not fulfilled here. As we have seen above, X-ray sources are found near regions of strong obscuration, where the optical/NIR source density is much smaller than average, and changes on very small spatial scales. Moreover, the PSF (and source position error) of the XMM-Newton data is much larger than that of the Chandra ACIS data, so that even if the optical/NIR spatial density were uniform there is a higher chance of spurious matches for XMM-Newton X-ray sources than for the Chandra ACIS sources.

Finally, we positionally matched our X-ray source list with the YSOs from RGS11, obtaining 184 matches out of all 802 YSOs falling in our X-ray FOVs (by class: 33/189 for flat-spectrum YSOs, 23/195 for Class I, 123/370 for Class II, 4/23 for Class III, and 1/25 for unclassified YSOs). Of the H58 stars, 45 were falling in the X-ray FOVs and 31 were X-ray detected. It is worth remarking that the ACIS fields yielded larger detection percentages than the XMM-Newton fields, whose higher background resulted in a lower sensitivity. The median threshold X-ray luminosity for ACIS detection was found to be $\log L_X \sim 29.9$ erg/s, while the corresponding value for XMM-Newton is $\log L_X \sim 30.4$ erg/s, at the average absorption values inferred for these YSOs (see below). Considering all ACIS FOVs, 115 YSOs were detected out of 373 observed (by class: 25/94 flat-spectrum, 17/118 Class I, 72/132 Class II, and 1/8 Class III). The corresponding numbers for the XMM-Newton FOVs are 83 detections out of 551 observed YSOs (by class: 11/136 flat-spectrum, 10/115 Class I, 58/274 Class II, and 3/17 Class III).

Our X-ray source properties and identifications are reported in Tables 3 and 4.

5. Results

5.1. Distance

The deep IPHAS photometry enables us to perform a new determination of distance, relying upon the assumption that the obscuring dark cloud LDN935 lies immediately before the star-

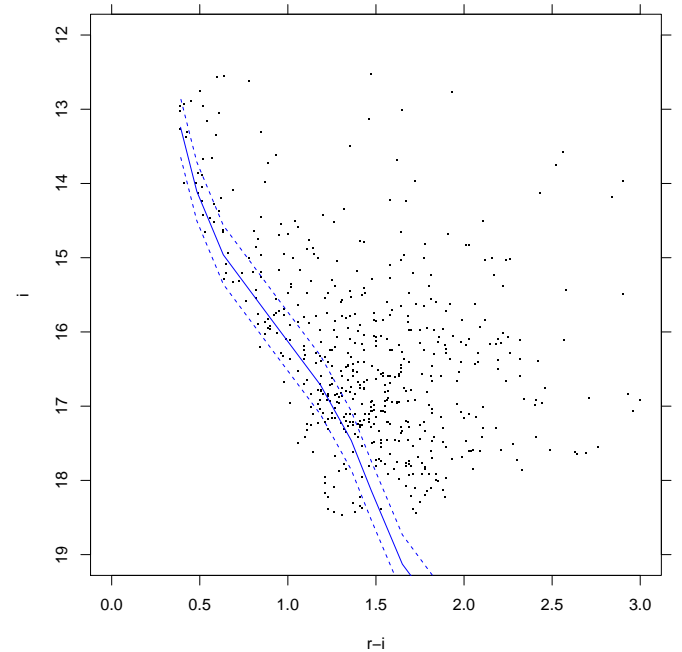


Fig. 8. An ($i, r-i$) CMD of stars towards two heavy-obscuration regions in LDN 935, with a 10-Gyr isochrone from BHAC at zero reddening and distance of 560 pc (blue solid curve). Blue dashed curves correspond to distances smaller and larger by 20%, respectively. Only datapoints with errors < 0.05 in both i and $r-i$ are shown.

forming region, as argued above. The method (already used by Prisinzano et al. 2005 to determine the distance of the young cluster NGC 6530) fits the lower envelope of datapoints in the color-magnitude diagram (CMD) to the shape of the main sequence of field stars, which are the lowest-luminosity field stars at each given color. It is therefore independent of any assumption on the cluster age or specific isochrone set. To apply the test we have selected two heavily obscured regions in LDN 935 (12-arcmin radius circles around $(RA, Dec) = (314.2, 43.6)$ and $(312.9, 44.9)$, respectively), whose CMD using IPHAS data is shown in Figure 8. Also shown is a 10-Gyr isochrone from Baraffe et al. (2015; henceforth BHAC) at zero reddening and distance of 560 pc, which provides a good fit to the lower envelope of datapoints (solid), at least for $r-i < 1$. The dashed curves ($\pm 20\%$ in distance) moreover suggest that the distance is unlikely to be larger than ~ 650 pc. Therefore, the new data are in good agreement with the accepted distance of the complex (560–600 pc, Laugalys et al. 2006, 2007). Since the BHAC tracks are not currently available from the IPHAS filter set we have recalibrated them for this filter set starting from those for the Johnson/Cousin filters, as explained in Appendix B.

5.2. $H\alpha$ -emission stars

The IPHAS survey also provides a $r - H\alpha$ index, useful to select $H\alpha$ -emission objects over wide sky areas. A $r - H\alpha$ vs. $r - i$ diagram for NAP is shown in Figure 9. Datapoints in the upper part of the diagram are emission-line stars. In particular, we show with a dashed line the color-dependent limit used by Kalari et al. (2015) to select CTTS stars. Almost all of the H58 PMS stars, and most of the RGS11 YSOs fall above that limit. We have therefore selected all stars significantly above that line (4σ above errors) as candidate CTTS. However, this choice yielded hundreds objects falling too low in the optical CMD ($i > 18$, $r-i \sim 1$,

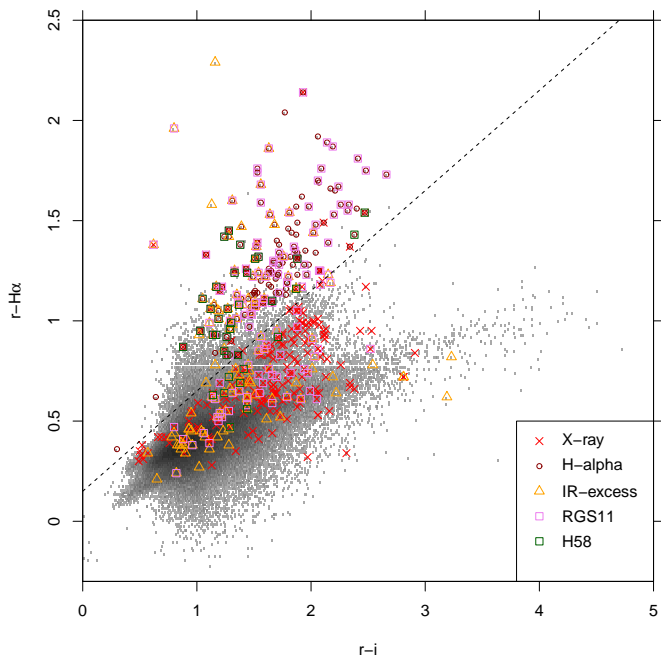


Fig. 9. IPHAS ($r - H\alpha$, $r - i$) diagram. The grayscale background is a 2-D histogram of all IPHAS objects in the sky region of Fig. 1, with bin sizes of 0.01 in both axes. The dashed line is the CTTS-star limit. Symbols as in Fig. 7, with the addition of YSOs from RGS11 (violet squares), and emission-line stars from H58 (dark-green squares). Hundreds of faint stars above the dashed line are not selected here as $H\alpha$ -emission stars because of their position in the CMD.

much below the ZAMS at the NAP distance), and mostly in the N-E quadrant of the surveyed region, i.e. spatially far from the known YSOs, that are thus unlikely to be young stars in the NAP. These are probably unrelated emission-line stars at much larger distances, and are therefore not included in our emission-star list, which comprises 153 stars (of which 30 detected in X-rays). The spatial distribution of accepted emission-line stars selected from the $r - H\alpha$ index is shown in Figure 7.

5.3. Optical and near-IR color-color diagrams

Different color-color diagrams can be used to estimate the amount of reddening and the possible presence of non-photospheric color excesses, likely originated in circumstellar dusty disks. The ($J - H$, $H - K$) diagram for the entire NAP region is shown in Figure 10. In agreement with Straižys, Corbally and Laugalyš (2008), we find that the Rieke and Lebofsky (1985) reddening-vector slope does not adequately describe the slope of datapoints in this diagram; therefore, we devote Appendix C to the careful determination of the reddening vector slopes for all independent color pairs in the NAP optical/NIR catalog. This redetermined reddening vector is shown in Fig. 10 and in all following color-color diagrams. To the right of the main locus of reddened normal photospheres, stars with K-band excess emission are found. We have set a fiducial limit to define such stars as the dashed line in the Figure. Stars significantly ($> 4\sigma$) to the right of this line are selected as NIR-excess objects, or candidate CTTSs (orange triangles in the Figure). The complete list of NIR-excess objects includes stars selected from other optical/NIR color-color diagrams (see below), hence the presence of several of them also to the left of the fiducial limit in Fig. 10. It should be remarked that this diagram, although widely used,

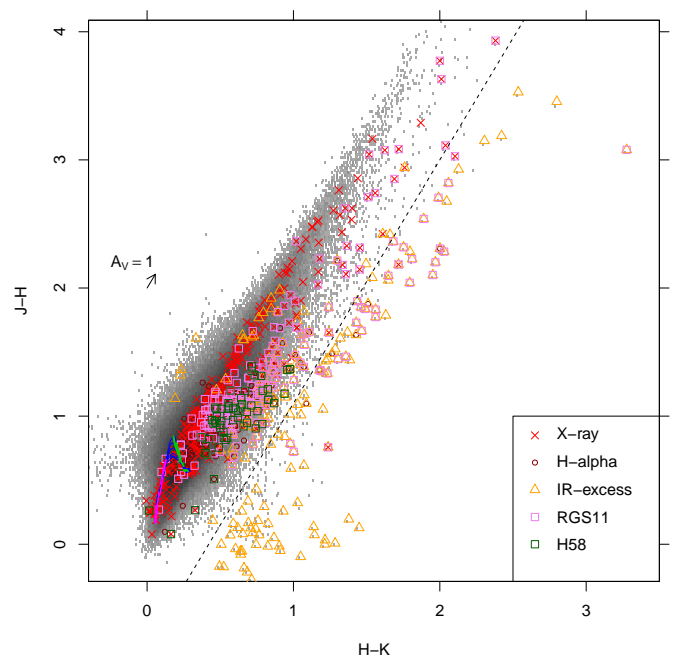


Fig. 10. Near-IR color-color diagram ($J - H$, $H - K$), using both 2MASS and UKIDSS data. Symbols as in Fig. 9. The arrow indicates the reddening vector corresponding to $A_V = 1$. The dashed line is the adopted limit to select NIR-excess objects from this diagram. The blue lines in the lower-left part are unreddened BHAC isochrones for ages of 1, 3, 10, 30, 100 Myr, and 10 Gyr, and masses between $0.08 - 1.4 M_\odot$. BHAC evolutionary tracks for masses of 0.1, 0.3, and $0.5 M_\odot$ are shown in green. In this and following color-color diagrams, only data with errors less than 0.1 mag on each color are shown.

is not a very efficient tool to select CTTSs: none of the CTTSs found by H58 (green squares) falls to the right of the limiting line in this diagram. Also very few of the RGS11 YSOs are found in the CTTS region of the diagram.

We have studied the properties of several mixed optical/NIR diagrams in the young cluster NGC 6530 (Damiani et al. 2006), which enable the selection of many more NIR-excess stars than the ($J - H$, $H - K$) diagram. Therefore, we use similar mixed optical/NIR diagrams also for the NAP stars. Figure 11 is a ($r - i$, $H - K$) diagram, where we again have drawn a fiducial line (with the slope of the reddening vector, see Appendix C), sufficiently distant from the bulk of stars, separating normal reddened photospheres (to its left) from NIR-excess stars, whose NIR colors are too red compared to the respective $r - i$ colors for any reddening value. The usefulness of this diagram is immediately seen by considering that here most of the H58 CTTSs and of the optically detected RGS11 YSOs are found to the right of our fiducial limit, together with other tens NIR-excess stars (orange triangles) not present in previously-known catalogs. The bulk of normal field stars are instead found along a reddened-photosphere locus, well reproduced by the available BHAC models (blue lines) and reddening vector. The magenta segment of the BHAC isochrones represents the locus of (unreddened) stars with $M > 1 M_\odot$; the upper envelope of datapoints is instead populated by the lowest-mass dwarf stars (isochrones are shown down to a minimum mass $M = 0.08 M_\odot$). Most of the X-ray sources in the NAP region do not show NIR excesses, neither from Fig. 11 nor from Fig. 10. Some of them follow well the zero-reddening isochrones, down to the substellar-mass limit, while in general Figs. 10 and 11 suggest that they are char-

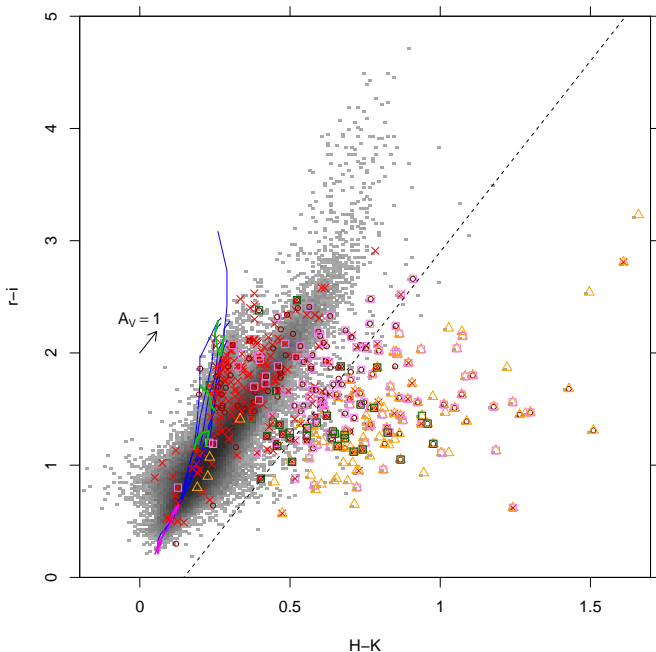


Fig. 11. Optical-IR color-color diagram ($r - i, H - K$). Symbols as in Figs. 9 and 10. The dashed line is the adopted limit for selection of NIR-excess objects from this particular diagram. The magenta thick line in the lower-left part indicates the location of unreddened stars in the mass range $1 - 1.4 M_{\odot}$. Much larger fractions of the H58 stars and of the RGS11 YSOs show a NIR excess using this diagram, compared to that of Fig. 10.

acterized by a wide range of reddening. The same conclusion was reached in Section 2 above from the visual inspection of the true-color X-ray images of Figs. 4–6.

Another useful diagram is $r - i$ vs. $J - H$ (Fig. 12) although in this case the number of NIR-excess stars selected is smaller than from Fig. 11. However, this color combination enables us to identify the lowest-mass stars more securely than previous diagrams, as it breaks the near-degeneracy between intrinsic stellar color and reddening, for masses below $\sim 0.3 M_{\odot}$ (green curves in Fig. 12 are BHAC evolutionary tracks for the lowest masses), as long as a star has photospheric colors. An even more detailed, non-degenerate determination of mass and reddening for individual stars is made possible by the rarely-used, but very interesting, $(r - i, i - H)$ diagram shown in Figure 13. The high-precision IPHAS and UKIDSS photometry undoubtedly are a major ingredient for this representation being so useful. Dwarf M stars, with $M \leq 0.5 M_{\odot}$, stand out clearly above the main locus of more massive stars, and are therefore effectively selected using this diagram. Most of them are unreddened ($2 < i - H < 3$), of which 34 detected in X-rays. This diagram indicates that the majority of X-ray sources having an optical counterpart have instead larger reddening, in the range $A_V \sim 2 - 4$. Only 3–4 of the H58 CTTs have inferred masses $M \leq 0.5 M_{\odot}$, while all others are more massive (if their $i - H$ color is photospheric, which may not be strictly true, see Fig. 11). The few X-ray sources to the left of the unreddened isochrones are not easily justified by any current model: their discrepant colors might arise from spurious matches between the IPHAS and 2MASS/UKIDSS catalogs, or from variability in the optical or NIR bands.

We have estimated the number of foreground X-ray sources as in Pillitteri et al. (2013), by integrating the field-star X-ray luminosity function (Favata and Micela 2003) up to the NAP dis-

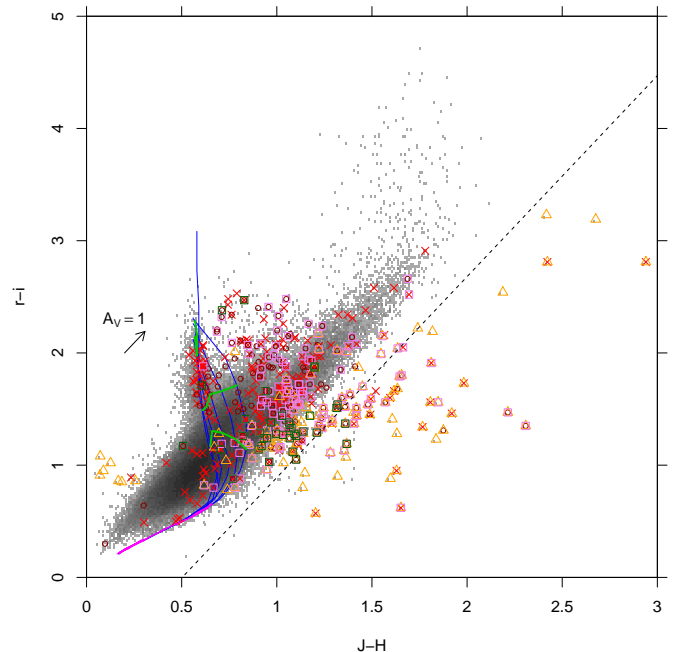


Fig. 12. Optical-IR color-color diagram ($r - i, J - H$). Symbols as in Figs. 9 and 10. The dashed line is the adopted limit for selection of NIR-excess objects from this particular diagram.

tance, and down to the limiting X-ray flux values appropriate to our X-ray observations (see Sect. 5.8 and Fig. 28). We estimate that about 67 foreground sources are detected cumulatively in all XMM pointings, and 18 in all ACIS pointings, for a total of ~ 85 foreground sources not related to the NAP. Being older than the NAP members, these are expected to be found among the softest detected X-ray sources (Güdel et al. 1997). The unreddened M stars found above, and many other X-ray sources found along the unreddened sequence in the diagram of Figure 13, are therefore the best candidates as foreground sources.

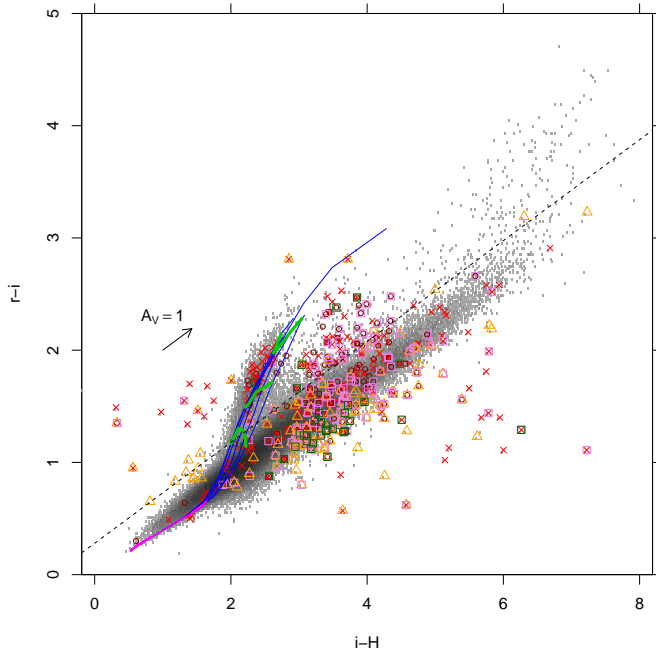
The number of NIR-excess stars is 208 (of which 29 detected in X-rays, and 38 common to the $H\alpha$ -excess list), and their spatial distribution can be seen in Fig. 7, with the maximum density found in the “Pelican” region. The 273 X-ray undetected NIR-excess and $H\alpha$ -excess stars are listed in Table 5.

5.4. Color-magnitude diagrams

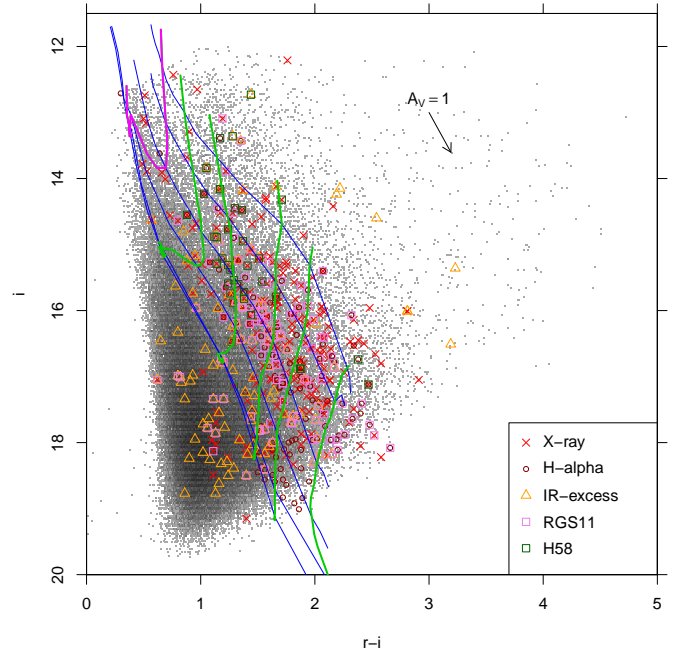
Figure 14 is an optical CMD for the whole NAP region. Comparison with Fig. 8 shows that thousands background stars are observed behind the cloud. Since no reddening correction was applied here, the apparent masses of e.g. the H58 stars, which as seen above are reddened by several magnitudes in the V band, are much lower than their actual values, in most cases larger than $0.5 M_{\odot}$ as discussed above. The few tens X-ray sources and NIR-excess stars below the 10-Gyr isochrone are not necessarily lying at larger distances: in fact, they share the same position in this CMD as many of the RGS11 YSOs. Below-ZAMS NIR-excess objects were already found in other young clusters like NGC 6530 (Damiani et al. 2006) or NGC 6611 (Guarcello et al. 2010), and may be attributed to photospheres obscured by edge-on disks, seen only in scattered light. Since datapoints shown in Figure 14 have all errors less than 0.1 mag, attributing their position in the CMD to errors seems instead unlikely.

Table 5. Optical/NIR photometry for X-ray undetected stars with IR/H α excess. Full table in electronic format only.

Seq no.	RA	Dec	<i>i</i>	<i>r - i</i>	<i>r - Hα</i>	<i>J</i>	<i>H</i>	<i>K</i>	IR excess	H α excess	RGS11 number
722	311.40294	45.08670				14.27	11.12	8.82	Y		
723	311.52945	44.78329				18.36	14.83	12.29	Y		
724	311.53239	44.77889	17.24	1.39	1.47	14.09	12.99	11.90	Y	Y	
725	311.55911	44.87168				16.97	14.68	12.89	Y		
726	311.56617	43.70630				14.34	13.48	12.59	Y		
727	311.57703	44.74357	18.29	1.23	0.45	14.51	12.68	11.83	Y		
728	311.61675	44.04525				15.47	13.82	12.45	Y		
729	311.67674	43.75285	17.36	1.98	1.28	15.02	14.15	13.66		Y	
730	311.68683	45.21762				14.36	11.17	8.75	Y		
731	311.70190	44.18731	16.78	2.17	1.66	13.53	12.46	11.95		Y	
732	311.71429	44.92656	17.22	1.64	0.76	14.46	13.38	12.55	Y		
733	311.71948	44.91088	15.76	1.25	0.55	13.46	12.46	11.66	Y		
734	311.72259	44.39995	18.03	1.46	0.75	16.34	14.26	12.97	Y		
735	311.72326	43.76692	17.89	2.21	1.65	15.23	14.54	14.07		Y	
736	311.74237	44.89695	16.83	1.11	0.36	14.54	13.45	12.43	Y		
737	311.74626	43.68682	16.51	3.19	0.62	12.88	10.21	8.16	Y		
738	311.76965	43.22022				16.45	15.01	13.63	Y		
739	311.77003	43.81984	17.55	1.16	2.29	15.18	14.26	13.56	Y		
740	311.82935	43.36731				17.05	15.70	14.50	Y		
741	311.84319	43.83651	15.38	1.16	0.84	13.70	12.73	12.41		Y	

**Fig. 13.** Optical-IR color-color diagram ($r - i, i - H$). Symbols as in Figs. 9 and 10. Stars less massive than $0.5M_{\odot}$ (M-type) fall above the dashed line.

Considering X-ray sources, there is no clear sequence or cluster locus in the CMD, probably because of the large scatter in extinction from star to star. Estimating individual extinction values is subject to large uncertainties, as we will discuss in the following. Two-thirds of X-ray sources lack an IPHAS counterpart, probably because they are too highly reddened. Figure 15 shows therefore the NIR CMD ($J, J - H$). The frequency and intensity of non-photospheric dust emission in these NIR bands is probably lower than in the K band, from the comparison of Figs. 11 and 12. The distribution of datapoints, elongated parallel to the

**Fig. 14.** Optical color-magnitude diagram ($i, r - i$). Symbols as in Figs. 9 and 10. Unreddened BHAC evolutionary tracks are here shown for masses of $0.1, 0.2, 0.3, 0.5, 0.7 M_{\odot}$ (green), and $1 M_{\odot}$ (magenta). In this and following color-magnitude diagrams, only data with errors less than 0.1 mag on each axis are shown.

reddening vector, suggests that indeed reddening, rather than H -band excess, is responsible for most of the spread towards red colors, by up to $A_V \sim 35$ for the most reddened X-ray sources and YSOs with a NIR counterpart. A considerable number of X-ray sources has inferred $A_V \geq 10$, if indeed their $J - H$ color is photospheric.

Finally, Figure 16 shows the ($H, H - K$) diagram. The spread towards red colors is here probably due to a combination of red-

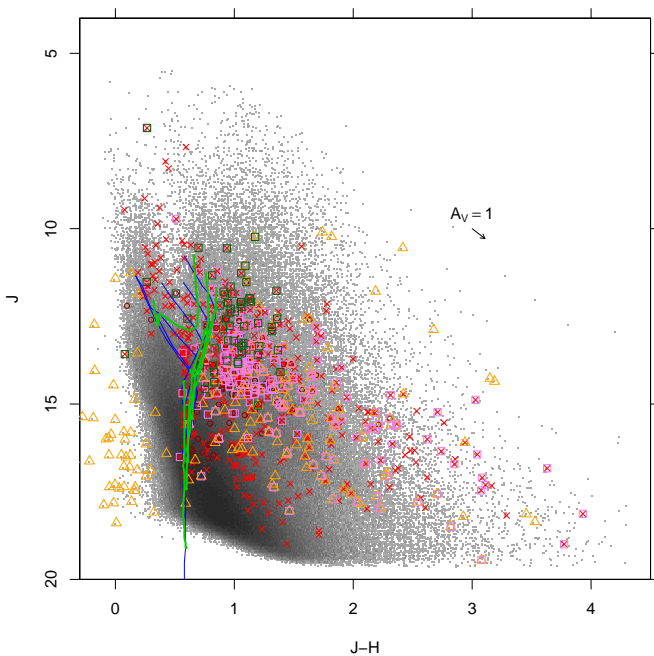


Fig. 15. NIR color-magnitude diagram ($J, J - H$). Symbols as in Figs. 9 and 10.

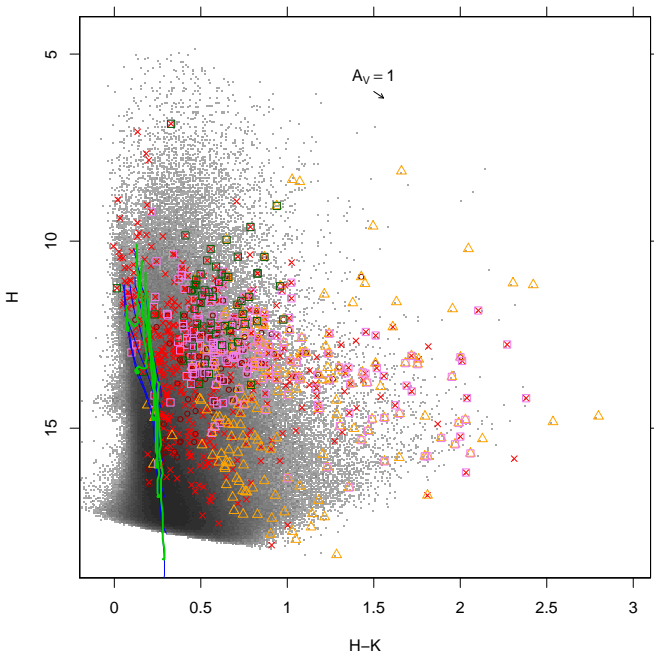


Fig. 16. NIR color-magnitude diagram ($H, H - K$). Symbols as in Figs. 9 and 10.

dening and K -band excess emission. The diagram shows that several tens new NIR-excess sources (not identified with a YSO from RGS11) are much fainter objects (with $H > 15$) than these latter. The majority of X-ray sources has $H - K \leq 0.5$, no NIR excesses, and H magnitudes fainter than the H58 stars.

In the presence of strong differential reddening, as we discuss below, incompleteness affects the optical CMD much more than the NIR CMD: from Figure 14 we see that while for low reddening the IPHAS photometry reaches down to the sub-stellar limit at the NAP distance and ages ≤ 3 Myr, the mass complete-

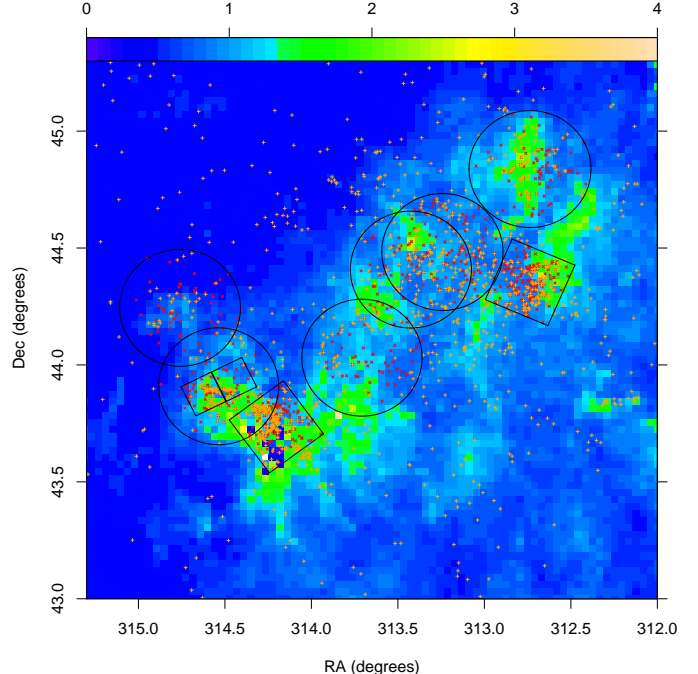


Fig. 17. Spatial map of average $J - H$ (scale at figure top) as a measure of extinction. Indicated are the X-ray FOVs as in Fig. 1. The datapoints indicate X-ray sources (red) and RGS11 YSOs (orange).

ness limit rises rapidly for increasing extinction (e.g. $\sim 1 M_{\odot}$ for $A_V \sim 5$). Our combined NIR catalog reaches at least 3-4 magnitudes deeper than the substellar limit at the same age, and is moreover much less sensitive to extinction (Figures 15 and 16), which accounts for the much larger number of NIR counterparts to X-ray sources (548) compared to optical counterparts (235).

5.5. Extinction and reddening

The wide range of extinction indicated by the above diagrams may have a local component, arising in the individual circumstellar environments, but also shows definite large-scale patterns, as shown by Cambrésy et al. (2002) using 2MASS data. Here we take advantage of the more precise UKIDSS NIR data to build a more detailed extinction map of the NAP, based on the average $J - H$ color, as shown in Figure 17. Optical extinction is approximately 10 times the average $J - H$ (minus 0.5), so that the most obscured regions correspond to $A_V \sim 35$, and the “green” regions in the map correspond to $A_V \sim 15$.

The $J - H$ color may be considered as the best indicator of reddening for our NAP candidate PMS members, either X-ray detected or from $H\alpha$ - or NIR excess: it is available for most candidate members (548/721 X-ray sources, 817/994 X-ray/ $H\alpha$ /NIR-excess sources), is less affected by non-photospheric emission than the K band magnitudes, and normal stars fall within a small $J - H$ color range (Fig. 12), especially for $M < 1 M_{\odot}$. The mass dependence of $J - H$ color may moreover be partially compensated by using a “corrected” color, of the form:

$$(J - H)_c \equiv (J - H) + 0.526 (H - K) \quad (1)$$

for stars not classified as NIR-excess sources; the intrinsic unreddened value of $(J - H)_c$ is ~ 0.75 for all masses in the range $0.08 - 1 M_{\odot}$, and ages ≥ 20 Myr, with slight deviations for younger low-mass stars (Figure 18). Individual visual extinction

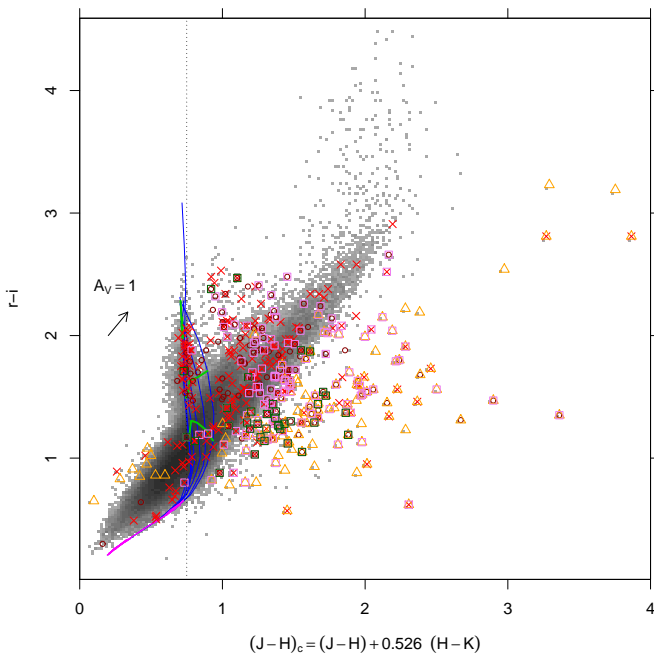


Fig. 18. Mixed color-color diagram of $r - i$ vs. corrected color $(J - H)_c$ (see text). Symbols as in Figs. 9 and 10. The vertical dotted line indicates the value $(J - H)_c = 0.75$.

A_V , for stars with $(J - H)_c > 0.75$, can be estimated therefore as

$$A_V \sim ((J - H)_c - 0.75) \times (A_V / (E(J - H) + 0.526 E(H - K))) \quad (2)$$

where the last factor above is the (constant) reddening vector slope, equal to 7.318 (using the Rieke and Lebofsky 1985 reddening law). For stars more massive than $1M_\odot$ this underestimates A_V , since their intrinsic $(J - H)_c$ color is lower (bluer) than 0.75. Extinction A_V for stars with a NIR excess is instead estimated from the $J - H$ color alone (this is again an underestimate for $M > 1M_\odot$).

By using these individual A_V values (converted to the IPHAS bands A_i and $E(r - i)$ as explained in Appendix C) we have built the dereddened optical CMD, shown in Figure 19. The clustering of X-ray sources at $(r - i)_0 \sim 1$ is probably an artifact resulting from our underestimated reddening for stars above $1M_\odot$. The bulk of X-ray sources, if lying at the NAP distance, are found in a 2-mag wide strip corresponding to the PMS band, between ages 1-10 Myr, also populated by the majority of H58 stars (on average brighter than the rest of the X-ray-source counterparts) and optically-visible YSOs. Tens of NIR-excess stars are found apparently below the main sequence at the Nebula distance, as remarked above. The unreddened X-ray-detected M stars selected from Fig. 13 have especially reliable positions in this diagram, since they required no dereddening: they do not form a proper sequence in this CMD, but are mixed to other low-mass NAP X-ray sources. They might still be foreground, active M dwarfs, 3 to 10 times closer than the NAP; this diagram does not permit to confirm (nor exclude) their NAP membership.

5.6. Spatial distributions

As found by e.g. Cambrésy et al. (2002) and RGS11, the spatial distribution of young stars in the NAP is highly non-uniform. This non-uniformity also holds for the X-ray source distribution (Figs. 4 to 6). Therefore, we examine here in more detail the

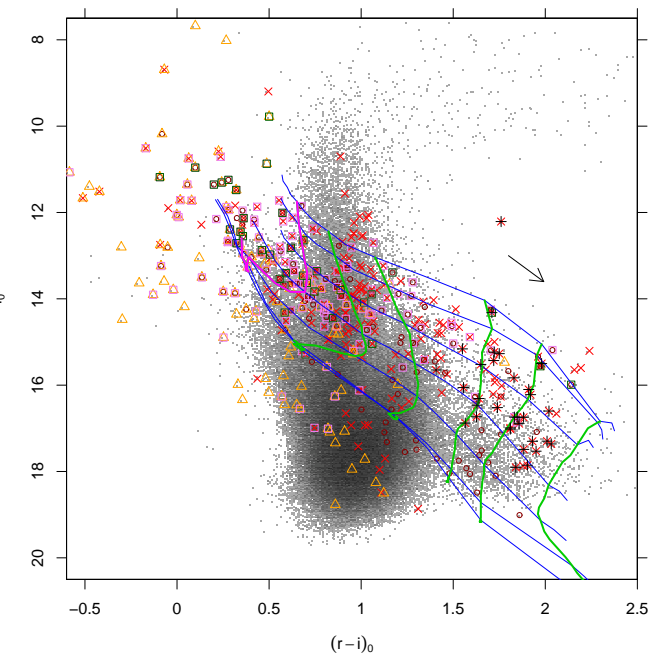


Fig. 19. De-reddened optical CMD. Symbols, isochrones and evolutionary tracks as in Fig. 14. The black plus signs are the unreddened M stars from Fig. 13 (with $2 < (i - H) < 3$).

properties of each spatial sub-region. The individual panels of Figures 20 and 21 permit a comparison between the spatial distributions of all sets of data considered here. The background greyscale image represents the local density of all optical/NIR objects (in white the lowest densities), which is inversely correlated with the mean reddening (Cambrésy et al. 2002) shown in Fig. 17, but is a somewhat more versatile indicator (e.g. for sources with too noisy or missing J magnitudes). As in Figs. 1 and 7, big solid circles/squares are X-ray FOVs, while RGS11 YSOs are indicated with black plus signs. X-ray sources are here instead color-coded, according to their observed $J - H$ color, with the color scale shown in the upper left panel of Fig. 20. X-ray sources without a NIR counterpart, or with missing $J - H$, are drawn with a red color, assuming that high extinction is the reason for the missing measurement.

The “Pelican hat”, as in RGS11, is the northernmost field in our survey (Fig. 20, top left), covered by XMM-Newton ObsId 0679580101. The region hosts a local concentration of YSOs (see RGS11), nearly coincident with a region of enhanced obscuration, elongated along N-S direction, through the center of the XMM-Newton FOV. Curiously, most X-ray detected sources in this field lie to the right of center (inside the dashed rectangle in the Figure). Their $J - H$ colors suggest they are an inhomogeneous group, either with very different extinction values, and/or a wide range of masses. Very few of these in-rectangle X-ray sources also possess a NIR excess. At the same time, they are not spread uniformly across the X-ray FOV, as if they were an unrelated field-star population¹, but closer to the West side of the obscured region. Therefore, these X-ray sources appear to correspond to a sub-population of the NAP which is missed by YSO/CTTS searches, even using Spitzer or mixed optical/IR criteria; they also lack strong H α emission, as are not coincident

¹ The XMM-Newton EPIC camera sensitivity dependence on off-axis distance is flat enough that such a central concentration of detections cannot be an instrumental effect. See also Sect. 5.8.

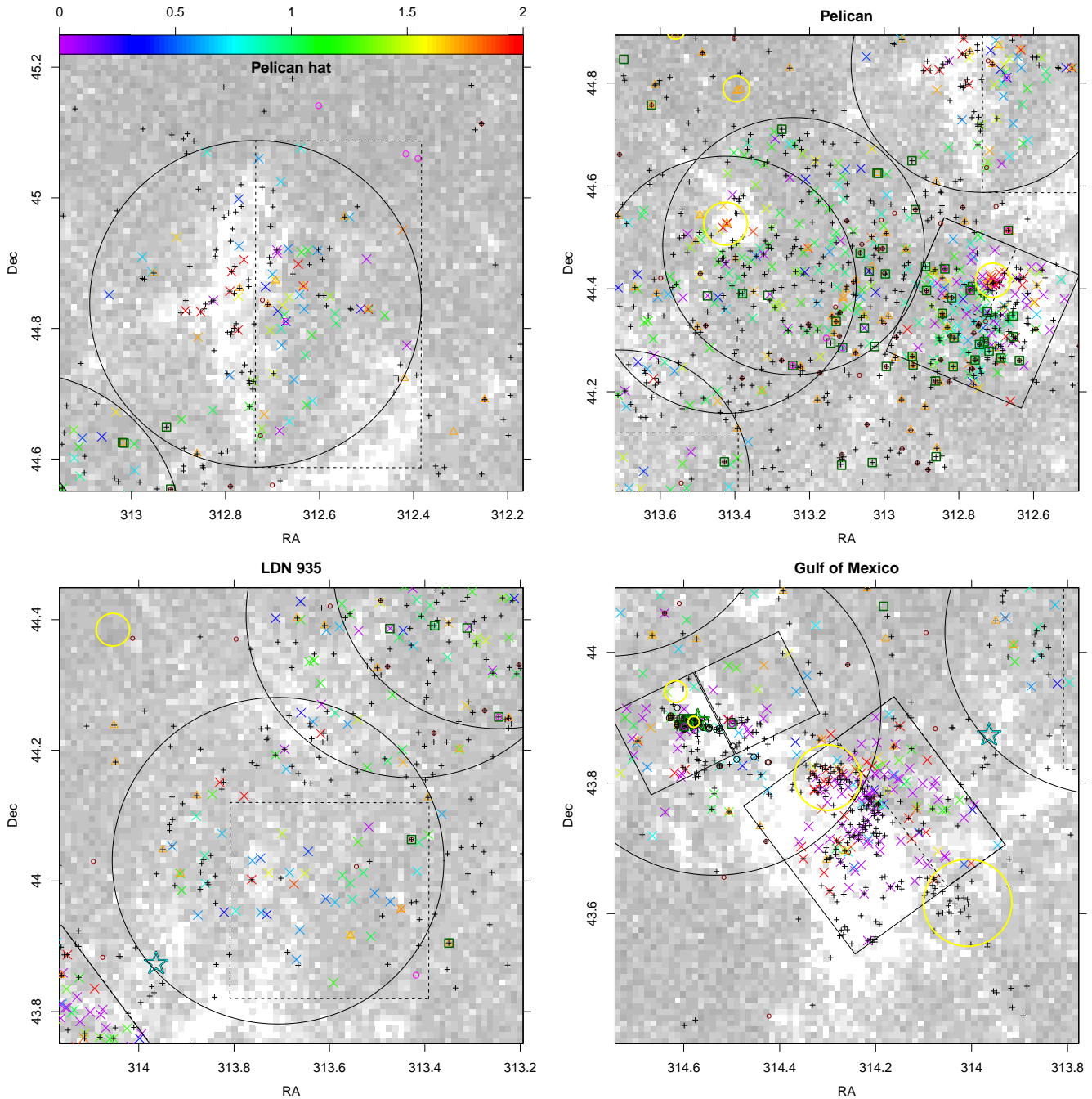


Fig. 20. Comparison between spatial distributions of X-ray sources, YSOs and other young stars in each X-ray FOV. The background grayscale image is a 2-D histogram of the combined optical-NIR object density, showing clearly high-obscuration regions. Solid black circles/squares are XMM/ACIS FOVs, respectively. Symbols as in Figs. 9 and 10, except that here X-ray sources (crosses) are color-coded according to their $J - H$ color (with the color scale show in the top left panel). X-ray sources without a NIR counterpart are shown in red. Black plus signs indicate positions of all RGS11 YSOs, regardless of their identification with X-ray or other catalogued objects. Small empty circles are young stars from Armond et al. (2011; black) and Welin (1973; violet). Yellow circles are 2MASS star clusters from Cambrésy et al. (2002). The black dashed rectangular regions are defined here as places with a local overdensity of X-ray sources, not matched by an overdensity of YSOs. The three bigger star symbols indicate respectively the O5 star 2MASS J20555125+4352246 (cyan), and FUOrs HBC722 (green) and V1057 Cyg (orange).

with IPHAS-selected CTTSs. The properties of this group of X-ray sources are perhaps best interpreted as a group of relatively older WTTS members of the NAP population, and their spatial placement relative to the younger YSOs (and the currently cloud overdensity seen from the star-count map) as an indication of sequential star-formation episodes, proceeding from West to East in this particular region of the NAP.

The upper-right panel of Fig. 20 (“Pelican” field proper) was covered by one new (0679580201) and one archival (0556050101) XMM-Newton observations, and by Chandra ACIS-I ObsIds 13647 and 15592; it hosts most of the H58 stars, and a large number of RGS11 YSOs (though not the highest density). Most of the X-ray sources in the XMM-Newton FOVs (those in the ACIS-I FOV will be discussed below) have intermediate $J - H \sim 1 - 1.5$, except for 4-5 higher-reddening X-ray

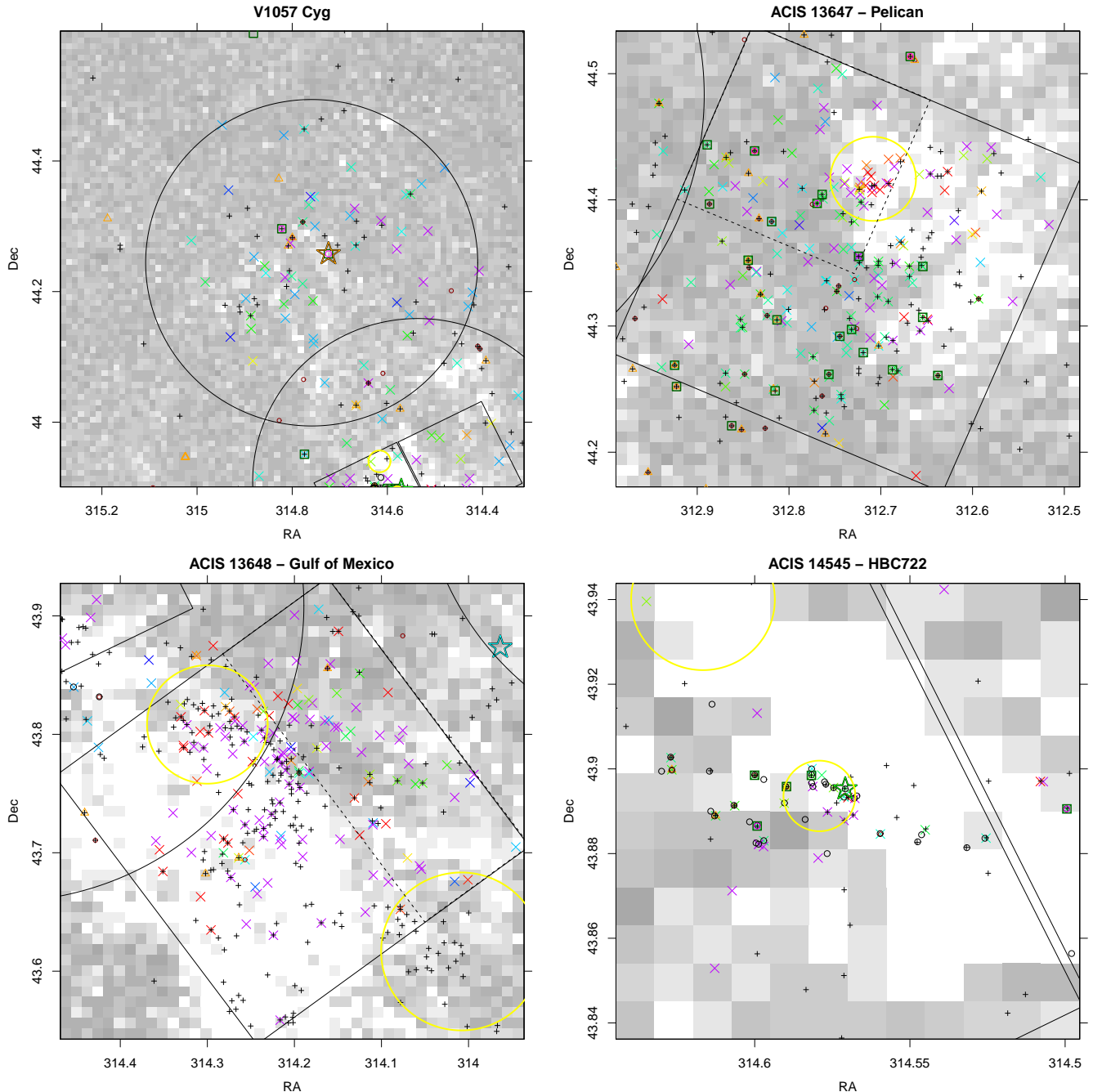


Fig. 21. Continuation of Fig. 20. In the lower-right panel the zooming factor is much larger than in the other panels, to help visually resolve the dense cluster in the center. The 2-D bin size of the background image (and the density-grayscale conversion) is the same in all panels here and in Fig. 20.

sources falling in a more obscured region, and also coincident with Cluster #6 from Cambrésy et al. (2002; yellow circles).

Next, the lower-left panel of Fig. 20 (LDN 935) shows our XMM-Newton field closest to the most obscured part of the NAP, and also to its illuminating O5 star, which lies just outside of our (ObsId 0679580301) FOV. In proceeding from the Pelican region towards the O5 star, there is an obvious gradual decrease in the YSO spatial density. Also the S-E part of the XMM-Newton FOV, closest to the O star, is almost devoid of X-ray sources. The central and S-W part of this FOV (again marked with a dashed rectangle) contains very few YSOs, but still a few tens X-ray sources, again with a mixture of $J - H$ values.

The “Gulf of Mexico” region (lower-right panel of Fig. 20) hosts a crowded YSO population, and also dense groups of X-ray sources, which the spatial resolution of the XMM-Newton EPIC images was insufficient to resolve. The region, also containing four of Cambrésy’s clusters, shows very definite spatial relationships between the obscuration pattern, the YSO and X-ray populations. Its properties are best examined by looking at the individual Chandra FOVs, as we do below. To conclude with our XMM-Newton observed fields, Fig. 21, upper-left panel, shows the archival ObsId 0302640201, centered on the FU Ori star V1057 Cyg (not detected in X-rays), and containing inconspicuous, low-density populations of both YSOs and X-ray sources. North of it, corresponding to “continental North America”, Fig-

ure 17 shows that both the YSO density and the average reddening are very low: although some hot, ionized gas must be there to produce the emission nebula, the total dust column density must be low not to redden background giants (main contributor to the star-count map); a low amount of warm dust there is also evident from Fig. 2, so that we do not expect active star formation in this region.

Our ACIS-I “Pelican” FOV (upper-right panel of Fig. 21) comprises the highest density of H58 PMS stars, and also probes with high spatial resolution the bright-rimmed cloud giving the nebula its shape (see Fig. 2). This cloud is so dense to obscure most background stars behind its illuminated rim (see also Fig. 17). This latter coincides with a cluster from Cambrésy et al. (2002), which is also detected as a small cluster of highly reddened X-ray sources. In the N-E part of the ACIS FOV (dashed square), the X-ray source density is larger than the YSO density, the latter being much more numerous in the southern part of the same FOV.

Both the YSO spatial density and local obscuration reach their maximum inside our “Gulf of Mexico” ACIS-I FOV (lower-left panel of Fig. 21), with YSO falling along arch-like patterns near the border of the obscured region. Many tens X-ray sources are also following the same pattern, indicating that they are also young stars belonging to the NAP population. Some of them have large reddening, especially those coincident with Cambrésy’s Cluster #2 (northernmost yellow circle). The obscuring material here, unlike that in the Pelican nebula, does not coincide with the (southern) bright rim, as it should be evident from comparing Figs. 2 and 17. To the N-W of the most obscured region and the YSO cluster, the YSO density drops abruptly but there are still several tens of X-ray sources (dashed rectangle), which appear to be too little reddened to belong to the background, and too numerous to belong to the foreground of the NAP: they again are good candidates as WTTs members of the NAP. It is worth remarking that their spatial density increases towards the obscured region, while it decreases slightly towards the N-W border of the FOV, in the direction of the O5 star, only 5' away. As above, there is not detectable increase of X-ray source density in the neighborhood of the most massive star. It might be argued that the in-rectangle X-ray sources are too lightly reddened to be NAP members, in a region dominated by strong obscuration, and that they are unlikely to lie all on the near edge of the obscuring dust. The reason for their apparent low reddening might then be their higher mass ($M > 1M_{\odot}$), causing reddening from $J - H$ to be increasingly underestimated the higher the actual mass is.

Last, in the lower-right panel of Fig. 21 we show a zoom of the central part of archive ACIS-S ObsId 14545, centered on the recently-erupted FU Ori object HBC722, surrounded by a dense group of X-ray sources, known YSOs and PMS stars (H58, Armond et al. 2011; also coincident with Cambrésy’s Cluster #3b): they lie all near the border of a strong-obscuration region.

5.7. X-ray spectra, lightcurves and luminosities

Whenever X-ray sources are detected with a sufficient number of X-ray counts, their X-ray spectra and lightcurves may help to understand their nature. Here we make use of hardness ratios and do not perform a detailed best fit of the spectra of the brightest sources, deferring this to a future paper. Hardness ratios are here defined as $HR1 = (M - S)/(M + S)$, and $HR2 = (H - M)/(H + M)$, where S , M , and H are the source X-ray counts in the soft (0.3–1.2 keV), medium (1.2–2.4 keV), and hard (2.4–8.0 keV) bands, respectively. $HR1$ is most affected by the line-of-sight absorp-

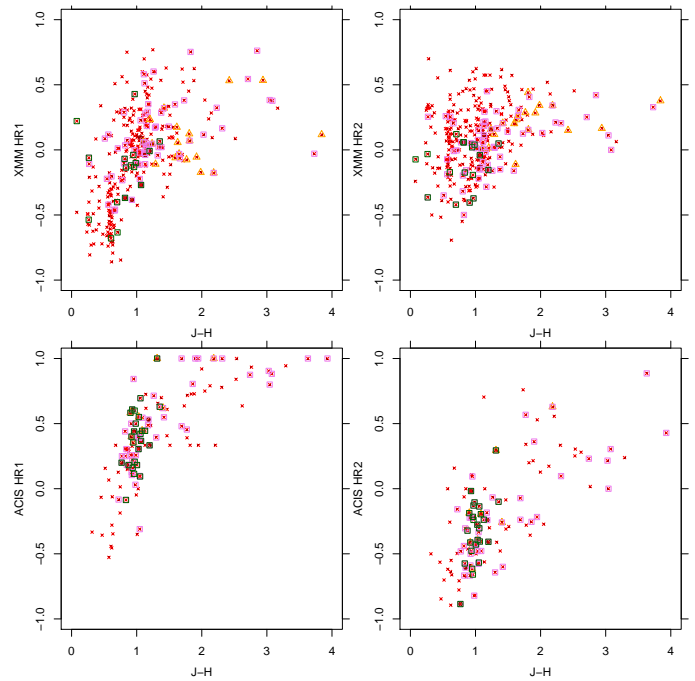


Fig. 22. Hardness ratios (left panels: $HR1$; right panels: $HR2$) vs. $J - H$, for all ACIS (bottom panels) and XMM-Newton (top panels) X-ray sources. Symbols as in Fig. 9.

tion of soft X-ray photons, while $HR2$ is affected by absorption only at very high column densities, and more often is a measure of intrinsic spectrum hardness (and high plasma temperatures for thermal sources). Figure 22 compares these hardness ratios with the $J - H$ color, separately for XMM-Newton sources (with more than 50 X-ray counts) and ACIS sources (with more than 20 counts). Since the instrumental effective area has a different energy dependence for XMM-Newton and Chandra ACIS, the respective $HR1, 2$ must not be mixed together. We have argued above that $J - H$ is dominated by reddening: this is further supported by the fairly good correlation between $HR1$ and this color (left two panels in Fig. 22); the X-ray sources associated with a H58 star or with a RGS11 YSO follow the same relation as the other sources. A much weaker correlation is seen between ACIS $HR2$ and $J - H$, as expected if $HR2$ is only weakly related to absorption. No relation is seen between XMM-Newton $HR2$ and $J - H$. Also when considering $HR2$, the X-rays sources with a H58 star/YSO association are homogeneous with the others. Nearly all of H58 stars have (XMM-Newton or ACIS) $HR2 \leq 0$, indicative of not-too-hot X-ray emitting plasma. Over the same $J - H$ range of the H58 stars, however, the upper-right panel of Fig. 22 shows that about one-half of the RGS11 YSOs have $HR2 > 0$, and thus even hotter plasmas, in agreement with previous results on very young Class I/II protostars in Orion (e.g. Prisinzano et al. 2008). The group of unreddened X-ray sources at $J - H \sim 0.6$, already mentioned with reference to Figs. 12 and 13, is also recognizable in the two upper panels of Fig. 22, their $HR1, 2$ also being rather homogeneous. Their low $HR1$ values confirm their low line-of-sight absorption, but not lower than several of the H58 CTTS; their $HR2$ values average to ~ 0 , like the bulk of YSOs, which suggests that these X-ray sources have intrinsic spectra no different from the bona-fide population of the NAP, despite that their low reddening/absorption is compatible with being active foreground stars.

We have also examined the X-ray lightcurves of sources detected with enough counts. Some examples are shown in Fig-

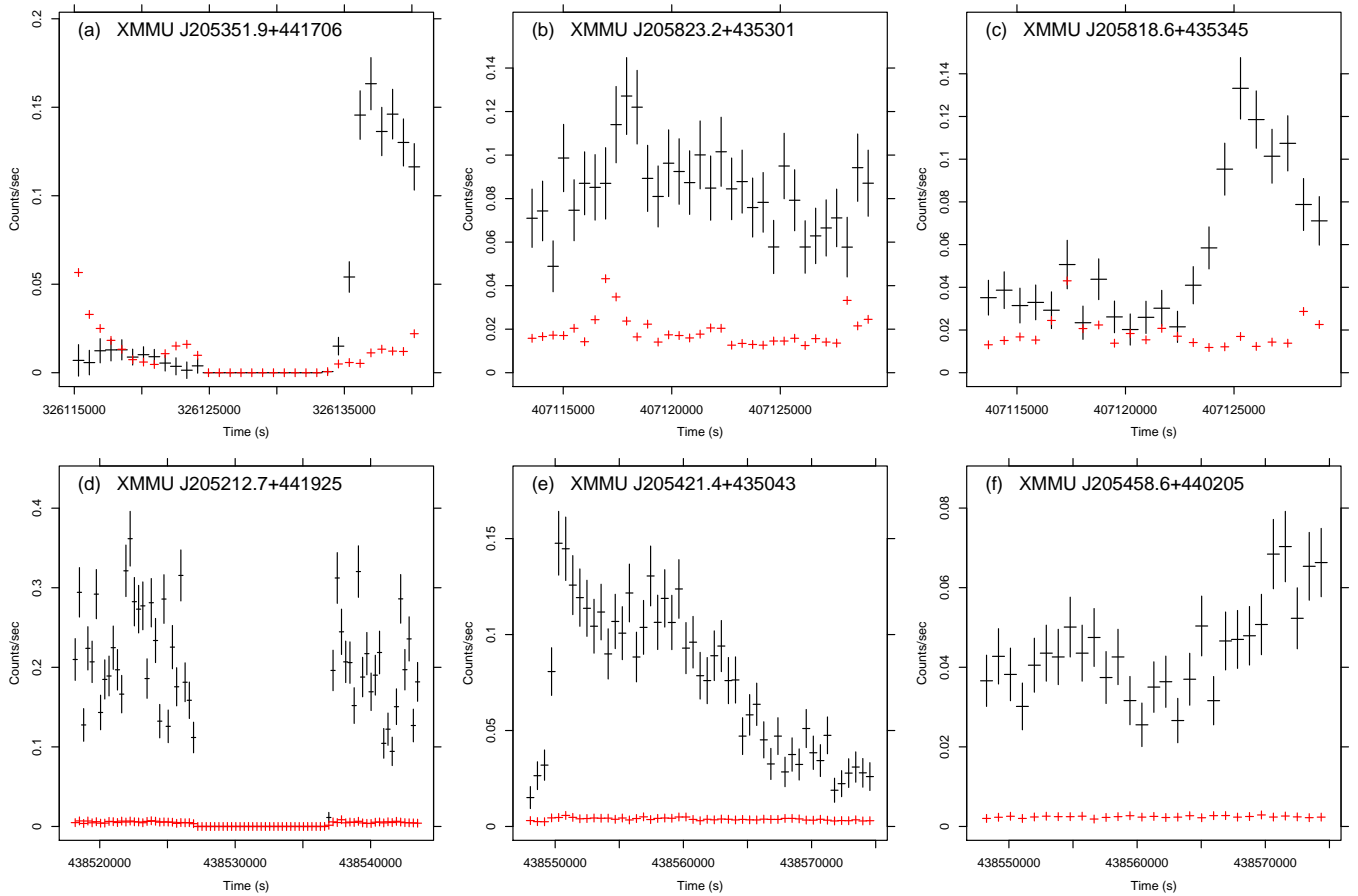


Fig. 23. Examples of (background-subtracted) X-ray light curves of XMM-Newton X-ray sources. The observations of sources in panels (a) and (d) have interruptions in the middle, hence their zero count rates there. The background count rate, scaled to the source area, is shown with red symbols.

ure 23, which illustrates the type of variability found. When the count rate is large enough, most sources are found to be variable; in many or most cases, lightcurve shapes are complex, while “simple” flares with impulsive rise and exponential decay are more rare. This is reminiscent of the X-ray lightcurves of YSOs in the ρ Oph star-forming region, from the XMM-Newton DROXO survey (Pillitteri et al. 2010). Panel e shows a probable (double-peaked) flare event, with a long decay time of ~ 10 ksec, as found e.g. in the COUP Orion lightcurves (Favata et al. 2005). Some of the XMM-Newton observations have long interruptions in the middle (like in panels a and d). Large-amplitude variability on timescales of one day may also be seen from the comparison of the co-pointed ACIS-I images ObsId 13647 and 15592, already shown in Fig. 4.

Since X-ray emission decays with stellar age, one possible way of discriminating very young stars in the NAP from foreground/background active non-members is through the use of X-ray-to-optical luminosity ratios, which decrease with mass-dependent timescales (e.g. Preibisch and Feigelson 2005). Ratios of X-ray to bolometric (L_X/L_{bol}) or X-ray to visual (L_X/L_V) luminosities are commonly used. In our case, the difficulty in obtaining accurate extinction values for individual X-ray sources makes these ratios unsuitable, and has prompted us to search a reddening-free equivalent ratio. It is well known that while the dust absorption decreases from optical to IR wavelengths, the X-ray absorption decreases from the soft to the hard X-ray band, with photons of energy $E = 2$ keV being absorbed like NIR photons with $\lambda = 2\mu$, for a typical interstellar gas/dust ratio. There-

fore, we searched for an X-ray energy range where absorption is equivalent to that in the J NIR band, which as discussed above is convenient to study our NAP stars. We made several experiments using the PIMMS software², for different energy bands: 0.8–1.2 keV, 1.0–1.8 keV, and 1.2–2.4 keV, sufficiently wide for being well characterized at the spectral resolution of Chandra/ACIS detector. Three single-temperature APEC thermal models were considered, in the temperature range of Class I/II/III YSOs. Hydrogen column density (N_H) values were converted to optical extinction using the relation $N_H = 2.22 \cdot 10^{21} A_V$ (Gorenstein 1975), while the correspondence between A_V and NIR extinction is explained in Appendix C. The results of the experiment is shown in Figure 24, where the ordinate shows the relative flux attenuation. We see that the X-ray band between 1.0–1.8 keV is absorbed by an amount similar to the J band, within a factor of $\sim 50\%$ up to $A_V \sim 10 - 12$. Absorption in the harder 1.2–2.4 keV band is also very close to that in the H band; however, X-ray counts are often less in this higher-energy band than in the 1.0–1.8 keV band, and the NIR H band is more easily affected by non-photospheric contributions than the J band, so that the pair [1.0–1.8 keV]/ J seems preferable to obtain an absorption-independent flux ratio.

A plot of X-ray count-rate in the 1.0–1.8 keV band vs. J is shown in Figure 25, for ACIS-I sources with $J - H < 2$, corresponding roughly to $A_V = 12$. In this diagram, absorption causes datapoints to move parallel to the dashed line, and might par-

² Portable, Interactive Multi-Mission Simulator, available at <http://heasarc.gsfc.nasa.gov/docs/software/tools/pimms.html>

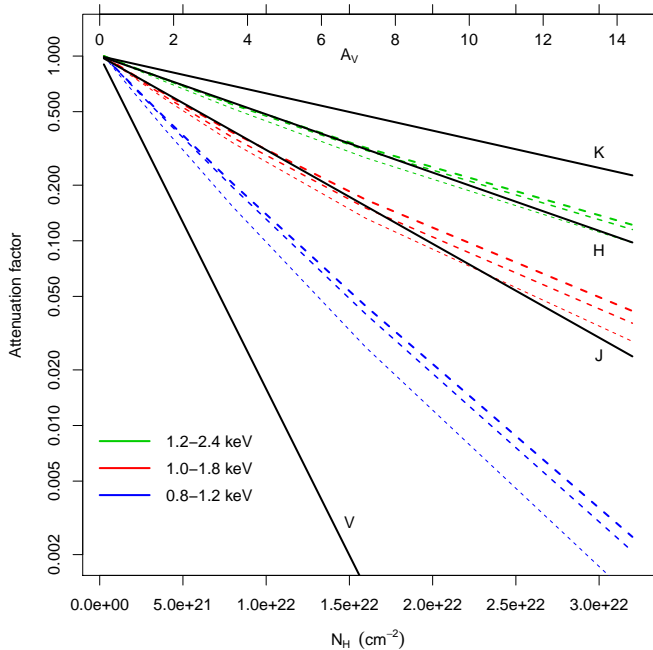


Fig. 24. Computed attenuation factors for X-ray and NIR emission and variable line-of-sight absorption, as parameterized by the hydrogen column density N_H (bottom axis) and its equivalent extinction A_V (top axis). X-ray attenuation of the observed ACIS-I flux is computed for three single-temperature emitting plasmas (short-dashed: 1 keV; mid-dashed: 1.5 keV; long-dashed: 2 keV), and three energy ranges, as labeled. Optical and NIR attenuation is shown (using the A_λ/A_V conversions from Rieke and Lebosky 1985) with the black solid lines.

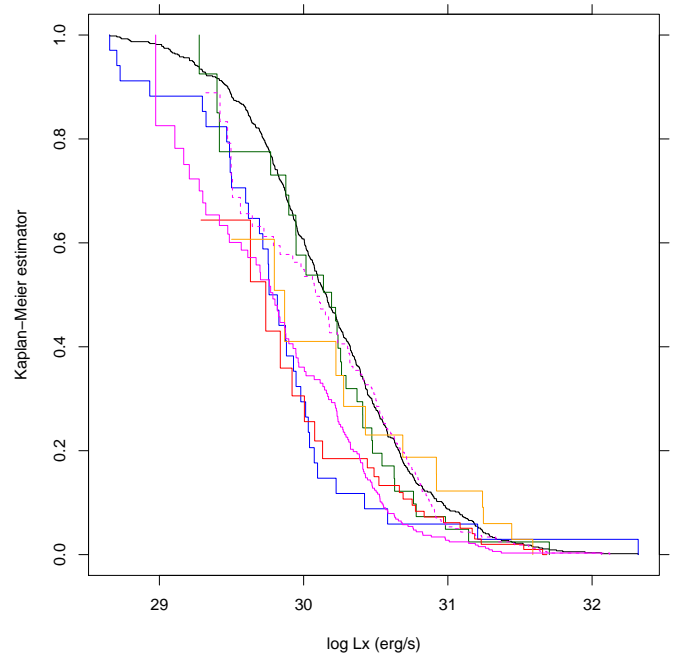


Fig. 26. Maximum-likelihood X-ray luminosity functions, for the entire NAP sample (black), and different subsamples: unreddened M dwarfs (blue), H58 stars (dark green), RGS11 YSOs of Class II (solid magenta), Class I (orange), and flat-spectrum YSOs (red). The dashed magenta distribution refers to Class II YSOs, using different absorption N_H , see text.

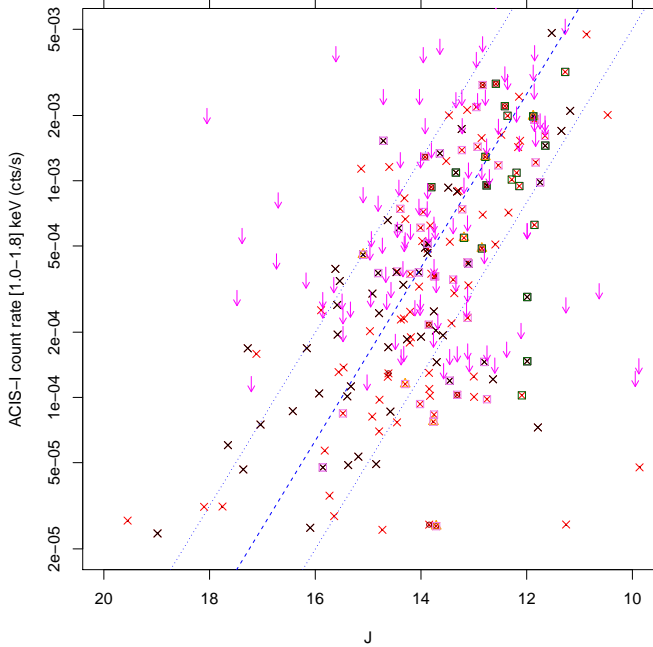


Fig. 25. ACIS-I count rate in the [1.0–1.8] keV band vs. J magnitude. The dashed/dotted lines represent proportionality; the distance between the dotted lines is an order magnitude difference in the X-ray to J flux ratio. Symbols as in Figs. 9 and 10, except for black crosses representing a spatially-selected subset of X-ray sources (see text). Arrows indicate count-rate upper limits to undetected RGS11 YSOs.

tially account for the correlation seen in the diagram, while the spread above and below that line reflects the X-ray to photospheric flux ratio. Most of the H58 stars have X-ray/NIR flux ratios within an order of magnitude. Their average ratio is also close to that of the bulk of NAP X-ray sources; only four of them show weaker X-ray/NIR flux ratio. Also the RGS11 YSOs appear well mixed with the non-YSO X-ray sources, and count-rate upper limits for X-ray undetected YSOs (arrows in the Figure) are consistent with detections. The black crosses in the diagram are X-ray sources in the dashed rectangles in Figs. 20 and 21: also these sources do not appear to have particularly high or low X-ray/NIR flux ratios, and are therefore homogeneous with the rest of NAP X-ray sources.

We have estimated X-ray luminosities L_X for our X-ray sources, using PIMMS to compute conversion factors between count-rate and flux. These are weakly dependent on the emitting plasma temperature if this is above 1 keV, as often found in active PMS stars, but vary considerably as a function of N_H , across the range of inferred absorption values for our NAP sources. As above, we estimated N_H for individual sources from their $J - H$ color, and using the above conversion between this and A_V , and between A_V and N_H . Since we do not know individual distances for possible foreground stars, we might be overestimating L_X for these latter. The derived L_X distribution is shown in Figure 26, for both the total NAP X-ray sample and selected subsamples. The total sample and the X-ray emitting M dwarfs are X-ray selected samples, and therefore do not include upper limits. For independently-selected samples such as H58 stars and RGS11 YSOs we have instead computed individual L_X upper limits using PW(X)Detect; these are used to compute maximum-likelihood X-ray luminosity functions, us-

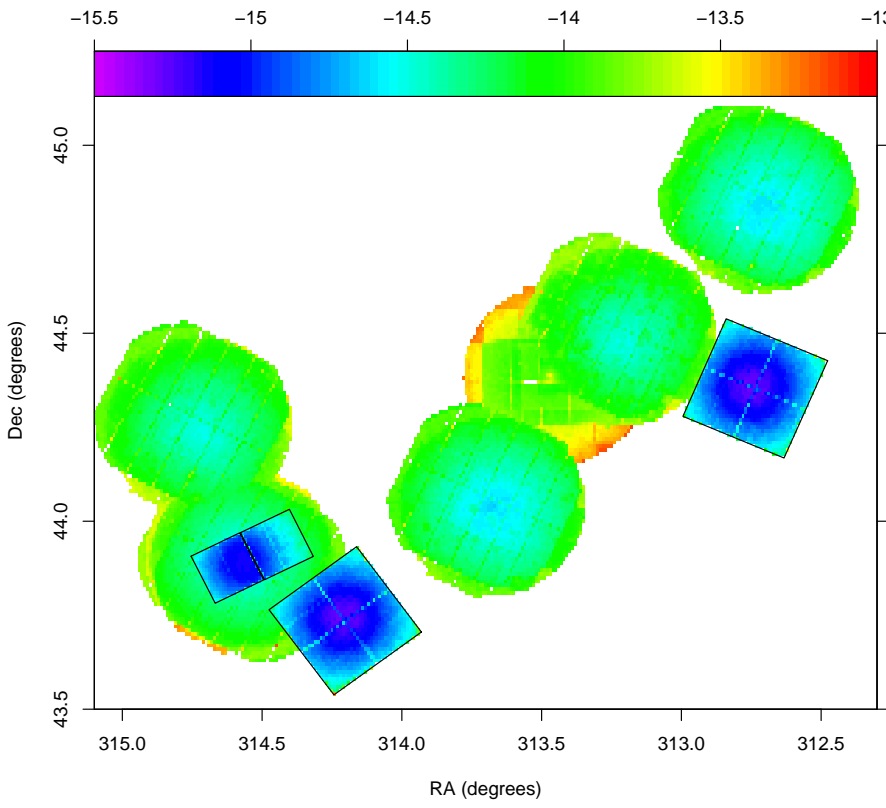


Fig. 27. Map of X-ray sensitivity across our survey. Color indicates $\log f_x$ (top-axis scale, in units of $\text{erg s}^{-1} \text{cm}^{-2}$), where f_x is the minimum detectable X-ray flux at a reference energy of 1 keV. At the NAP distance, $\log f_x = -15$ corresponds to an (unabsorbed) X-ray luminosity $\log L_x \sim 28.6 \text{ erg/s}$.

ing the *survival* R software package³, shown in Fig. 26. With less than 20% of objects detected in X-rays, our sampling of the X-ray properties of flat-spectrum and Class I YSOs is rather poor, compared to the >60% X-ray detections among Class 0-I YSOs in the ONC by Prisinzano et al. (2008); nevertheless, the L_X medians for the flat-spectrum and Class I YSOs from Fig. 26 fall very close to the L_X median of Class 0-Ib objects in Prisinzano et al. (2008; note that YSO classification was made differently by these authors and RGS11). The X-ray luminosity function of RGS11 Class II YSOs (33% detection rate) also has a median $L_X \sim 29.75$ (erg/s), which compares well to the Preibisch and Feigelson (2005) results for the ONC M stars (median $L_X \sim 29.55$ erg/s), but is significantly lower than the median L_X of more massive stars in the ONC (or NGC 2264, or Chamaeleon: median $L_X \sim 29.9 - 30.5$ erg/s). We have however found from our color-color diagrams that only a minor fraction of our X-ray sources are consistent with M-star colors. One possible solution to this contradiction is that we might be strongly underestimating absorption N_H , and with it also L_X , since we probably underestimated $E(J - H)$ as discussed above, if these stars' masses are much above $\sim 0.5M_\odot$. To test this, we have computed the maximum $E(J - H)$ (and corresponding N_H) for each star, assuming an intrinsic value $(J - H)_0 = 0.15$, appropriate to $1.4M_\odot$ stars at 100 Myr (Fig. 15), but definitely not to $0.5M_\odot$ stars: the resulting X-ray luminosity function for Class II YSOs is shown (dashed) in Fig. 26: the resulting median $\log L_X \sim 30.1$ is closer to the ONC value, and even more to the values for NGC 2264 and Chamaeleon stars in Preibisch and Feigelson (2005) for the mass range $0.5 - 0.9M_\odot$, but remains a factor ~ 2 below the median L_X for stars in the mass range $0.9 - 1.2M_\odot$ in the same clusters, for which $E(J - H)_0 = 0.15$

would be most appropriate. Therefore, reddening underestimates may be only a partial explanation of the low X-ray luminosity function of Class II objects in the NAP.

The H58 stars, most of which are not M stars, and which are only lightly absorbed, as seen above, have higher L_X than the Class II YSOs (solid magenta line in Fig. 26), well consistent with PMS stars in the mass range $M = 0.5 - 0.9M_\odot$ from the different clusters shown by Preibisch and Feigelson (2005).

The unreddened M dwarfs have a L_X distribution much lower than the bulk of NAP sources; if they are NAP members, the lower L_X would not be surprising, since these stars are at the lower end of the mass spectrum (Fig. 19) and their L_X distribution of Fig. 26 is close to that of similar-mass stars in the ONC (e.g. Preibisch and Feigelson 2005). However, we cannot rule out that these are M stars with ages similar to the Pleiades (~ 100 Myr), 3-10 times nearer to us, so that their actual L_X would be 10-100 times lower than shown in Fig. 26: also in this case their L_X distribution would agree with the data presented in Preibisch and Feigelson (2005; fig.4).

5.8. X-ray sensitivity limits

It is important to recognize to what extent the results presented above may be affected by the uneven sensitivity of the available X-ray data. As discussed in detail e.g. by Broos et al. (2011), two distinct causes contribute to the effect that an astrophysical object with a given intrinsic X-ray flux (at the NAP distance) may be detected or not. The first cause is instrumental, the detection sensitivity being not uniform across the imaged FOV, because of both mirror vignetting and PSF off-axis degradation. The second cause is of astrophysical origin and resides in the uneven column density of absorbing matter along the line of sight to the source, which was seen above to span a wide range inside the surveyed

³ <http://cran.r-project.org/web/packages/survival>

region. Therefore, we try here to quantitatively examine both effects individually.

The instrument-related effects are relatively easy to model, once the background level of each individual X-ray observation is measured, and properties like vignetting and PSF shape are known. If the spatial distribution of X-ray sources is wide enough, this gives rise to what was termed the “egg-crate effect” by Broos et al. (2011), since the smaller PSF near the (ACIS-I) FOV center results in a larger spatial density of detections there, with respect to FOV borders. We have computed nominal minimum detectable fluxes f_x (for point sources) for the entire NAP survey area using the capabilities of PW(X)Detect: the resulting map is shown in Figure 27, including both ACIS and EPIC pointings. In order to compare different detectors in the same map, we cannot use purely instrumental quantities (counts/sec), but physical ones, scaling counts to erg/cm² with the adoption of the nominal instrument effective area at a representative energy of 1 keV. Since the two ACIS-I ObsIDs 13647 and 15592 were analyzed together and the ACIS-S ObsID 14545 has higher sensitivity than ACIS-I datasets, all ACIS fields span approximately the same range of f_x . Instead, the various XMM-Newton EPIC exposures are of unequal duration (see Table 1), and their f_x is more sensitive to background than ACIS datasets: therefore, despite the more uniform PSF they collectively span a wider range of f_x . This is more clearly seen in the f_x histograms of Figure 28, separately for ACIS and EPIC data: most of the width of the EPIC histogram is related to ObsId-to-ObsId variations, while most of the width of the ACIS histogram is related to center-to-border effects, the various ACIS FOV having similar f_x ranges.

The strong center-to-border f_x variation in ACIS datasets is responsible for the egg-crate effect, when this is found. However, the distribution of X-ray detections in NAP ACIS-I FOVs (Figure 21) does not show such a centrally-symmetric shape, so we may conclude that any egg-crate effect is not primarily responsible for the observed spatial distribution of NAP X-ray sources. As far as other effects are concerned, it is interesting to observe from Figure 25 (including only ACIS-I data) that upper limits span a wide range of almost two orders of magnitude, because they are computed on the basis of the individual source absorption values. The fact that they are even more frequent in the upper part of the diagram emphasizes that absorption, more than uneven detector properties, is the most important factor against their detection. This emerges also clearly from a comparison between the range in the ordinates of Figure 25 of 2.5 orders of magnitude, and that spanned by the instrumental ACIS sensitivity (one order of magnitude) in the red histogram of Figure 28.

The distribution of absorption-based (from $J - H$ colors) X-ray count-rate-to-flux conversion factors is shown in Figure 29, separately for ACIS and EPIC detectors (and regardless of whether each detector actually imaged a given source), under the same assumptions about the intrinsic source spectrum as in the previous subsection. For both instruments, the bulk of stars span approximately 1.5 orders of magnitude, in agreement with conclusions given just above. While the total NAP cloud absorption shows definite spatial properties (Figure 17), the X-ray colors (Figures 4 to 6) and NIR colors (Figures 20 and 21) of X-ray sources are not generally correlated with the local total depth. This suggests that X-ray sources are located at various depths in the cloud, and the extrapolation of the undetected source density on the basis of the local density of detections is here at risk of being misleading. Such an approach was instead used by e.g. Kuhn et al. (2015) in their X-ray study of several massive SFRs, in which absorption is more uniform and source statistics (per FOV) is much higher than in the NAP,

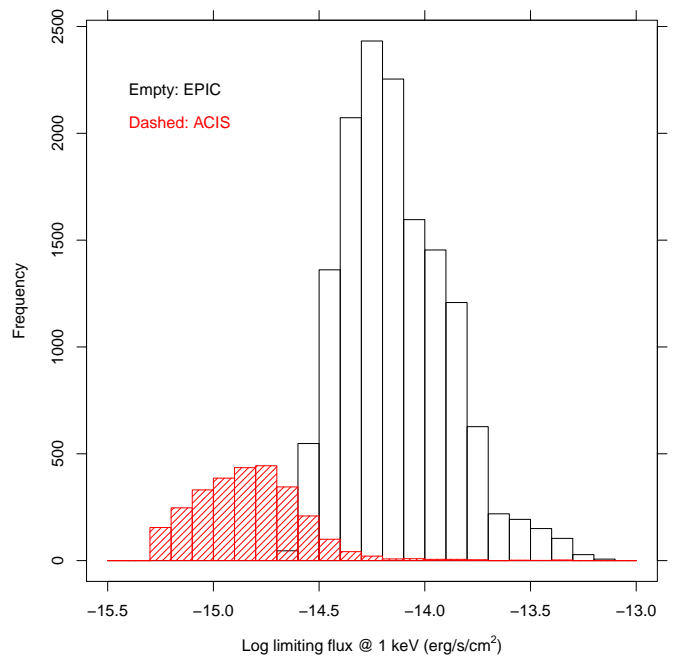


Fig. 28. Histograms of minimum detectable flux f_x from the same spatial grid as in Fig. 27, shown separately for ACIS (red) and EPIC data (black).

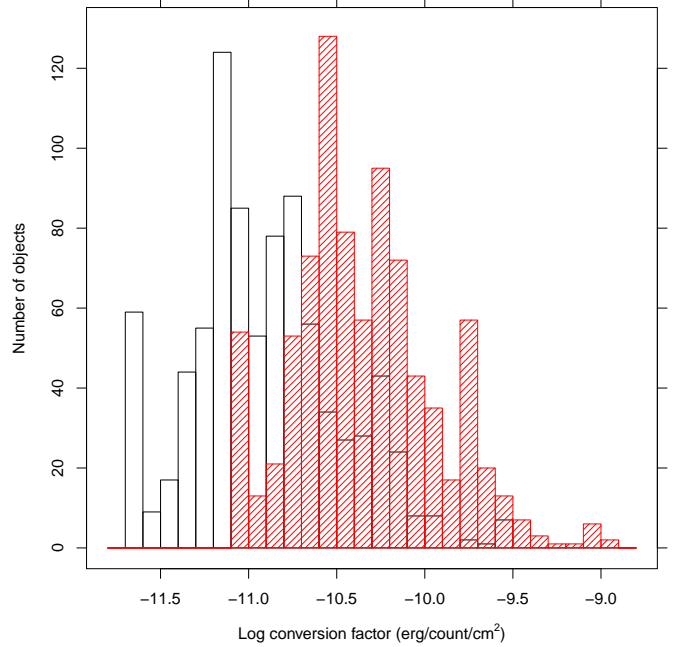


Fig. 29. Distribution of computed count-rate to flux conversion factors for all observed NIR objects (either X-ray detected or not), separately for ACIS (red) and EPIC (black) observations.

permitting a believable reconstruction of the undetected population. Contrarily to the data studied by Kuhn et al. (2015), in the NAP dataset the flux completeness limit (a flux above which we are confident to have detected near 100% of sources) is near the upper end of the detected source range, as can be understood from Figure 25 where upper limits are found up to the top of the count-rate scale; this also renders the approach adopted by those authors unapplicable here. The conclusion drawn from

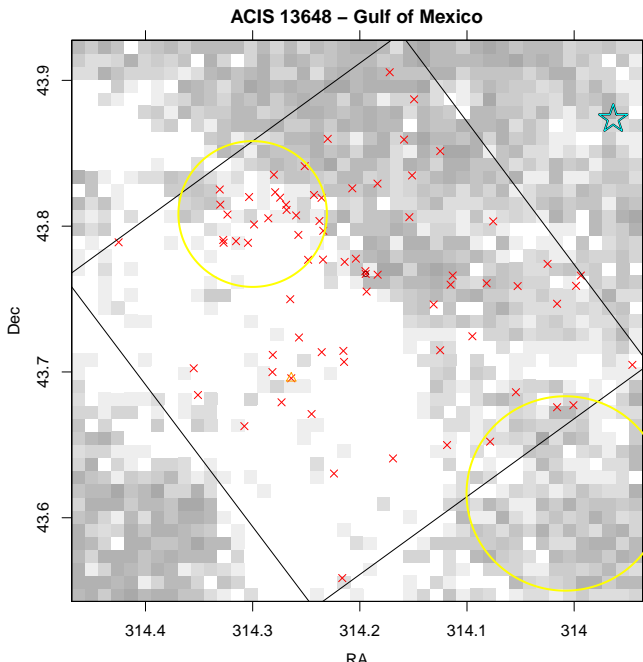


Fig. 30. Analogous of Fig. 21 (lower-left panel), but leaving out all X-ray detections with less than 15 counts. No optical/NIR objects are plotted here in order to show better the X-ray source distribution. The big yellow circles are Cambresy's IR clusters, and the cyan star symbol is the O5 star, as in Fig. 21.

Figure 29 is that the intrinsic X-ray luminosities of undetected sources may range up to 1.5 orders of magnitude above their unabsorbed value, whose spatial distribution was shown in Figure 27. The peaks of the instrumental-sensitivity and conversion-factor histograms, taken together, correspond to an intrinsic X-ray luminosity $\log L_x \sim 29.9$ erg/s, detectable over most of the NAP fields. This L_x value being typical of low-mass PMS stars, we conclude that our NAP detection list can be considered representative of the young star population in this SFR.

While a proper reconstruction of the space and flux distributions of undetected NAP sources is unfeasible, we may nevertheless mitigate the instrumental effects described above, by considering only detections above a uniform threshold for a given X-ray FOV. Figure 30 shows the detected X-ray sources in the “Gulf of Mexico” ACIS FOV, already shown in Fig. 21 (lower-left panel), but limited to sources with more than 15 counts, and therefore detectable across the whole FOV (thus free from eggcrate effects). Although the source statistics becomes smaller, the non-uniform spatial distribution of detections is still clear, especially near one of the Cambresy's NIR clusters. Therefore, the main conclusions of the previous subsections are not dramatically affected by instrumental factors.

6. Discussion

The results reported in the above sections emphasize once again the known complexity of the NAP star formation region, made of several subgroups of young stars (Cambrésy et al. 2002, RGS11), with no obvious connection between them. Although it was very difficult to assess individual membership for our X-ray detected sources, above results show that many (or most) of them exhibit properties (X-ray/NIR flux ratios, X-ray variability and spectrum hardness) consistent with young PMS stars. The non-detection in the X-rays of most YSOs, even those of Class II

whose X-ray properties are best known, remains puzzling, since optical/NIR color-color diagrams seem to rule out for most of them the low mass values ($M < 0.5 M_\odot$) that their X-ray luminosity function would imply. A better characterization of these objects would be desirable.

Perhaps the spatial distribution of our X-ray sources is our most interesting result. Although the illuminating O5 star 2MASS J20555125+4352246 does not fall in any of our X-ray FOVs, we observed its immediate neighborhood, a few arcmin away from it: there is no sign of any concentration of X-ray sources around it, in agreement with the finding by its discoverers that it is remarkably isolated (Comerón and Pasquali 2005). This isolation refers therefore not only to comparably massive stars, but to stars down to solar-like masses, to which our survey is sensitive even at the extinction of the O5 star. This is very different from most star-forming regions, where the highest-mass stars are immediately surrounded by low-mass PMS stars. It would be interesting to investigate if this is a runaway star, with implications on the timescales on which it might have interacted with the molecular cloud; although no such information is available now, the Gaia data should provide it in a short time frame.

The two sub-regions with the highest YSO spatial density, the Gulf of Mexico and Pelican, are also those with the largest number of X-ray detections (although this might be somewhat biased by having used there the most sensitive ACIS detectors). In the Gulf of Mexico, closest to the O5 star, there is a clear spatial trend: YSOs are clustered near the border of the dark cloud which faces the O star (and not inside the cloud), and tens of X-ray sources follow the same pattern; moreover, several other tens X-ray sources are found between the YSO cluster(s) and the O star, forming an apparently distinct layer. It is interesting to remark that in Figure 20 of RGS11 the Class III stars fall in this same intermediate region. This is highly suggestive of a time sequence, with formation of stars proceeding southwards, under the strong influence of the massive O star nearby. The X-ray sources without a YSO counterpart, as well as the Class III stars, would thus be the oldest, with younger stars being currently formed in the outer layers of the dense dust cloud. Toujima et al. (2011) also suggested triggered star formation in NGC 7000, on the basis of molecular-line observations. The disk-free X-ray detected stars are not necessarily much older than the others (no such separation is found in our de-reddened CMD), since when exposed to strong UV irradiation disk lifetimes are likely to be significantly shortened (e.g. Guarcello et al. 2007, 2009). In other places in the NAP, a similar segregation between the YSO and X-ray source distributions is observed, as in the “Pelican hat”, but its origin is much less clear, since the triggerer of the possible time sequence is not obvious. Moreover, we recover at least three of the Cambrésy et al. (2002) NIR clusters in X-rays, confirming their existence.

The assessment of membership for the X-ray detected sources was difficult, as discussed above for each of the possible indicators. Only $\sim 29\%$ of all X-ray sources have H α or NIR excesses (either from this work or from RGS11 and H58), and are therefore high-probability members individually. Most other X-ray sources have however X-ray properties, colors and extinction very similar to the former, and are probable members as well. The foreground extinction towards the NAP is very small, as we find from color-color diagrams and in agreement with Laugaly et al. (2006, 2007), and therefore foreground X-ray sources may only be found at near-zero reddening: we found only a few tens such sources above. Extinction rises rather abruptly in the NAP, although this may be position-dependent as we have examined

above (in agreement with Cambrésy et al. 2002). Background X-ray sources, behind such large absorbing column, are unlikely to be coronal sources, but may be distant compact objects or even AGNs, both characterized by large X-ray-to-optical flux ratios. We tentatively identify these classes of sources with our unidentified X-ray sources (115 out of 721 total detections), which must have large X-ray-to-optical flux ratios if they are missed in both of the very deep IPHAS/UKIDSS catalogs. To summarize, most of the NAP X-ray sources with an optical/NIR counterpart, except perhaps a significant fraction of the unreddened ones, are good candidates as young NAP members.

7. Summary

We have performed the first extensive, wide-area X-ray survey of the North-America and Pelican star-forming region, using both Chandra/ACIS and XMM-Newton/EPIC detectors. More than 700 unique X-ray sources have been detected, of which $\sim 85\%$ have a counterpart in at least one of the IPHAS/UKIDSS/2MASS catalogs. Only $\sim 29\%$ of X-ray sources are identified with previously known YSOs or CTTS, or with newly found H α -emission or NIR-excess stars. We argued that most of the optically/NIR identified X-ray sources are probable members of the star-forming region. A few tens unreddened X-ray sources are probable active foreground low-mass stars.

In the Gulf-of-Mexico region, the respective spatial properties of dark obscuration, YSOs, and X-ray sources without YSO association are suggestive of a sequential star-formation scenario, with the O5 star illuminating the entire nebula as the probable triggerer. Unlike most star-forming regions, this most massive star appears isolated even in X-ray images. The large-scale spatial distribution of the X-ray detected member candidates follows qualitatively that of the known YSOs, with several sub-clusters, apparently physically unconnected.

Detailed follow-up (spectroscopic) observations will be needed to confirm individual membership of the X-ray sources found here.

Appendix A: 2MASS - UKIDSS calibration

The UKIDSS J, H, K photometric system is calibrated to the 2MASS system (Hodgkin et al. 2009); however, the calibration was made at low reddening, and we find that small adjustments are required to match the two catalogs at large reddening values, typical of the NGC 7000/IC 5070 region. The difference between 2MASS and UKIDSS J magnitudes is shown in Figure A.1: although small, this difference is often significant compared to the very small errors in the UKIDSS magnitudes. Only objects with errors < 0.07 mag in both J bands, and errors < 0.1 mag in $(J - H)_{UKIDSS}$, are shown. A least-square fit to the data (with fixed zero intercept) has the form:

$$J_{2MASS} - J_{UKIDSS} = 0.0188 (J - H)_{UKIDSS}. \quad (\text{A.1})$$

The $J - H$ colors differ between 2MASS and UKIDSS more appreciably, however, by almost 8% (Figure A.2, where only objects with errors < 0.1 mag in both $(J - H)_{UKIDSS}$ and $(J - H)_{2MASS}$ are shown). The best fit to the data (with zero intercept) has the form:

$$(J - H)_{UKIDSS} = 0.9217 (J - H)_{2MASS}. \quad (\text{A.2})$$

Similarly, Figure A.3 shows the comparison between the respective $H - K$ colors, with the best fit here given by:

$$(H - K)_{UKIDSS} = 1.04236 (H - K)_{2MASS}. \quad (\text{A.3})$$

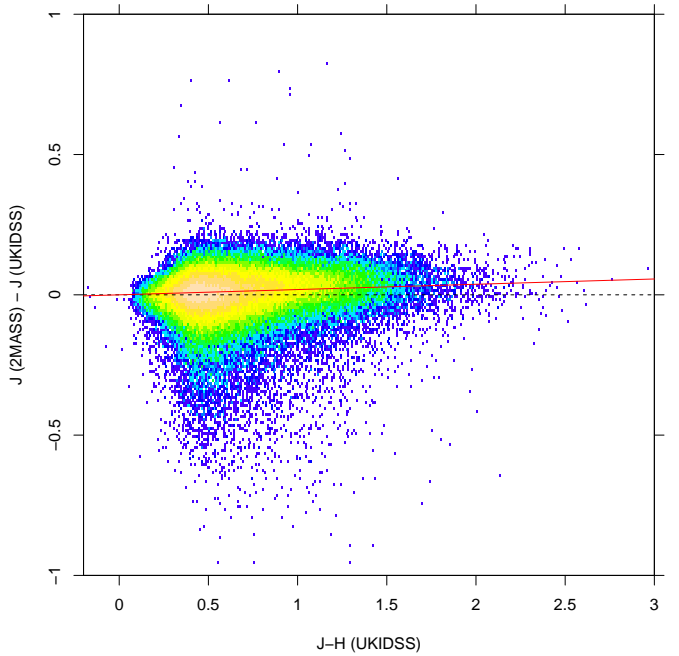


Fig. A.1. 2MASS-UKIDSS comparison: difference $J_{2MASS} - J_{UKIDSS}$ vs. UKIDSS $J - H$ color (2-D histogram). The black dashed line represents $J_{2MASS} - J_{UKIDSS} = 0$, while the red solid line is a best-fit to the data.

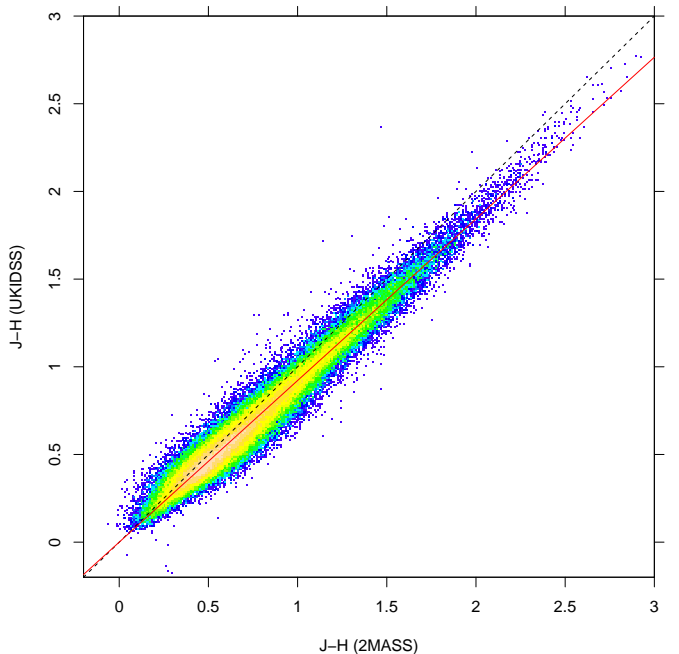
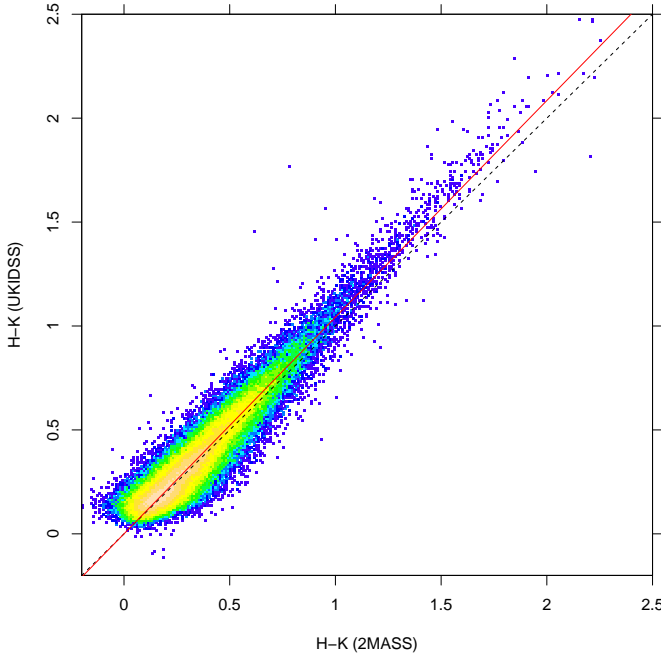
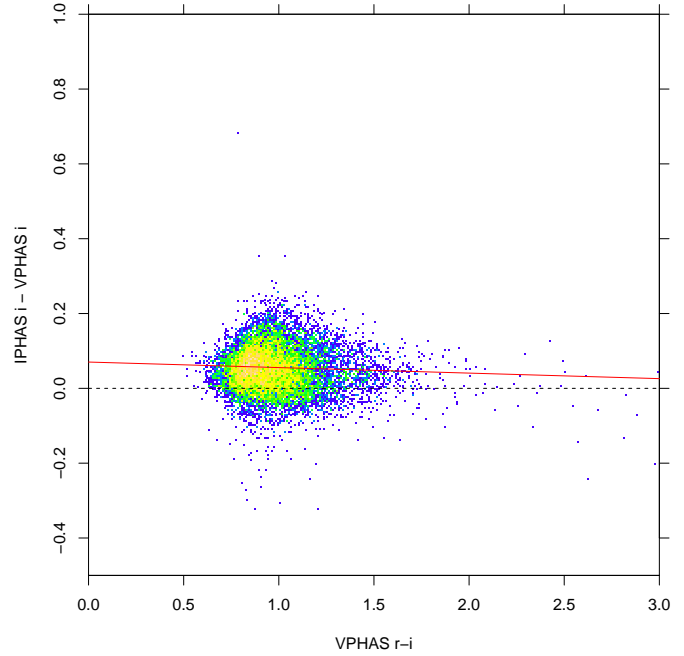
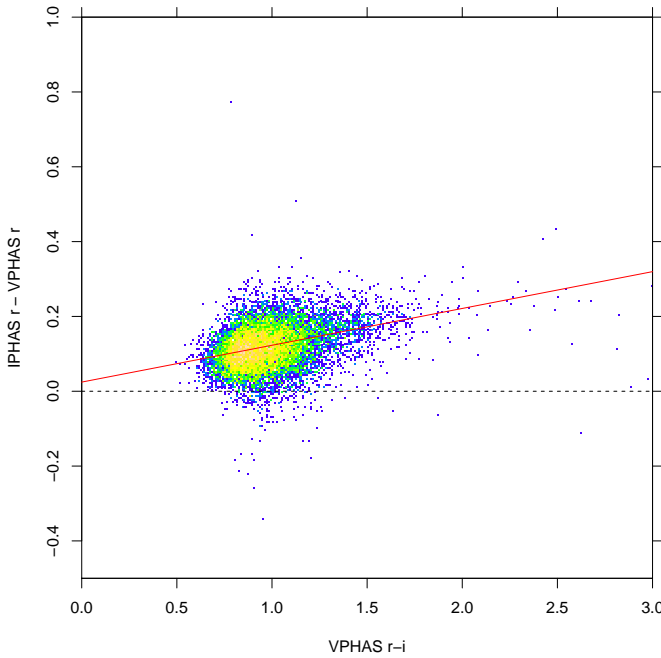


Fig. A.2. Comparison between $J - H$ colors from 2MASS and UKIDSS. The black dashed line represents $(J - H)_{2MASS} = (J - H)_{UKIDSS}$, while the red solid line is a best-fit to the data.

All UKIDSS magnitudes were therefore rescaled according to the $(J - H)_{UKIDSS}$ color, to match the 2MASS photometric system even at large reddening. At low reddening (low $J - H$), this recalibration is irrelevant, and does not interfere with the one presented by Hodgkin et al. (2009). After recalibration, we merged the 2MASS and UKIDSS catalogs into a single NIR

**Fig. A.3.** Same as Fig. A.2, for $H - K$.**Fig. B.2.** Same as Fig. B.1, for the i band.**Fig. B.1.** IPHAS-VPHAS+ comparison: difference $r_{\text{IPHAS}} - r_{\text{VPHAS}}$ vs. VPHAS+ $r - i$ color (2-D histogram). The black dashed line represents $r_{\text{IPHAS}} - r_{\text{VPHAS}} = 0$, while the red solid line is a best-fit to the data.

source catalog, choosing the more precise UKIDSS magnitudes when available.

Appendix B: IPHAS - VPHAS+ calibration

Although the IPHAS r, i photometric system is similar to the Sloan Survey system, the formulae in Barentsen et al. (2014) indicate that significant differences exist between the two systems. Moreover, no recipe is given to convert the IPHAS r, i magnitudes into Johnson/Cousin VRI magnitudes. Such a recipe is in-

stead given by Drew et al. (2014) for the VPHAS+ $ugriz$ magnitudes, which are closely related to the IPHAS filter system. The BHAC evolutionary tracks and isochrones, moreover, are currently available for the $UBVRI$ filters, but not for either the Sloan or the IPHAS/VPHAS+ filters, so we attempt here to re-calibrate the IPHAS r, i magnitudes in terms of the VPHAS+ r, i , whose relation with VRI is known from Drew et al. (2014). We consider an equatorial field where both IPHAS and VPHAS+ data are available, to study their photometric differences. The results of this experiment are shown in Figures B.1 and B.2, where only objects with errors < 0.05 mag in all bands are shown. The best-fit relations shown in these Figures are:

$$r_{\text{IPHAS}} - r_{\text{VPHAS}} = 0.02448 + 0.0984 (r - i)_{\text{VPHAS}} \quad (\text{B.1})$$

$$i_{\text{IPHAS}} - i_{\text{VPHAS}} = 0.070283 - 0.01477 (r - i)_{\text{VPHAS}}. \quad (\text{B.2})$$

These relations (together with those given in Drew et al. 2014) were used to convert the BHAC tracks/isochrones in the Johnson/Cousin filters into the appropriate IPHAS r, i magnitudes and colors.

Appendix C: Reddening law

We study here the empirical reddening law for the NGC 7000/IC 5070 region, in the r, i, J, H, K bands. With respect to previous studies, we benefit here from an extensive optical/NIR catalog, reaching down to faint magnitudes with small photometric errors. Thanks to these properties, we are able to discern in several color-color diagrams the giant-star locus from the dwarfs locus. Figure C.1 shows the $(J - H, H - K)$ diagram of all sources in the studied region: the reddened red-giant sequence starts at $J - H \sim 0.8$, whereas the dwarf sequence starts at $J - H \sim 0$, but the giants being more luminous remain observable up to larger reddening values. We have therefore visually fitted the giant sequence with the red line in the Figure

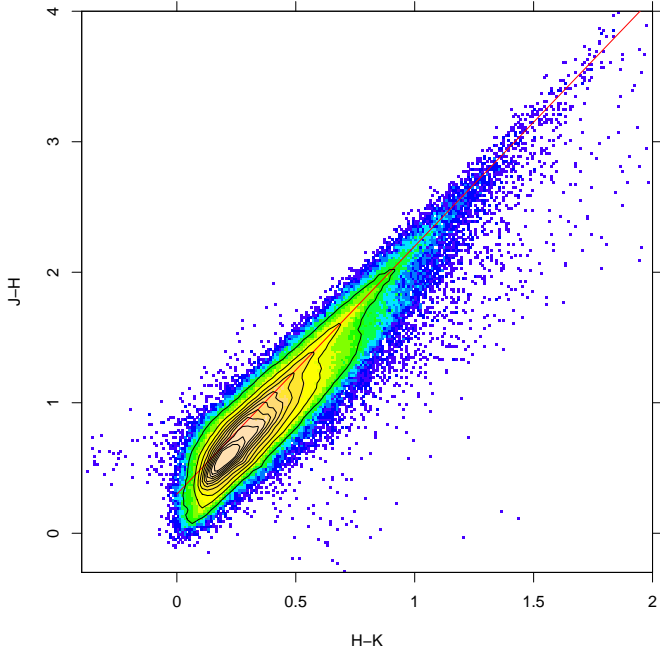


Fig. C.1. Slope of reddening vector ($E(J - H)/E(H - K) = 1.9$) in the ($J - H, H - K$) plane (red line), obtained from the giant-star sequence, which is best seen from the iso-density contours (black).

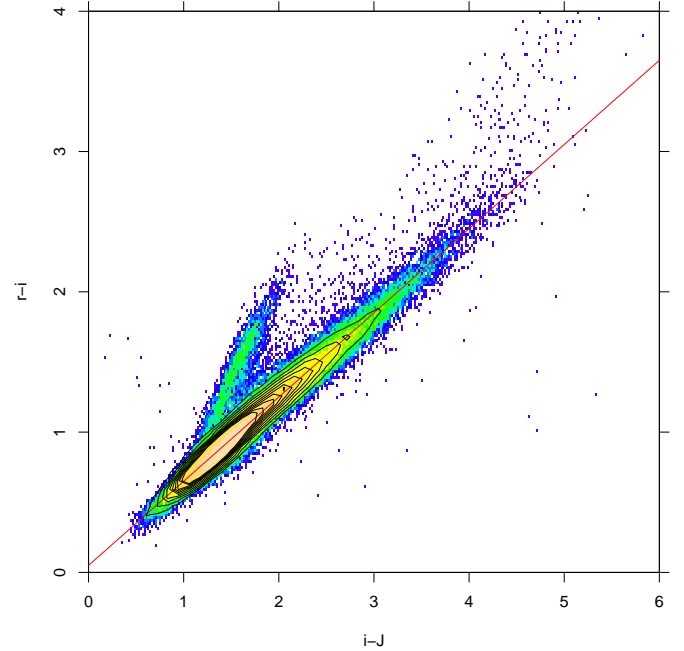


Fig. C.3. Same as Fig. C.1, for the ($r - i, i - J$) plane: the reddening-vector slope is here $E(r - i)/E(i - J) = 0.6$.

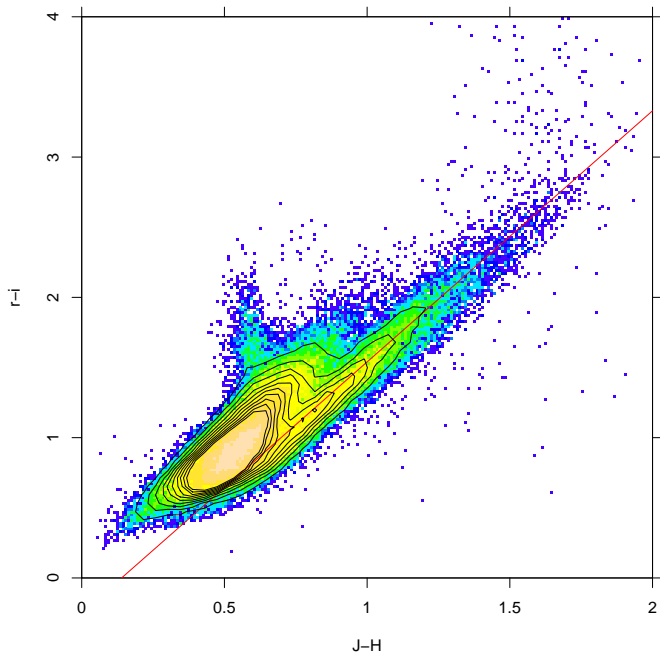


Fig. C.2. Same as Fig. C.1, for the ($r - i, J - H$) plane: here the reddened giant-star sequence is particularly well distinct from the reddened main sequence, while the unreddened M-dwarf locus protrudes upwards near $J - H \sim 0.6$. The reddening-vector slope is here $E(r - i)/E(J - H) = 1.79$.

line, since this would mix together stars with different intrinsic NIR colors, and the resulting slope would be higher than the true one. The upper envelope of datapoints in the Figure also agrees with the slope we estimate from the giant sequence.

Figure C.2 is a mixed optical/NIR ($r - i, J - H$) diagram, where we can discern well the reddened giant sequence (the lowest one, including the highest-reddening stars) from the dwarf sequence. Protruding upwards, the M-dwarf sequence is also clearly seen (cf. Fig. 12). The reddening vector has a slope of $E(r - i)/E(J - H) = 1.79$.

In the ($r - i, i - J$) diagram of Figure C.3, instead, the dwarf and giant sequence are not distinct, but the M-dwarfs are. The reddening-vector slope is here $E(r - i)/E(i - J) = 0.6$.

In order to connect these reddening laws to the V -band extinction, and to obtain the total-to-selective extinction ratio $A_i/E(r - i)$ for the IPHAS filters, we need two more equations. Assuming that the J band is least affected by peculiar reddening laws, we therefore take from Rieke and Lebofsky (1985) the ratios $A_J/A_V = 0.282$ and $E(J - H)/A_V = 0.107$. The set of relative extinctions A_λ/A_V for the NAP thus becomes:

$$A_r/A_V = 0.793 \quad (\text{C.1})$$

$$A_i/A_V = 0.601 \quad (\text{C.2})$$

$$A_J/A_V = 0.282 \quad (\text{C.3})$$

$$A_H/A_V = 0.175 \quad (\text{C.4})$$

$$A_K/A_V = 0.1187 \quad (\text{C.5})$$

(with slope $E(J - H)/E(H - K) = 1.9$). It should be remarked that at low reddening dwarfs dominate the distribution because of their higher spatial density, but at large reddening giants dominate being observable up to larger distances: it is therefore incorrect to derive the reddening vector slope by simply joining the low and high ends of the color distribution with a straight

where equations C.3 and C.4 are merely the Rieke and Lebofsky (1985) relations, included for convenience.

Acknowledgements. We wish to thank an anonymous referee for his/her helpful suggestions. I.P. acknowledges support by Chandra fund 16617814 contract GO2-13021X. The scientific results reported in this article are based on observations made by the Chandra and XMM-Newton X-ray Observatories. This paper also makes use of data obtained as part of the INT Photometric H α Survey of the Northern Galactic Plane (IPHAS, www.iphas.org) carried out at the Isaac Newton Telescope (INT). The INT is operated on the island of La Palma by the Isaac Newton Group in the Spanish Observatorio del Roque de los Muchachos of the Instituto de Astrofísica de Canarias. All IPHAS data are processed by the Cambridge Astronomical Survey Unit, at the Institute of Astronomy in Cambridge. The bandmerged DR2 catalogue was assembled at the Centre for Astrophysics Research, University of Hertfordshire, supported by STFC grant ST/J001333/1. This publication makes use of data products from the Wide-field Infrared Survey Explorer, which is a joint project of the University of California, Los Angeles, and the Jet Propulsion Laboratory/California Institute of Technology, funded by the National Aeronautics and Space Administration. This research makes use of the SIMBAD database, operated at CDS, Strasbourg, France. We also make heavy use of R: A language and environment for statistical computing. R Foundation for Statistical Computing, Vienna, Austria. (<http://www.R-project.org/>).

References

- Armond, T., Reipurth, B., Bally, J., & Aspin, C. 2011, A&A, 528, A125
 Aspin, C. 2011, AJ, 141, 196
 Bally, J., & Reipurth, B. 2003, AJ, 126, 893
 Bally, J., Ginsburg, A., Probst, R., et al. 2014, AJ, 148, 120
 Baraffe, I., Homeier, D., Allard, F., & Chabrier, G. 2015, A&A, 577, A42
 Barentsen, G., Farnhill, H. J., Drew, J. E., et al. 2014, MNRAS, 444, 3230
 Broos, P. S., Townsley, L. K., Feigelson, E. D., et al. 2011, ApJS, 194, 2
 Cambrésy, L., Beichman, C. A., Jarrett, T. H., & Cutri, R. M. 2002, AJ, 123, 2559
 Comerón, F., & Pasquali, A. 2005, A&A, 430, 541
 Corbally, C. J., Straizys, V., & Laugalys, V. 2009, Baltic Astronomy, 18, 111
 Covey, K. R., Hillenbrand, L. A., Miller, A. A., et al. 2011, AJ, 141, 40
 Damiani, F., Maggio, A., Micela, G., & Sciortino, S. 1997, ApJ, 483, 350
 Damiani, F., Maggio, A., Micela, G., & Sciortino, S. 1997, ApJ, 483, 370
 Damiani, F., Prisinzano, L., Micela, G., & Sciortino, S. 2006, A&A, 459, 477
 Dunham, M. M., Arce, H. G., Bourke, T. L., et al. 2012, ApJ, 755, 157
 Drew, J. E., Greimel, R., Irwin, M. J., et al. 2005, MNRAS, 362, 753
 Drew, J. E., Gonzalez-Solares, E., Greimel, R., et al. 2014, MNRAS, 440, 2036
 Favata, F., Flaccomio, E., Reale, F., et al. 2005, ApJS, 160, 469
 Favata, F., & Micela, G. 2003, Space Sci. Rev., 108, 577
 Gorenstein, P. 1975, ApJ, 198, 95
 Green, J. D., Evans, N. J., II, Kóspál, Á., et al. 2011, ApJ, 731, L25
 Guarcello, M. G., Prisinzano, L., Micela, G., et al. 2007, A&A, 462, 245
 Guarcello, M. G., Micela, G., Damiani, F., et al. 2009, A&A, 496, 453
 Guarcello, M. G., Damiani, F., Micela, G., et al. 2010, A&A, 521, A18
 Güdel, M., Guinan, E. F., & Skinner, S. L. 1997, ApJ, 483, 947
 Guiet, S., Rebull, L. M., Stauffer, J. R., et al. 2009, ApJ, 697, 787
 Herbig, G. H. 1958, ApJ, 128, 259
 Hodgkin, S. T., Irwin, M. J., Hewett, P. C., & Warren, S. J. 2009, MNRAS, 394, 675
 Kalari, V. M., Vink, J. S., Drew, J. E., et al. 2015, MNRAS, 453, 1026
 Kóspál, Á., Ábrahám, P., Acosta-Pulido, J. A., et al. 2011, A&A, 527, A133
 Kuhn, M. A., Getman, K. V., & Feigelson, E. D. 2015, ApJ, 802, 60
 Laugalys, V., Straizys, V., Vrba, F. J., et al. 2006, Baltic Astronomy, 15, 327
 Laugalys, V., Straizys, V., Vrba, F. J., et al. 2006, Baltic Astronomy, 15, 483
 Laugalys, V., Straizys, V., Vrba, F. J., et al. 2007, Baltic Astronomy, 16, 349
 Lawrence, A., Warren, S. J., Almaini, O., et al. 2007, MNRAS, 379, 1599
 Lee, J.-E., Park, S., Green, J. D., et al. 2015, ApJ, 807, 84
 Liebhart, A., Güdel, M., Skinner, S. L., & Green, J. 2014, A&A, 570, L11
 Lin, D., Webb, N. A., & Barret, D. 2012, ApJ, 756, 27
 Miller, A. A., Hillenbrand, L. A., Covey, K. R., et al. 2011, ApJ, 730, 80
 Pillitteri, I., Sciortino, S., Flaccomio, E., et al. 2010, A&A, 519, A34
 Pillitteri, I., Wolk, S. J., Megeath, S. T., et al. 2013, ApJ, 768, 99
 Preibisch, T., & Feigelson, E. D. 2005, ApJS, 160, 390
 Prisinzano, L., Damiani, F., Micela, G., & Sciortino, S. 2005, A&A, 430, 941
 Prisinzano, L., Micela, G., Flaccomio, E., et al. 2008, ApJ, 677, 401
 Rebull, L. M., Guiet, S., Stauffer, J. R., et al. 2011, ApJS, 193, 25
 Reipurth, B., & Schneider, N. 2008, Handbook of Star Forming Regions, Volume I, 4, 36
 Rieke, G. H., & Lebofsky, M. J. 1985, ApJ, 288, 618
 Semkov, E. H., Peneva, S. P., Munari, U., Milani, A., & Valisa, P. 2010, A&A, 523, L3
 Semkov, E. H., Peneva, S. P., Munari, U., et al. 2012, A&A, 542, A43
 Skinner, S. L., Briggs, K. R., Guedel, M., & Sokal, K. R. 2007, Bulletin of the American Astronomical Society, 39, 62.27
 Straizys, V., Corbally, C. J., & Laugalys, V. 2008, Baltic Astronomy, 17, 125
 Toujima, H., Nagayama, T., Omodaka, T., et al. 2011, PASJ, 63, 1259
 Welin, G. 1973, A&AS, 9, 183
 Witham, A. R., Knigge, C., Drew, J. E., et al. 2008, MNRAS, 384, 1277
 Wright, E. L., Eisenhardt, P. R. M., Mainzer, A. K., et al. 2010, AJ, 140, 1868-1881

Table 3. Detected X-ray sources in the NAP. Full table in electronic format only.

X-ray no.	CXO Id (CXOU)	XMM Id (XMMU)	RA (J2000)	Dec (J2000)	Pos. err. (arcsec)	Count rate (cts/ksec)	Rate error (cts/ksec)	HR1 ACIS	HR2 ACIS	HR1 XMM	HR2 XMM	$\log L_X$ (erg/sec)
1	J205004.0+442249		312.51677	44.38037	1.87	0.428	0.226	0.33	0.60			
2	J205006.2+442505		312.52597	44.41824	2.34	2.067	0.322	0.31	-0.06			30.09
3	J205013.5+441910		312.55631	44.31957	2.56	0.402	0.161	0.00	0.88			
4	J205017.6+442318		312.57358	44.38850	1.48	0.759	0.239	1.00	0.81			
5	J205019.0+442630		312.57958	44.44189	2.45	0.550	0.208	-0.90	0.50			29.99
6	J205020.3+442557		312.58466	44.43271	1.73	0.488	0.185	0.45	-0.07			30.76
7	J205021.7+442425		312.59051	44.40696	1.08	1.937	0.264	0.48	-0.07			29.02
8	J205021.8+442101		312.59113	44.35048	1.12	0.192	0.103	-0.20	0.20			30.39
9	J205022.4+441918		312.59365	44.32169	1.08	1.939	0.258	0.53	-0.24			29.79
10	J205022.9+442224		312.59556	44.37350	1.12	0.181	0.123	NaN	1.00			29.71
11	J205024.1+442222		312.60066	44.37301	1.12	0.221	0.128	0.20	0.14			
12	J205025.6+442633		312.60667	44.44274	2.81	0.361	0.163	-0.14	-0.09			29.91
13	J205026.3+442606		312.60990	44.43526	1.94	0.413	0.184	0.67	-0.43			
14	J205028.2+442205		312.61784	44.36821	0.83	0.158	0.104	NaN	1.00			28.80
15	J205028.8+442301		312.62006	44.38378	0.79	0.177	0.109	-1.00	NaN			
16	J205030.1+441501		312.62557	44.25049	1.40	0.355	0.225	-1.00	1.00			31.23
17	J205030.5+442520		312.62709	44.42243	0.86	1.127	0.192	0.90	0.22			30.34
18	J205031.1+442427		312.62987	44.40758	1.15	0.536	0.185	0.33	0.80			30.19
19	J205033.1+441539		312.63798	44.26084	1.69	1.498	0.235	0.30	-0.28			
20	J205035.0+442514		312.64602	44.42077	1.44	0.232	0.109	-1.00	1.00			29.40
21	J205035.6+441815		312.64838	44.30433	0.86	0.460	0.169	1.00	0.78			30.76
22	J205035.8+442324		312.64924	44.39015	0.54	0.144	0.078	1.00	0.60			30.32
23	J205035.8+441819		312.64958	44.30541	0.83	0.153	0.086	1.00	-0.56			30.18
24	J205036.9+442050		312.65413	44.34725	0.50	0.255	0.121	0.56	-0.40			
25	J205037.0+441825		312.65431	44.30700	0.58	5.570	0.415	0.42	-0.30			
26	J205037.3+442053		312.65580	44.34813	0.32	2.800	0.287	0.13	-0.59			
27	J205037.8+441746		312.65766	44.29612	1.26	0.958	0.174	0.75	-0.05			
28	J205037.9+442512		312.65823	44.42022	0.47	3.010	0.301	0.61	-0.31			30.77
29	J205038.6+441049		312.66086	44.18029	2.66	0.546	0.259	1.00	0.71			30.36
30	J205039.7+442003		312.66583	44.33426	0.43	0.648	0.241	0.33	-0.82			29.63
31	J205040.4+442022		312.66864	44.33951	0.36	0.632	0.197	0.50	-0.67			29.70
32	J205040.5+442051		312.66897	44.34751	0.36	0.173	0.086	0.00	-0.50			29.30
33	J205041.9+441825		312.67467	44.30722	0.50	2.151	0.265	0.94	0.24			31.58
34	J205042.0+442149		312.67531	44.36379	0.47	0.305	0.128	0.00	-0.25			29.80
35	J205042.8+442156		312.67844	44.36561	0.25	2.231	0.270	0.39	0.34			30.86
36	J205042.9+442204		312.67875	44.36791	0.94	0.250	0.107	-0.11	-0.33			29.08
37	J205042.9+442559		312.67875	44.43319	0.72	0.770	0.229	0.73	-0.36			30.38
38	J205043.5+441552		312.68150	44.26465	1.08	0.670	0.218	0.22	-0.22			29.70
39	J205044.0+442058		312.68356	44.34958	0.40	0.499	0.163	1.00	0.58			
40	J205044.4+442535		312.68526	44.42643	0.90	0.146	0.118	-1.00	1.00			30.01
41	J205044.5+441540		312.68579	44.26125	1.98	0.311	0.135	0.33	0.64			
42	J205044.8+441718		312.68684	44.28860	0.65	1.161	0.231	0.86	-0.11			
43	J205044.9+441554		312.68725	44.26522	0.86	1.605	0.225	0.09	-0.57			30.23

Table 3. continued.

X-ray no.	CXO Id (CXOU)	XMM Id (XMMU)	RA (J2000)	Dec (J2000)	Pos. err. (arcsec)	Count rate (cts/ksec)	Rate error (cts/ksec)	HR1 ACIS	HR2 ACIS	HR1 XMM	HR2 XMM	$\log L_X$ (erg/sec)
44	J205045.9+442446	312.69138	44.41302	0.47	0.794	0.150	1.00	0.89				31.44
45	J205045.9+442555	312.69160	44.43202	0.61	0.751	0.296	0.67	0.23				30.36
46	J205046.0+441910	312.69201	44.31950	0.36	2.527	0.264	0.03	-0.82				30.27
47	J205046.5+442446	312.69384	44.41304	0.76	0.196	0.103	1.00	0.50				
48	J205047.0+441729	312.69588	44.29159	0.47	2.614	0.274	0.33	-0.43				30.31
49	J205047.5+441413	312.69832	44.23716	2.56	0.438	0.192	0.33	0.14				29.67
50	J205047.6+441956	312.69862	44.33233	0.61	0.279	0.107	1.00	0.67				
51	J205048.1+442428	312.70079	44.40804	0.61	0.726	0.289	0.67	0.17				30.73
52	J205048.5+441702	312.70228	44.28406	1.08	0.200	0.102	1.00	0.11				28.97
53	J205048.5+442104	312.70243	44.35134	0.47	0.281	0.115	0.60	0.00				29.47
54	J205048.6+442025	312.70252	44.34034	0.32	1.271	0.361	0.31	-0.31				29.91
55	J205048.7+442053	312.70304	44.34820	0.43	0.324	0.121	-0.06	-1.00				29.49
56	J205048.8+441923	312.70334	44.32325	0.22	3.915	0.378	0.26	-0.43				30.55
57	J205048.9+442829	312.70395	44.47478	1.44	0.243	0.142	1.00	0.43				
58	J205049.6+442441	312.70689	44.41161	0.40	0.470	0.165	1.00	0.65				31.25
59	J205049.7+442015	312.70727	44.33777	0.25	0.184	0.089	1.00	0.50				
60	J205050.2+442433	312.70943	44.40926	0.54	0.531	0.171	1.00	0.33				
61	J205050.2+442421	312.70957	44.40602	0.22	4.242	0.464	0.79	0.17				31.42
62	J205050.5+442507	312.71061	44.41864	0.58	0.457	0.155	1.00	-0.10				30.82
63	J205050.7+441725	312.71157	44.29053	0.61	0.142	0.113	NaN	1.00				
64	J205050.8+441852	312.71186	44.31447	0.65	0.295	0.118	1.00	0.56				
65	J205051.3+442518	312.71407	44.42190	0.43	0.984	0.172	1.00	0.30				30.90
66	J205051.7+442539	312.71577	44.42767	0.43	0.421	0.173	1.00	0.07				30.14
67	J205051.9+442441	312.71660	44.41155	0.40	0.457	0.162	1.00	0.47				31.29
68	J205052.4+442342	312.71839	44.39517	0.32	0.104	0.078	-1.00	NaN				
69	J205052.6+441645	312.71920	44.27919	0.76	2.193	0.268	0.18	-0.32				30.22
70	J205053.1+442353	312.72157	44.39825	0.54	0.167	0.084	0.00	-0.50				29.21
71	J205053.2+442450	312.72178	44.41394	0.43	0.314	0.120	NaN	1.00				
72	J205053.3+442414	312.72228	44.40415	0.72	0.174	0.083	NaN	1.00				
73	J205053.4+442435	312.72264	44.40995	0.54	0.527	0.173	0.33	0.20				30.19
74	J205053.4+442427	312.72279	44.40761	0.43	0.334	0.129	0.75	-0.17				29.89
75	J205053.5+442101	312.72327	44.35035	0.22	4.207	0.515	0.30	-0.30				30.42
76	J205053.6+442430	312.72357	44.40854	0.40	0.487	0.158	1.00	-0.24				30.16
77	J205053.7+442118	312.72381	44.35522	0.25	1.726	0.248	0.39	-0.68				
78	J205053.9+442118	312.72484	44.35522	0.25	0.696	0.229	0.04	-0.62				
79	J205054.8+441758	312.72859	44.29947	0.32	0.126	0.101	-1.00	NaN				29.45
80	J205054.8+442013	312.72861	44.33697	0.40	0.476	0.166	0.80	-0.12				29.43
81	J205054.8+442258	312.72874	44.38300	0.47	0.223	0.098	NaN	1.00				
82	J205055.4+441746	312.73107	44.29634	0.40	0.452	0.159	0.22	-0.57				
83	J205055.6+441750	312.73198	44.29732	0.47	3.098	0.289	0.18	-0.43				30.48
84	J205055.7+442144	312.73213	44.36239	0.25	0.670	0.309	0.60	0.00				29.61
85	J205055.7+441828	312.73229	44.30800	0.54	0.520	0.170	-0.05	-0.82				29.60
86	J205055.8+442420	312.73263	44.40570	0.54	0.151	0.075	1.00	0.67				

Table 3. continued.

X-ray no.	CXO Id (CXOU)	XMM Id (XMMU)	RA (J2000)	Dec (J2000)	Pos. err. (arcsec)	Count rate (cts/ksec)	Rate error (cts/ksec)	HR1 ACIS	HR2 ACIS	HR1 XMM	HR2 XMM	$\log L_X$ (erg/sec)
87	J205056.2+441926	312.73446	44.32396	0.25	2.807	0.293	-0.36	-0.85				30.00
88	J205056.6+441706	312.73619	44.28501	0.47	0.257	0.129	-0.14	-0.50				29.24
89	J205056.8+442527	312.73682	44.42440	0.68	0.245	0.107	NaN	1.00				
90	J205057.0+441643	312.73757	44.27863	0.79	0.162	0.089	-0.14	-0.50				29.02
91	J205057.3+442450	312.73901	44.41401	0.32	0.995	0.164	0.41	-0.09				30.33
92	J205057.4+442445	312.73951	44.41275	0.29	4.768	0.353	0.67	-0.15				
93	J205057.7+442138	312.74082	44.36083	0.58	0.144	0.079	0.33	0.20				29.09
94	J205057.9+442309	312.74162	44.38611	0.43	0.357	0.131	1.00	0.27				29.85
95	J205058.0+442959	312.74195	44.49976	1.48	2.542	0.313	0.15	-0.30				30.20
96	J205058.3+441432	312.74324	44.24237	1.12	1.924	0.304	0.25	-0.48				29.96
97	J205058.4+441444	312.74365	44.24582	1.08	1.990	0.278	0.11	-0.50				30.16
98	J205058.5+441221	312.74407	44.20597	2.02	0.360	0.224	-1.00	1.00				29.95
99	J205058.7+441731	312.74467	44.29202	0.36	7.317	0.473	0.61	-0.02				30.78
100	J205058.7+442317	312.74478	44.38828	0.29	0.517	0.177	0.00	-0.38				29.74
101	J205059.4+441728	312.74769	44.29138	0.61	0.141	0.086	-0.33	-1.00				28.70
102	J205059.4+441939	312.74788	44.32768	0.61	0.680	0.261	0.56	-0.75				29.87
103	J205059.6+443015	312.74834	44.50444	1.48	1.149	0.370	0.72	-0.56				30.09
104	J205100.2+442141	312.75097	44.36162	0.36	0.355	0.173	1.00	0.80				
105	J205100.3+442436	312.75127	44.41020	0.29	1.169	0.180	0.15	-0.68				29.88
106	J205101.4+441331	312.75594	44.22531	3.35	1.615	0.277	0.26	0.11				30.07
107	J205101.4+442504	312.75613	44.41782	0.54	0.561	0.182	1.00	0.29				29.50
108	J205101.4+441534	312.75615	44.25963	0.61	0.413	0.161	0.33	-0.60				30.47
109	J205101.5+441542	312.75654	44.26177	0.50	3.359	0.385	0.44	-0.22				29.61
110	J205102.1+442009	312.75905	44.33601	0.36	0.629	0.197	0.25	-0.67				28.74
111	J205102.3+442009	312.75993	44.33597	0.29	0.110	0.067	0.00	-0.33				28.93
112	J205102.5+442743	312.76053	44.46211	1.04	0.239	0.126	0.25	-1.00				
113	J205102.8+442822	312.76207	44.47302	0.97	0.318	0.166	1.00	0.33				
114	J205103.0+442403	312.76291	44.40087	0.22	4.505	0.361	0.84	0.09				30.53
115	J205103.3+442415	312.76388	44.40439	0.25	2.553	0.301	0.69	-0.14				30.41
116	J205103.3+441310	312.76412	44.21966	1.40	0.330	0.151	0.00	-0.14				29.07
117	J205103.8+442720	312.76623	44.45574	0.97	0.292	0.129	1.00	0.80				
118	J205104.4+442919	312.76867	44.48867	1.76	0.522	0.200	0.27	-0.27				29.51
119	J205104.5+442351	312.76884	44.39751	0.47	0.135	0.085	0.33	-0.14				29.28
120	J205104.6+442350	312.76936	44.39731	0.36	0.635	0.201	0.44	-0.24				29.95
121	J205105.3+441522	312.77246	44.25636	1.37	1.119	0.316	0.45	0.57				30.43
122	J205105.7+441358	312.77376	44.23287	3.17	0.689	0.232	0.39	-0.39				29.83
123	J205105.7+441632	312.77378	44.27577	0.61	1.694	0.274	0.40	-0.42				30.25
124	J205106.1+441758	312.77543	44.29946	0.68	0.830	0.157	-0.45	-0.64				29.47
125	J205106.6+442141	312.77768	44.36141	0.25	1.742	0.207	0.01	-0.71				29.89
126	J205107.0+442103	312.77932	44.35088	0.86	0.339	0.129	1.00	0.27				
127	J205108.5+442433	312.78563	44.40929	0.47	0.822	0.156	-0.08	-0.16				29.67
128	J205108.9+441642	312.78739	44.27847	0.61	1.284	0.210	0.29	0.00				29.91
129	J205109.0+442315	312.78762	44.38760	0.61	0.123	0.072	0.50	-1.00				29.03

Table 3. continued.

X-ray no.	CXO Id (CXOU)	XMM Id (XMMU)	RA (J2000)	Dec (J2000)	Pos. err. (arcsec)	Count rate (cts/ksec)	Rate error (cts/ksec)	HR1 ACIS	HR2 ACIS	HR1 XMM	HR2 XMM	$\log L_X$ (erg/sec)
130	J205109.3+442248	44.38018	0.76	0.174	0.087	0.00	0.00					28.79
131	J205110.6+442618	312.79433	44.43843	2.48	0.399	0.155	0.20	0.50				29.62
132	J205112.4+441943	312.80181	44.32878	0.47	0.238	0.104	0.50	-1.00				29.14
133	J205112.5+441809	312.80238	44.30272	1.12	0.493	0.163	0.07	-0.45				29.48
134	J205112.6+441845	312.80259	44.31273	0.36	7.343	0.455	0.13	-0.50				30.49
135	J205113.4+442448	312.80600	44.41335	0.50	0.285	0.133	1.00	0.60				29.66
136	J205113.7+442225	312.80733	44.37372	0.58	0.876	0.310	-0.71	0.00				
137	J205113.9+441814	312.80802	44.30402	0.58	0.187	0.125	1.00	0.67				
138	J205114.7+442746	312.81154	44.46285	1.26	0.420	0.174	0.71	0.08				29.71
139	J205114.9+442125	312.81233	44.35707	1.80	0.329	0.131	-0.33	0.56				29.32
140	J205115.1+441818	312.81313	44.30505	0.68	1.029	0.286	0.35	-0.62				29.88
141	J205115.7+442950	312.81548	44.49739	1.66	0.724	0.275	0.07	0.00				29.41
142	J205115.7+441457	312.81567	44.24929	1.69	1.635	0.409	0.60	-0.24				30.14
143	J205116.4+442258	312.81873	44.38292	0.40	1.559	0.220	0.20	-0.89				29.95
144	J205117.4+441914	312.82282	44.32071	0.86	0.376	0.143	0.08	-0.75				29.39
145	J205117.7+441829	312.82375	44.30826	0.58	0.162	0.094	1.00	-0.33				29.17
146	J205118.6+442454	312.82791	44.41510	0.61	0.146	0.117	NaN	1.00				29.50
147	J205119.4+441931	312.83097	44.32536	0.61	0.358	0.131	0.56	-0.40				29.57
148	J205120.4+442035	312.83529	44.34321	0.36	0.113	0.104	0.50	-1.00				
149	J205120.5+442032	312.83581	44.34245	0.32	3.245	0.326	0.28	-0.46				30.32
150	J205120.9+442619	312.83746	44.43887	0.65	3.421	0.334	0.40	-0.41				30.37
151	J205121.3+442405	312.83915	44.40162	0.47	3.327	0.314	0.16	-0.70				30.08
152	J205122.6+442108	312.84445	44.35224	0.50	2.623	0.285	0.44	-0.20				30.41
153	J205122.9+442326	312.84573	44.39078	0.83	0.188	0.104	NaN	1.00				
154	J205123.6+441542	312.84838	44.26186	0.83	0.606	0.221	0.33	-0.50				29.79
155	J205124.0+442024	312.85012	44.34014	0.72	0.228	0.109	1.00	0.25				29.49
156	J205124.1+441757	312.85050	44.29917	1.12	0.644	0.215	0.55	-0.48				29.92
157	J205124.7+441755	312.84573	44.29875	0.76	0.245	0.137	0.14	-1.00				29.25
158	J205124.7+441820	312.85303	44.30556	1.01	0.801	0.157	0.31	-0.48				
159	J205126.0+442439	312.85853	44.41105	1.01	0.844	0.258	1.00	0.62				
160	J205127.3+441958	312.86414	44.33286	0.83	0.186	0.126	-0.50	-1.00				
161	J205127.7+442541	312.86550	44.42833	1.30	0.443	0.176	1.00	0.38				29.90
162	J205128.5+442601	312.86878	44.43374	1.48	0.931	0.286	0.62	-0.26				30.24
163	J205128.5+441545	312.86906	44.26252	1.87	1.349	0.371	0.26	-0.22				30.01
164	J205128.9+441507	312.87066	44.25208	1.44	0.273	0.147	0.33	0.33				29.60
165	J205129.4+442437	312.87270	44.41046	1.66	0.471	0.166	0.71	0.33				29.33
166	J205129.4+442202	312.87288	44.36742	1.01	0.257	0.118	1.00	-0.33				29.74
167	J205131.5+442543	312.88156	44.42869	2.09	0.842	0.261	0.33	0.70				29.96
168	J205133.2+442423	312.88853	44.40662	1.44	0.275	0.127	1.00	0.27				29.61
169	J205133.4+442637	312.88925	44.44376	1.58	1.893	0.292	0.21	-0.13				30.26
170	J205137.6+442005	312.90673	44.33487	0.83	0.586	0.219	0.12	-0.64				29.62
171	J205138.2+441707	312.90936	44.28548	1.48	0.278	0.160	0.33	0.20				
172	J205139.2+442429	312.91318	44.40810	1.98	2.038	0.597	0.44	-0.44				30.15

Table 3. continued.

X-ray no.	CXO Id (CXOU)	XMM Id (XMMU)	RA (J2000)	Dec (J2000)	Pos. err. (arcsec)	Count rate (cts/ksec)	Rate error (cts/ksec)	HR1 ACIS	HR2 ACIS	HR1 XMM	HR2 XMM	$\log L_X$ (erg/sec)
173	J205141.8+441607	312.92445	44.26875	1.98	1.191	0.349	0.58	-0.19				29.90
174	J205145.4+441606	312.93934	44.26861	2.12	0.360	0.265	0.00	0.67				29.46
175	J205145.9+441917	312.94137	44.32144	3.20	0.773	0.266	0.33	0.56				30.68
176	J205547.0+434216	313.94598	43.70464	2.48	0.584	0.226	0.16	-0.38				29.32
177	J205558.5+434557	313.99378	43.76610	2.56	0.654	0.246	0.60	0.62				
178	J205559.5+434532	313.99818	43.75911	1.51	2.390	0.312	-0.33	-0.50				29.93
179	J205559.9+434030	313.99968	43.67509	3.20	0.738	0.251	0.33	0.53				30.44
180	J205603.8+434033	314.01593	43.67594	1.15	6.858	0.530	-0.07	-0.56				30.39
181	J205603.8+434448	314.01591	43.74679	1.84	1.151	0.229	0.73	0.58				
182	J205606.0+434628	314.02520	43.77449	1.76	0.476	0.187	0.50	-0.20				29.78
183	J205612.6+434531	314.05253	43.75880	1.30	1.209	0.207	0.71	-0.07				30.31
184	J205613.0+434109	314.05434	43.68609	1.22	0.417	0.164	0.00	0.76				
185	J205613.5+434120	314.05633	43.68894	1.44	0.294	0.150	0.00	0.64				
186	J205614.6+434528	314.06089	43.75794	0.97	0.246	0.112	-0.56	-1.00				29.44
187	J205616.5+434630	314.06881	43.77508	1.12	0.193	0.120	-1.00	1.00				
188	J205616.7+434142	314.06982	43.69525	1.12	0.216	0.121	1.00	0.11				29.71
189	J205618.0+434812	314.07533	43.80334	0.90	2.649	0.510	0.75	-0.40				
190	J205618.8+433908	314.07842	43.65234	1.30	4.114	0.406	1.00	0.36				31.19
191	J205619.1+434743	314.07963	43.79537	1.40	0.254	0.115	-1.00	1.00				
192	J205619.5+434539	314.08163	43.76084	0.65	1.007	0.278	0.39	-0.64				30.23
193	J205622.1+434031	314.09218	43.67536	0.94	0.281	0.131	1.00	0.80				
194	J205622.3+435007	314.09296	43.83540	1.44	0.263	0.134	1.00	-0.27				
195	J205622.7+434328	314.09496	43.72463	0.58	1.244	0.179	0.92	0.13				30.71
196	J205624.4+434757	314.10192	43.79925	0.86	0.154	0.129	-0.33	0.00				
197	J205626.2+434051	314.10938	43.68107	0.65	0.304	0.130	1.00	0.82				
198	J205626.2+434330	314.10956	43.72526	0.61	0.142	0.101	-0.33	0.00				28.73
199	J205626.3+434325	314.10986	43.72366	0.61	0.151	0.108	-1.00	1.00				
200	J205627.2+434558	314.11337	43.76626	0.47	0.971	0.155	0.55	-0.60				30.31
201	J205627.7+434536	314.11544	43.76002	0.54	0.482	0.158	0.50	-0.12				30.18
202	J205628.4+433859	314.11859	43.64986	2.59	0.732	0.286	0.60	0.62				
203	J205629.4+434705	314.12290	43.78483	0.58	0.149	0.086	1.00	0.33				
204	J205629.9+434253	314.12491	43.71485	0.86	0.405	0.151	1.00	0.22				30.45
205	J205629.9+435106	314.12492	43.85184	1.44	2.640	0.312	0.49	-0.18				30.47
206	J205631.0+434921	314.12930	43.82257	0.83	0.173	0.05	1.00	0.71				
207	J205631.4+434447	314.13117	43.74647	0.32	0.861	0.159	1.00	-0.22				30.53
208	J205632.5+434808	314.13570	43.80225	0.58	0.170	0.121	-1.00	1.00				29.21
209	J205633.9+434755	314.14139	43.79867	1.01	0.214	0.104	-0.20	0.33				29.28
210	J205635.4+434240	314.14763	43.71138	0.40	0.138	0.076	-1.00	1.00				
211	J205635.7+435313	314.14906	43.88721	1.80	0.478	0.221	0.00	0.83				30.49
212	J205636.0+434821	314.15003	43.80610	0.58	0.146	0.099	0.00	0.33				
213	J205636.2+435005	314.15104	43.83473	1.22	0.448	0.167	0.00	0.09				29.79
214	J205636.9+434822	314.15377	43.80617	0.47	0.778	0.147	1.00	0.14				
215	J205638.0+435133	314.15874	43.85937	0.94	3.558	0.344	0.77	0.45				

Table 3. continued.

X-ray no.	CXO Id (CXOU)	XMM Id (XMMU)	RA (J2000)	Dec (J2000)	Pos. err. (arcsec)	Count rate (cts/ksec)	Rate error (cts/ksec)	HR1 ACIS	HR2 ACIS	HR1 XMM	HR2 XMM	$\log L_X$ (erg/sec)
216	J205638.5+434843	314.16069	43.81218	0.76	0.169	0.086	-0.50	0.00	0.00	0.00	0.00	28.78
217	J205639.1+434723	314.16328	43.78998	0.36	0.117	0.091	1.00	0.67	0.00	0.67	0.00	29.76
218	J205639.6+434840	314.16505	43.81115	0.76	0.187	0.095	0.00	0.67	0.00	0.00	0.00	29.67
219	J205640.5+433826	314.16902	43.64067	1.51	0.686	0.216	0.00	0.85	0.00	0.00	0.00	29.76
220	J205641.7+434718	314.17410	43.78850	0.47	0.273	0.113	0.25	0.00	0.00	0.00	0.00	29.76
221	J205642.2+435426	314.17585	43.90738	2.95	1.142	0.354	0.33	0.16	0.33	0.16	0.16	30.12
222	J205643.0+434935	314.17940	43.82645	0.72	0.251	0.136	1.00	0.50	0.00	0.50	0.00	29.76
223	J205643.7+434845	314.18219	43.81250	0.72	0.232	0.108	NaN	1.00	0.00	0.00	0.00	29.76
224	J205643.9+434607	314.18301	43.76863	0.40	0.152	0.088	1.00	0.60	0.00	0.60	0.00	29.77
225	J205643.9+434600	314.18332	43.76680	0.22	1.182	0.177	-0.19	-0.78	0.00	0.00	0.00	30.39
226	J205644.0+434945	314.18344	43.82937	0.72	0.776	0.238	0.70	-0.48	0.00	0.00	0.00	29.80
227	J205645.7+434147	314.19048	43.69665	0.58	0.131	0.073	1.00	0.67	0.00	0.67	0.00	29.80
228	J205645.7+434240	314.19077	43.71115	0.32	0.125	0.105	-1.00	NaN	0.00	0.00	0.00	29.80
229	J205646.4+434518	314.19368	43.75513	0.36	0.625	0.192	-1.00	1.00	0.00	0.00	0.00	30.44
230	J205646.6+434602	314.19443	43.76734	0.22	4.626	0.337	0.18	-0.61	0.00	0.00	0.00	30.39
231	J205646.7+434609	314.19475	43.76927	0.18	2.620	0.262	0.10	-0.58	0.00	0.00	0.00	29.80
232	J205647.0+434929	314.19607	43.82484	0.47	0.385	0.185	0.50	-0.50	0.00	0.00	0.00	29.80
233	J205647.0+435022	314.19614	43.83952	0.94	0.295	0.126	0.50	0.45	0.00	0.00	0.00	29.80
234	J205647.4+435143	314.19758	43.86207	1.30	0.356	0.151	1.00	0.38	0.00	0.00	0.00	29.80
235	J205647.8+434847	314.19944	43.81309	0.61	0.146	0.118	1.00	0.33	0.00	0.00	0.00	29.80
236	J205648.2+435355	314.20085	43.89882	2.02	0.433	0.230	-1.00	1.00	0.00	0.00	0.00	29.80
237	J205648.5+434852	314.20236	43.81455	0.61	0.136	0.107	-1.00	1.00	0.00	0.00	0.00	29.80
238	J205648.7+434707	314.20306	43.78530	0.32	0.140	0.120	-1.00	NaN	0.00	0.00	0.00	29.80
239	J205648.8+434640	314.20358	43.77778	0.22	4.689	0.366	0.72	-0.28	0.00	0.00	0.00	29.80
240	J205648.9+434722	314.20413	43.78949	0.43	0.323	0.123	-1.00	1.00	0.00	0.00	0.00	29.80
241	J205649.4+434528	314.20588	43.75804	0.97	0.263	0.113	0.00	0.75	0.00	0.00	0.00	29.80
242	J205649.6+434933	314.20702	43.82607	0.76	0.720	0.224	0.78	0.33	0.00	0.00	0.00	29.80
243	J205650.4+434610	314.21031	43.76954	0.32	0.129	0.102	-0.33	-1.00	0.00	0.00	0.00	29.80
244	J205651.1+434705	314.21309	43.78474	0.32	0.236	0.104	NaN	1.00	0.00	0.00	0.00	29.80
245	J205651.3+434655	314.21396	43.78212	0.32	0.111	0.085	-1.00	1.00	0.00	0.00	0.00	29.80
246	J205651.3+434632	314.21405	43.77558	0.40	0.487	0.170	0.67	0.41	0.00	0.00	0.00	29.80
247	J205651.5+434224	314.21470	43.70689	0.47	0.646	0.124	-1.00	1.00	0.00	0.00	0.00	29.80
248	J205651.6+434252	314.21537	43.71459	0.29	1.248	0.181	-0.28	-0.89	0.00	0.00	0.00	29.80
249	J205651.9+433333	314.21659	43.55931	3.28	2.226	0.361	0.43	0.62	0.00	0.00	0.00	29.80
250	J205652.0+434240	314.21676	43.71119	0.29	0.124	0.079	-1.00	1.00	0.00	0.00	0.00	29.80
251	J205652.0+434434	314.21682	43.74285	0.32	0.152	0.125	0.00	-1.00	0.00	0.00	0.00	29.80
252	J205652.5+434955	314.21887	43.83201	1.76	0.345	0.133	0.56	-0.08	0.00	0.00	0.00	29.80
253	J205652.5+434646	314.21911	43.77964	0.40	0.157	0.086	0.20	-0.20	0.00	0.00	0.00	29.80
254	J205652.9+434643	314.22043	43.77865	1.04	0.208	0.099	0.50	0.33	0.00	0.00	0.00	29.80
255	J205653.7+434804	314.222407	43.80115	0.29	0.159	0.104	NaN	1.00	0.00	0.00	0.00	29.80
256	J205653.7+433749	314.222411	43.63041	0.97	3.493	0.351	0.89	0.48	0.00	0.00	0.00	29.80
257	J205654.2+434356	314.222595	43.73249	0.32	0.124	0.106	1.00	0.00	0.00	0.00	0.00	29.80
258	J205654.8+434605	314.222857	43.76831	0.29	0.124	0.079	-1.00	1.00	0.00	0.00	0.00	29.80

Table 3. continued.

X-ray no.	CXO Id (CXOU)	XMM Id (XMMU)	RA (J2000)	Dec (J2000)	Pos. err. (arcsec)	Count rate (cts/ksec)	Rate error (cts/ksec)	HR1 ACIS	HR2 ACIS	HR1 XMM	HR2 XMM	$\log L_X$ (erg/sec)
259	J205654.9+434856	314.22908	43.81558	0.65	0.345	0.140	0.78	-0.45				30.40
260	J205655.1+435135	314.22995	43.85988	1.48	0.860	0.271	0.60	0.47				
261	J205655.3+434028	314.23072	43.67451	0.68	0.291	0.124	NaN	1.00				
262	J205656.1+434748	314.23406	43.79688	0.32	0.926	0.185	1.00	0.44				
263	J205656.2+434637	314.23436	43.77705	0.32	0.829	0.236	1.00	0.86				
264	J205656.4+434313	314.23517	43.72048	0.47	0.488	0.208	1.00	0.43				
265	J205656.5+434248	314.23556	43.71359	0.25	6.008	0.840	1.00	0.99				
266	J205656.6+434910	314.23585	43.81948	0.47	0.814	0.162	0.66	-0.41				
267	J205657.0+434812	314.23756	43.80359	0.47	0.927	0.260	0.33	0.75				
268	J205657.6+434339	314.24029	43.72761	0.32	0.103	0.077	1.00	-1.00				
269	J205658.2+434917	314.24271	43.82148	0.47	2.781	0.284	0.73	0.22				30.96
270	J205658.2+433955	314.24273	43.66541	0.86	0.337	0.126	-1.00	1.00				
271	J205658.8+434016	314.24514	43.67128	0.79	0.487	0.166	-0.33	-0.43				
272	J205659.0+435023	314.24620	43.83978	0.79	0.207	0.158	-1.00	1.00				
273	J205659.3+434753	314.24717	43.79816	0.43	0.341	0.135	-0.27	-0.33				29.23
274	J205659.5+434637	314.24816	43.77698	0.29	2.397	0.412	0.93	0.02				31.33
275	J205700.3+435028	314.25145	43.84112	0.83	0.541	0.196	1.00	0.45				
276	J205700.3+434207	314.25166	43.70216	0.43	0.376	0.148	0.71	0.08				
277	J205701.2+433822	314.25529	43.63971	1.44	0.255	0.121	-0.60	0.71				
278	J205701.5+434325	314.25664	43.72380	0.18	7.161	0.570	0.92	0.42				
279	J205701.6+434139	314.25669	43.69430	0.40	0.138	0.078	-0.20	-1.00				28.93
280	J205701.7+434738	314.25736	43.79400	0.54	0.875	0.279	1.00	0.71				
281	J205702.2+434826	314.25932	43.80747	0.58	1.372	0.204	0.83	0.32				
282	J205703.3+434144	314.26380	43.69578	0.40	0.576	0.196	0.75	0.22				30.08
283	J205703.5+434500	314.26487	43.75001	0.25	0.712	0.213	0.64	0.28				30.78
284	J205704.3+434840	314.26823	43.81124	0.72	0.671	0.208	1.00	0.31				
285	J205704.4+434853	314.26862	43.81476	0.90	0.974	0.175	0.88	0.30				31.09
286	J205704.7+434411	314.26997	43.73646	0.50	0.178	0.085	1.00	0.71				
287	J205704.9+434700	314.27070	43.78346	0.54	0.199	0.097	1.00	0.50				
288	J205705.5+434045	314.27303	43.67919	0.54	6.294	0.436	1.00	0.89				
289	J205705.8+434910	314.27436	43.81960	1.15	1.355	0.220	0.80	-0.25				30.66
290	J205706.3+434229	314.27643	43.70823	1.01	0.186	0.087	0.60	-0.33				30.83
291	J205706.9+434924	314.27894	43.82351	1.73	0.434	0.165	1.00	-0.06				30.07
292	J205707.0+434752	314.27948	43.79799	1.01	0.234	0.107	NaN	1.00				
293	J205707.2+435007	J205707.1+435004	314.28036	43.83544	0.90	3.731	0.357	-0.35	-0.66	-0.70	0.02	30.13
294	J205707.4+434242	314.28120	43.71176	0.86	0.373	0.137	0.71	0.37				30.49
295	J205707.5+434159	314.28149	43.69997	0.65	0.932	0.254	-0.35	-0.50				29.95
296	J205708.4+434819	J205708.4+434816	314.28526	43.80548	0.61	4.190	0.359	0.96	0.53	0.22	0.29	
297	J205710.9+434251	314.29559	43.71436	0.58	0.139	0.087	-1.00	1.00				
298	J205710.9+433805	314.29557	43.63482	1.40	0.284	0.151	-0.20	0.33				30.28
299	J205711.6+434804	314.29860	43.80123	0.94	0.849	0.166	1.00	0.43				31.53
300	J205712.1+434615	314.30061	43.77090	0.61	0.154	0.131	-1.00	NaN				
301	J205712.8+434912	J205712.6+434909	314.30334	43.82012	1.01	0.822	0.244	1.00	0.10	0.17	0.20	30.78

Table 3. continued.

X-ray no.	CXO Id (CXOU)	XMM Id (XMMU)	RA (J2000)	Dec (J2000)	Pos. err. (arcsec)	Count rate (cts/ksec)	Rate error (cts/ksec)	HR1 ACIS	HR2 ACIS	HR1 XMM	HR2 XMM	$\log L_X$ (erg/sec)
302	J205713.0+434718	314.30441	43.778859	2.20	0.645	0.213	0.08	0.52				
303	J205713.8+433947	314.30756	43.66324	1.22	0.480	0.181	1.00	0.05				30.52
304	J205713.9+434808	314.30824	43.80249	0.94	0.291	0.123	0.56	-0.27				30.16
305	J205714.8+434537	314.31199	43.76041	0.86	0.377	0.142	0.83	-0.29				30.10
306	J205715.7+434722	J205715.5+434719	314.31549	43.78968	1.08	1.768	0.245	-0.33	0.97	-0.12	0.60	
307	J205716.3+434200	314.31829	43.70016	0.86	0.177	0.151	NaN	1.00				
308	J205717.5+434829	314.32323	43.80816	0.86	0.447	0.180	0.82	-0.18				
309	J205718.5+434719	J205718.3+434714	314.32711	43.78870	0.86	1.321	0.215	0.80	0.00	0.38	0.11	31.19
310	J205718.6+434726	J205718.3+434714	314.32755	43.79057	1.15	0.573	0.200	0.75	-0.27	0.38	0.11	30.45
311	J205719.0+434854	314.32957	43.81512	1.73	0.466	0.173	0.45	-0.07				30.52
312	J205719.1+434931	J205719.1+434930	314.32985	43.82546	2.05	0.880	0.269	0.33	-0.29	0.27	0.07	30.26
313	J205721.4+434400	314.33941	43.73359	1.08	0.196	0.100	1.00	0.71				
314	J205724.2+434103	314.35114	43.68431	1.94	0.981	0.280	0.88	0.23				30.97
315	J205725.1+434209	314.35482	43.70264	1.37	2.896	0.325	0.84	0.25				31.34
316	J205726.1+434235	314.35913	43.70999	1.04	0.211	0.105	1.00	0.78				
317	J205727.6+435622	J205727.6+435622	314.36516	43.94040	3.17	3.097	0.462	-0.44	-0.26	-0.58	0.16	30.05
318	J205731.6+435956	314.38198	43.99893	1.98	0.646	0.326	0.00	0.00				30.16
319	J205742.5+435449	J205742.3+435447	314.42724	43.91371	1.19	3.195	0.444	0.88	0.57	0.27	0.38	
320	J205743.9+435857	314.43299	43.98268	2.34	2.968	0.480	0.64	0.76				30.88
321	J205744.1+435355	J205744.0+435352	314.43402	43.89869	1.58	3.266	0.455	1.00	0.76	0.39	0.49	
322	J205751.1+435232	J205750.7+435231	314.46299	43.87558	0.61	0.226	0.181	NaN	1.00	-0.10	0.49	
323	J205751.9+435252	314.46647	43.88124	0.83	0.228	0.126	1.00	0.50				
324	J205754.1+435326	314.47549	43.89061	0.36	0.170	0.171	NaN	1.00				
325	J205756.4+435235	J205756.4+435233	314.48539	43.87663	0.50	3.651	0.459	-0.06	-0.55	-0.48	0.17	30.12
326	J205757.7+435837	314.49065	43.97709	1.98	0.617	0.277	1.00	0.50				29.82
327	J205759.8+435326	J205759.7+435324	314.49924	43.89058	0.61	1.987	0.335	0.50	-0.11	-0.10	0.04	30.29
328	J205801.6+435848	314.50685	43.98005	1.76	2.455	0.463	0.49	-0.30				30.46
329	J205801.6+435349	314.50703	43.89699	0.32	0.186	0.176	1.00	-0.33				
330	J205801.8+435349	314.50784	43.89700	0.40	0.855	0.284	1.00	0.04				30.75
331	J205809.3+435632	314.53899	43.94236	0.32	0.212	0.162	-1.00	NaN				
332	J205806.1+435300	J205805.9+435259	314.52547	43.88360	0.25	2.756	0.331	-0.09	-0.57	-0.14	-0.17	30.23
333	J205810.8+435308	J205810.6+435306	314.54506	43.88563	0.25	1.083	0.214	-0.31	-0.33	-0.22	-0.22	30.01
334	J205814.2+435304	314.55944	43.88458	0.40	0.252	0.133	0.00	-1.00				29.24
335	J205816.2+435334	314.56767	43.89304	0.36	0.336	0.159	0.71	-0.33				
336	J205816.3+435320	J205816.4+435322	314.56819	43.88908	0.22	0.556	0.237	1.00	-0.09	0.23	0.11	
337	J205816.7+435335	314.56987	43.89320	0.43	0.523	0.197	0.50	-0.20				30.92
338	J205817.0+435343	314.57091	43.89534	0.22	0.547	0.217	1.00	0.87				29.80
339	J205817.0+435315	J205816.4+435322	314.57117	43.88776	0.14	2.311	0.317	0.86	-0.49	0.23	0.11	
340	J205817.1+435336	314.57127	43.89335	0.40	0.276	0.154	0.14	-0.60				29.29
341	J205817.9+435344	J205818.6+435345	314.57461	43.89557	0.22	1.274	0.230	0.63	-0.10	0.07	0.05	30.39
342	J205818.3+435323	314.57656	43.88983	0.22	1.309	0.235	1.00	0.22				
343	J205818.8+435354	J205818.6+435345	314.57837	43.89846	0.29	0.271	0.151	0.67	-0.67	0.07	0.05	29.44
344	J205819.0+435244	314.57957	43.87894	0.22	0.502	0.211	1.00	0.85				

Table 3. continued.

X-ray no.	CXO Id (CXOU)	XMM Id (XMMU)	RA (J2000)	Dec (J2000)	Pos. err. (arcsec)	Count rate (cts/ksec)	Rate error (cts/ksec)	HR1 ACIS	HR2 ACIS	HR1 XMM	HR2 XMM	$\log L_X$ (erg/sec)
345	J205819.5+435344	J205818.6+435345	314.58127	43.89571	0.22	0.738	0.293	0.17	-0.27	0.07	0.05	29.42
346	J205819.5+435354		314.58144	43.89846	0.29	0.206	0.129	0.00	-1.00			29.03
347	J205819.5+435400		314.58157	43.90006	0.29	0.179	0.113	0.00	0.33			30.02
348	J205821.5+435344		314.58977	43.89578	0.29	0.702	0.237	1.00	0.29			29.71
349	J205821.7+435330		314.59042	43.89184	0.25	0.260	0.149	0.20	-0.50			30.63
350	J205823.2+435258	J205823.2+435301	314.59701	43.88300	0.14	5.072	0.450	0.11	-0.66	-0.13	-0.19	29.71
351	J205823.3+435253	J205823.2+435301	314.59714	43.88165	0.50	0.305	0.144	1.00	0.33	-0.13	-0.19	30.22
352	J205823.3+434915	J205823.0+434913	314.59733	43.82093	1.08	0.250	0.125	-0.50	0.50	0.39	0.36	30.22
353	J205823.6+435255	J205823.2+435301	314.59848	43.88207	0.22	1.429	0.251	-0.22	-0.80	-0.13	-0.19	
354	J205823.7+435256	J205823.2+435301	314.59909	43.88243	0.36	0.309	0.149	0.11	-0.43	-0.13	-0.19	
355	J205823.7+435311		314.59915	43.88649	0.18	4.116	0.413	0.16	-0.48			30.63
356	J205823.8+435447		314.59922	43.91316	0.32	0.169	0.127	-1.00	1.00			
357	J205823.9+435354	J205823.8+435353	314.59999	43.89848	0.14	9.721	0.617	0.37	-0.41	-0.27	-0.04	30.98
358	J205824.9+434851		314.60400	43.81417	0.79	0.211	0.127	0.00	0.50			
359	J205825.4+434834		314.60611	43.80951	0.83	0.220	0.153	1.00	0.50			
360	J205825.5+435328	J205825.4+435327	314.60640	43.89129	0.25	2.329	0.303	0.33	-0.41	-0.01	-0.15	30.50
361	J205825.7+435216		314.60720	43.87114	0.32	0.158	0.134	1.00	0.33			
362	J205827.0+435320		314.61257	43.88890	0.18	3.689	0.398	0.55	-0.39			30.53
363	J205827.0+435110		314.61289	43.85291	0.40	0.245	0.144	1.00	0.75			
364	J205828.6+434855		314.61939	43.81533	1.19	0.564	0.202	0.75	0.12			30.65
365	J205830.3+435359		314.62663	43.89978	0.25	0.328	0.150	0.33	-0.71			29.59
366	J205830.5+435408		314.62716	43.90249	0.32	0.159	0.124	0.50	-1.00			29.11
367	J205832.3+435617		314.63481	43.93828	1.33	0.335	0.151	-0.50	0.71			29.83
368	J205840.6+435303		314.66925	43.88426	0.54	0.240	0.140	-0.33	0.50			29.80
369	J205842.2+434926		314.67598	43.82397	2.41	0.554	0.206	0.00	-0.29			29.30
370	J205842.9+435451		314.67885	43.91431	0.90	0.494	0.200	0.60	0.60			
371	J205844.5+435358		314.68556	43.89960	0.68	0.437	0.218	1.00	0.00			
372	J205846.9+435151	J205846.6+435153	314.69554	43.86436	1.04	2.896	0.370	1.00	0.63	-0.18	0.34	31.24
373	J205847.7+435141	J205847.5+435141	314.69898	43.86147	1.15	2.104	0.323	-0.53	-0.62	-0.41	0.21	29.88
374	J205848.9+435316	J205848.7+435315	314.70416	43.88791	0.83	0.619	0.222	-0.29	-0.20	-0.04	0.15	29.75
375	J205849.1+435035		314.70477	43.84325	2.16	0.961	0.309	0.56	0.24			
376	J205849.8+435204		314.70783	43.86799	1.40	1.140	0.332	0.24	0.04			
377	J205852.6+435451	J205852.3+435448	314.71944	43.91439	2.81	1.315	0.387	-0.52	0.26	-0.60	0.24	
378	J205853.3+435400	J205853.2+435358	314.72223	43.90019	1.55	2.502	0.356	0.62	0.00	0.21	-0.05	30.43
379		J205855.4+440336	314.73100	44.06010	1.22	230.150	5.214		-0.79	-0.69		31.29
380		J205835.7+440512	314.64882	44.08682	3.67	5.312	1.024			-0.08	0.23	29.91
381		J205932.7+440550	314.88627	44.09747	5.44	10.522	2.225			0.17	0.04	30.83
382		J205900.8+440710	314.75364	44.11951	1.80	117.830	5.745			0.51	0.23	31.14
383		J205901.4+440740	314.75620	44.12795	2.63	5.762	1.128			-0.35	-0.14	29.69
384		J205943.3+440748	314.93043	44.13002	3.78	6.522	1.333			-0.58	0.32	29.74
385		J205813.7+440800	314.55729	44.13334	2.66	3.907	0.807			0.19	0.30	30.08
386		J205932.7+440834	314.88643	44.14278	1.55	2.617	0.697			0.39	-0.59	29.85
387		J205804.3+440918	314.51806	44.15508	4.14	12.950	1.648			-0.09	-0.27	

Table 3. continued.

X-ray no.	CXO Id (CXOU)	XMM Id (XMMU)	RA (J2000)	Dec (J2000)	Pos. err. (arcsec)	Count rate (cts/ksec)	Rate error (cts/ksec)	HR1 ACIS	HR2 ACIS	HR1 XMM	HR2 XMM	$\log L_X$ (erg/sec)
388	J205914.8+440930	314.81201	44.15860	3.10	7.197	1.018	-0.86	0.61	29.79			
389	J205932.9+440946	314.88725	44.16283	2.81	13.153	1.546	0.04	-0.11	30.72			
390	J205812.9+440951	314.55383	44.16419	4.10	3.469	0.822	-0.58	0.12	29.49			
391	J205743.1+441037	314.42987	44.17698	4.82	8.945	2.838	-0.30	0.07	29.88			
392	J205917.3+441040	314.82216	44.17793	5.22	5.078	0.996	0.13	0.30	30.16			
393	J205819.0+441058	314.57950	44.18298	3.24	6.054	0.931	-0.61	0.13	29.71			
394	J205902.3+441112	314.75997	44.18671	3.31	4.441	0.708	0.04	0.45	30.15			
395	J205935.4+441120	314.89775	44.18895	5.26	6.058	1.193	-0.51	0.39	29.72			
396	J205910.6+441142	314.79437	44.19507	2.45	12.933	1.149	-0.57	-0.21	30.04			
397	J205740.9+441155	314.42053	44.19880	3.89	6.729	2.679	-0.44	-0.40	29.76			
398	J205906.8+441231	314.77851	44.20870	4.14	2.268	0.551	-0.05	0.46	29.64			
399	J205954.7+441246	314.97817	44.21282	4.86	9.075	1.558	-0.18	0.62	30.35			
400	J205806.0+441250	314.52511	44.21398	3.46	19.769	1.774	-0.52	0.01				
401	J205916.6+441311	314.81958	44.21976	3.46	4.342	0.747	0.06	-0.06				
402	J205913.1+441318	314.80484	44.22186	3.20	6.304	0.946	-0.17	-0.22	30.05			
403	J205925.2+441345	314.85520	44.22926	4.00	3.031	0.685	0.31	0.06	29.59			
404	J205737.7+441350	314.40734	44.23077	5.15	22.230	4.260	-0.50	-0.32	30.57			
405	J205925.7+441420	314.85722	44.23893	2.48	3.832	0.686	-0.17	0.05	30.03			
406	J205931.0+441508	314.87944	44.25225	3.64	14.698	1.439	-0.30	0.10	30.10			
407	J205819.9+441547	314.58306	44.26331	3.10	6.423	0.905	-0.02	0.38				
408	J205839.6+441614	314.66537	44.27076	1.98	24.220	1.424	-0.10	-0.32				
409	J205912.7+441626	314.80319	44.27389	2.23	17.035	1.275	0.16	-0.27				
410	J210002.9+441637	315.01210	44.27722	4.28	16.592	2.216	-0.01	-0.05	30.39			
411	J205816.7+441729	314.56969	44.29158	3.46	4.879	0.846	-0.24	-0.12	29.75			
412	J205803.6+441735	314.51517	44.29314	2.12	3.013	0.763	0.09	-0.46				
413	J205900.4+441757	314.75184	44.29941	2.59	9.906	0.995	-0.66	-0.08	29.93			
414	J205906.6+441822	314.77783	44.30616	2.99	6.607	0.858	-0.38	0.05	30.13			
415	J205827.2+441830	314.61334	44.30856	2.81	2.730	0.610	0.28	0.01				
416	J205842.6+441857	314.67783	44.31584	2.20	19.181	1.417	-0.52	-0.38	30.23			
417	J205840.4+441936	314.66847	44.32689	2.02	7.520	0.910	-0.16	-0.43				
418	J205903.4+441957	314.76454	44.33256	2.59	3.468	0.671	-0.28	-0.28	29.77			
419	J205900.6+442041	314.75273	44.34475	3.67	4.163	0.809	-0.54	0.18				
420	J205903.5+442046	314.76474	44.34636	3.60	4.496	0.836	-0.63	0.05	29.58			
421	J205814.7+442051	314.56157	44.34753	1.91	4.137	0.854	0.56	0.31	29.72			
422	J205812.0+442054	314.55021	44.34845	4.07	4.059	0.955	-0.11	0.01	29.97			
423	J205944.8+442114	314.93675	44.35406	3.56	13.980	2.564	-0.57	-0.14				
424	J205806.2+442146	314.52595	44.36283	3.24	9.435	1.451	0.23	0.30	29.94			
425	J205755.9+442321	314.48327	44.38921	4.39	17.624	2.496	-0.36	0.07	30.18			
426	J205841.5+442325	314.67307	44.39043	2.23	4.042	1.132	0.75	0.11	29.78			
427	J205916.1+442621	314.81709	44.43921	3.10	4.005	1.074	-0.03	0.24	29.53			
428	J205905.9+442654	314.77467	44.44859	2.95	15.519	2.015	0.29	-0.20	30.43			
429	J205946.5+442716	314.94380	44.45460	5.40	13.484	2.828	-0.64	0.42	30.06			
430	J205839.5+434307	314.66468	43.71865	5.22	7.131	1.397	-0.21	0.16	29.86			

Table 3. continued.

X-ray no.	CXO Id (CXOU)	XMM Id (XMMU)	RA (J2000)	Dec (J2000)	Pos. err. (arcsec)	Count rate (cts/ksec)	Rate error (cts/ksec)	HR1 ACIS	HR2 ACIS	HR1 XMM	HR2 XMM	$\log L_X$ (erg/sec)
431	J205800.8+434515	314.50366	43.75429	4.36	3.879	1.019		0.05	0.16	0.16	0.16	30.13
432	J205834.5+434520	314.54384	43.75570	3.28	6.054	0.940		0.16	0.39			
433	J205809.8+434536	314.54124	43.76002	4.28	8.268	1.106	-0.02	0.15		0.15	30.34	
434	J205808.6+434658	314.53612	43.78294	1.98	25.479	1.486		0.58	-0.09		0.58	30.89
435	J205741.9+434721	314.42465	43.78932	3.10	6.580	0.935		-0.47	0.23		0.23	29.76
436	J205744.8+434839	314.43700	43.81098	2.38	13.879	1.161		-0.46	-0.01		0.01	30.07
437	J205854.5+434904	314.72710	43.81803	5.44	4.525	0.950		-0.05	0.45		0.45	30.43
438	J205754.4+434931	314.47701	43.82539	4.03	8.857	1.059		-0.49	0.34		0.34	29.88
439	J205805.8+434931	314.52437	43.82541	2.56	8.019	0.792		-0.37	0.06		0.06	30.11
440	J205849.6+435006	314.70695	43.83511	2.34	12.767	1.061		0.07	-0.12		0.12	30.39
441	J205757.3+435007	314.48891	43.83541	2.20	13.232	0.978		-0.63	0.12		0.12	30.10
442	J205748.5+435022	314.45214	43.83961	1.91	31.113	1.703		-0.68	-0.17		0.17	30.42
443	J205726.8+435037	314.36202	43.84370	6.80	8.424	1.418		-0.22	0.30		0.30	29.85
444	J205727.9+435144	314.36637	43.86239	2.05	2.152	0.507		-0.81	0.70		0.70	29.26
445	J205716.2+435156	314.31751	43.86577	4.25	11.163	1.479		0.07	0.15		0.15	30.98
446	J205709.9+435226	314.29161	43.87409	5.15	7.504	1.437		0.09	0.14		0.14	31.08
447	J205928.7+435459	314.86965	43.91659	3.24	16.822	2.573		-0.22	-0.20		0.20	30.34
448	J205746.7+435633	314.44498	43.94252	2.95	1.868	0.453		0.31	0.06		0.06	30.00
449	J205818.6+435652	314.57770	43.94798	3.38	3.017	0.503		-0.31	0.22		0.22	29.64
450	J205905.7+435701	314.77385	43.95038	1.37	112.750	3.186		-0.40	-0.42		0.42	31.14
451	J205722.1+435751	314.34209	43.96427	2.09	31.320	2.066		-0.50	-0.09		0.09	30.43
452	J205844.3+435810	314.68494	43.96965	3.49	4.085	0.717		-0.01	0.24		0.24	30.01
453	J205826.2+440015	314.60920	44.00434	5.47	3.826	0.811		-0.26	0.35		0.35	29.60
454	J205839.5+440133	314.66470	44.02605	4.97	6.969	1.251		-0.03	0.26		0.26	30.69
455	J205717.8+440227	314.32417	44.04099	4.36	8.421	2.217		-0.34	0.07		0.07	29.92
456	J205821.6+440305	314.59029	44.05149	5.36	5.109	1.052		-0.12	0.38		0.38	30.10
457	J205833.5+440333	314.63972	44.05929	2.63	17.160	1.760		-0.15	-0.04		-0.04	
458	J205748.6+440525	314.45256	44.09041	2.30	16.083	2.527		-0.16	-0.39		0.39	30.35
459	J205421.4+435043	313.58949	43.84545	2.02	190.240	5.560		0.54	-0.06		0.20	30.58
460	J205440.6+435243	313.66932	43.87867	3.06	2.748	0.716		-0.63	0.12		0.12	29.37
461	J205403.1+435455	313.51331	43.91536	5.18	5.067	0.986		-0.11	0.01		0.01	30.10
462	J205414.9+435457	313.56228	43.91601	7.09	5.775	1.056		-0.06	0.20		0.20	30.58
463	J205438.8+435528	313.66201	43.92462	2.88	8.813	1.080		-0.49	-0.19		0.19	29.87
464	J205530.2+435653	313.87620	43.94818	3.17	8.992	1.333		-0.74	-0.07		0.07	29.88
465	J205455.5+435653	313.73136	43.94833	2.66	10.627	1.130		-0.72	-0.14		0.14	29.96
466	J205516.9+435706	313.82065	43.95187	3.71	4.254	0.839		-0.57	0.32		0.32	29.56
467	J205348.1+435711	313.45078	43.95327	6.08	11.561	1.569		0.12	0.44		0.44	30.99
468	J205511.0+435713	313.79604	43.95381	1.76	4.376	0.787		-0.19	-0.55		0.55	29.79
469	J205458.3+435713	313.74328	43.95388	2.81	8.806	1.022		-0.71	-0.07		0.07	29.87
470	J205421.1+435802	313.58815	43.96728	2.84	2.014	0.465		-0.45	0.03		0.03	29.28
471	J205412.0+435806	313.55006	43.96836	4.79	4.672	0.783		0.05	0.31		0.31	29.95
472	J205353.3+435807	313.47230	43.96862	2.88	9.923	1.212		-0.60	-0.08		0.08	29.93
473	J205425.8+435820	313.60767	43.97248	2.05	19.842	1.270		-0.65	-0.39		0.39	30.23

Table 3. continued.

X-ray no.	CXO Id (CXOU)	XMM Id (XMMU)	RA (J2000)	Dec (J2000)	Pos. err. (arcsec)	Count rate (cts/ksec)	Rate error (cts/ksec)	HR1 ACIS	HR2 ACIS	HR1 XMM	HR2 XMM	$\log L_X$ (erg/sec)
474	J205401.3+435851	313.50548	43.998087	4.50	6.684	0.993	-0.33	-0.14	-0.33	-0.14	-0.33	29.75
475	J205538.6+435905	313.91103	43.98479	2.34	96.706	3.923	0.70	0.32	0.70	0.32	0.70	31.47
476	J205441.8+435939	313.67449	43.99420	1.91	6.224	0.669	0.62	0.47	0.62	0.47	0.62	30.80
477	J205413.4+435945	313.55616	43.99589	3.06	1.491	0.393	-0.20	0.55	-0.20	0.55	-0.20	29.55
478	J205526.1+435945	313.85916	43.99597	7.85	5.244	1.145	-0.23	0.06	-0.23	0.06	-0.23	29.80
479	J205503.1+440008	313.76318	44.00237	3.38	3.592	0.593	0.32	0.21	0.32	0.21	0.32	30.84
480	J205416.5+440037	313.56903	44.01044	3.71	2.762	0.540	0.31	-0.23	0.31	-0.23	0.31	29.82
481	J205541.2+440038	313.92179	44.01066	6.41	11.616	1.739	0.23	0.01	0.23	0.01	0.23	30.58
482	J205436.2+440039	313.65096	44.01095	3.67	2.186	0.423	-0.05	0.35	-0.05	0.35	-0.05	30.17
483	J205338.6+440041	313.41109	44.01145	5.29	5.559	1.120	0.01	0.28	0.01	0.28	0.01	29.83
484	J205406.8+440045	313.52874	44.01251	2.95	7.086	0.896	0.10	-0.29	0.10	-0.29	0.10	30.20
485	J205443.9+440045	313.68320	44.01276	2.23	13.007	0.977	-0.73	-0.20	-0.73	-0.20	-0.73	30.04
486	J205454.8+440052	313.72851	44.01471	2.84	1.635	0.376	0.09	0.57	0.09	0.57	0.09	30.03
487	J205502.7+440149	313.76141	44.03042	3.31	3.605	0.573	-0.46	-0.11	-0.46	-0.11	-0.46	29.49
488	J205458.6+440205	313.74448	44.03491	1.55	54.015	1.965	-0.72	-0.52	-0.72	-0.52	-0.72	30.66
489	J205526.8+440225	313.86207	44.04039	3.42	4.945	0.832	0.04	0.53	0.04	0.53	0.04	29.97
490	J205434.6+440241	313.64434	44.04494	2.99	1.422	0.357	-0.28	-0.28	-0.28	-0.28	-0.28	29.08
491	J205543.3+440310	313.93064	44.05292	3.28	8.065	1.272	0.12	-0.19	0.12	-0.19	0.12	29.84
492	J205338.9+440332	313.41217	44.05899	2.05	11.071	1.362	0.21	-0.11	0.21	-0.11	0.21	30.34
493	J205409.3+440336	313.53893	44.06005	2.09	1.885	0.468	0.47	0.33	0.47	0.33	0.47	29.82
494	J205334.4+440412	313.39337	44.07005	2.95	11.702	1.515	0.22	0.57	0.22	0.57	0.22	30.60
495	J205447.7+440419	313.69881	44.07221	3.49	3.041	0.533	0.33	-0.11	0.33	-0.11	0.33	30.24
496	J205518.2+440419	313.82599	44.07218	3.71	3.641	0.712	-0.40	-0.07	-0.40	-0.07	-0.40	29.50
497	J205404.3+440458	313.51795	44.08278	1.98	2.234	0.500	0.60	0.54	0.60	0.54	0.60	29.82
498	J205531.2+440606	313.88009	44.10170	4.00	3.936	0.891	0.52	0.22	0.52	0.22	0.52	29.86
499	J205327.2+440606	313.36357	44.10169	2.88	20.478	2.519	0.11	-0.28	0.11	-0.28	0.11	30.24
500	J205506.7+440745	313.77796	44.12936	2.20	1.840	0.489	-0.14	0.65	-0.14	0.65	-0.14	30.55
501	J205522.6+440800	313.84449	44.13361	2.38	5.768	0.952	0.77	0.47	0.77	0.47	0.77	30.32
502	J205520.2+440902	313.83458	44.15069	2.99	2.742	0.695	0.24	0.52	0.24	0.52	0.24	30.57
503	J205445.5+441015	313.68976	44.17107	2.95	8.285	1.049	-0.60	0.02	0.60	0.02	0.60	29.87
504	J205404.6+441022	313.51918	44.17301	2.81	15.851	1.862	0.23	-0.07	0.23	-0.07	0.23	30.63
505	J205346.6+441058	313.44418	44.18284	6.55	14.013	2.196	-0.04	0.33	-0.04	0.33	-0.04	31.01
506	J205355.6+441108	313.48178	44.18563	4.68	9.431	1.497	0.15	0.05	0.15	0.05	0.15	30.33
507	J205450.8+441134	313.71170	44.19285	4.18	10.664	1.378	0.18	-0.02	0.18	-0.02	0.18	30.55
508	J205346.6+441156	313.44432	44.19915	5.80	6.038	1.427	-0.22	0.31	-0.22	0.31	-0.22	30.17
509	J205446.6+441206	313.69451	44.20186	3.42	6.442	1.087	0.33	-0.05	0.33	-0.05	0.33	32.06
510	J205428.0+441330	313.61673	44.22518	6.52	11.652	1.810	-0.03	0.33	-0.03	0.33	-0.03	32.06
511	J205414.6+441424	313.56098	44.24000	3.78	6.214	1.274	-0.41	0.28	-0.41	0.28	-0.41	29.72
512	J205432.2+441438	313.63421	44.24392	4.93	9.077	1.601	-0.25	0.10	-0.25	0.10	-0.25	29.89
513	J205410.3+441457	313.54295	44.24934	4.10	5.759	1.376	-0.29	0.23	-0.29	0.23	-0.29	30.52
514	J205438.1+441526	313.65889	44.25738	3.10	3.859	1.023	-0.40	0.33	-0.40	0.33	-0.40	29.52
515	J205428.0+441614	313.61697	44.27057	1.40	4.685	1.063	-0.51	0.27	-0.51	0.27	-0.51	31.18
516	J205318.0+441208	313.32529	44.20238	8.50	38.845	9.815	-0.11	0.12	-0.11	0.12	-0.11	31.18

Table 3. continued.

X-ray no.	CXO Id (CXOU)	XMM Id (XMMU)	RA (J2000)	Dec (J2000)	Pos. err. (arcsec)	Count rate (cts/ksec)	Rate error (cts/ksec)	HR1 ACIS	HR2 ACIS	HR1 XMM	HR2 XMM	$\log L_X$ (erg/sec)
517	J205420.8+441528	313.58696	44.25804	3.89	30.555	3.467	0.08	0.19	-0.02	0.06	0.31	30.77
518	J205313.5+441600	313.30631	44.26682	7.02	23.701	4.263	-0.06	0.31	0.23	-0.08	0.23	31.23
519	J205351.9+441706	313.46657	44.28503	1.58	54.105	2.056	0.23	-0.08	0.12	0.30	0.19	31.19
520	J205429.2+441817	313.62167	44.30482	3.17	15.577	2.272	-0.12	0.30	0.12	-0.07	0.20	30.70
521	J205242.4+441919	313.17708	44.32202	3.35	32.224	2.717	-0.02	0.06	0.12	0.40	0.12	31.01
522	J205301.9+441921	313.25821	44.32274	1.55	48.971	3.521	0.12	0.40	0.12	0.20	0.12	30.99
523	J205432.8+442013	313.63705	44.33703	6.16	26.184	3.660	0.12	0.20	0.12	0.20	0.12	30.67
524	J205324.3+442034	313.35159	44.34279	2.23	20.719	1.570	0.12	-0.07	0.12	-0.07	0.12	30.58
525	J205341.5+442137	313.42328	44.36034	1.69	34.199	1.454	-0.02	-0.26	0.12	0.40	0.12	30.47
526	J205309.7+442151	313.29048	44.36442	2.63	8.194	1.605	-0.04	0.30	0.06	0.41	0.12	30.68
527	J205305.2+442206	313.27196	44.36849	2.74	7.638	1.651	-0.19	0.41	0.08	0.18	0.12	30.67
528	J205309.7+442220	313.29078	44.37229	2.59	7.723	1.504	-0.19	0.32	0.12	0.29	0.12	30.64
529	J205253.1+442221	313.22134	44.37259	3.85	12.069	2.558	-0.11	0.35	0.06	0.38	0.06	30.65
530	J205409.3+442258	313.53890	44.38303	0.90	17.420	1.613	0.06	0.38	0.08	0.18	0.08	30.70
531	J205346.6+442302	313.44431	44.38399	1.44	58.784	1.906	-0.04	0.02	0.04	0.02	0.04	30.70
532	J205424.8+442305	313.60368	44.38488	5.00	12.151	2.188	-0.18	0.29	0.12	0.29	0.12	30.01
533	J205313.4+442322	313.30592	44.38948	2.12	44.933	3.070	-0.58	0.06	0.29	0.12	0.26	30.30
534	J205418.6+442323	313.57777	44.38999	2.48	11.720	1.100	-0.29	0.12	0.04	0.02	0.10	30.24
535	J205330.9+442325	313.37895	44.39055	2.92	7.831	0.981	-0.04	0.02	0.04	0.02	0.04	30.24
536	J205323.9+442342	313.34966	44.39515	2.09	22.329	1.476	0.38	0.12	0.28	0.12	0.28	31.28
537	J205438.1+442402	313.65903	44.40062	2.20	6.084	0.859	0.26	0.07	0.21	0.35	0.21	30.30
538	J205450.0+442409	313.70870	44.40266	7.16	23.254	4.307	-0.21	0.35	0.04	0.04	0.04	30.30
539	J205337.7+442422	313.40746	44.40632	4.90	12.705	2.203	-0.00	0.04	0.00	0.04	0.04	30.44
540	J205413.4+442432	313.55606	44.40914	1.51	70.825	2.323	0.38	0.12	0.28	0.01	0.19	31.37
541	J205417.5+442532	313.57310	44.42580	4.57	17.471	2.696	0.03	0.19	0.03	0.19	0.03	30.67
542	J205358.2+442534	313.49268	44.42620	2.59	2.769	0.535	0.10	-0.01	0.10	-0.01	0.10	30.27
543	J205438.2+442543	313.65949	44.42876	5.90	14.789	1.918	-0.21	0.28	0.12	0.28	0.12	30.10
544	J205339.7+442550	313.41560	44.43059	1.87	24.785	1.290	0.27	-0.09	0.27	-0.09	0.27	30.69
545	J205346.4+442707	313.44366	44.45218	4.61	7.577	1.173	0.06	0.10	0.06	0.10	0.06	30.32
546	J205325.4+442716	313.35590	44.45453	2.56	17.985	1.769	0.08	-0.01	0.08	-0.01	0.08	30.72
547	J205322.1+442747	313.34250	44.46333	1.84	43.370	2.166	0.09	-0.35	0.09	-0.35	0.09	30.57
548	J205224.6+442814	313.10254	44.47082	6.30	17.672	2.557	-0.05	0.16	0.05	0.16	0.05	30.62
549	J205345.5+442816	313.43980	44.47123	5.90	28.958	3.758	-0.02	0.21	0.02	0.21	0.02	30.92
550	J205405.7+442842	313.52394	44.47845	5.36	11.297	2.330	-0.08	0.27	0.08	0.27	0.08	30.68
551	J205319.8+442844	313.33274	44.47903	2.27	24.859	1.902	0.14	-0.15	0.14	-0.15	0.14	30.65
552	J205250.0+442902	313.20839	44.48402	6.62	32.892	5.248	-0.06	0.28	0.06	0.28	0.06	31.52
553	J205244.9+442912	313.18745	44.48675	4.90	24.652	4.279	-0.01	0.23	0.01	0.23	0.01	30.82
554	J205357.4+442940	313.48949	44.49450	4.00	35.950	4.266	0.31	-0.22	0.31	-0.22	0.31	30.97
555	J205406.2+443025	313.52602	44.50721	2.95	28.979	3.759	0.26	-0.28	0.26	-0.28	0.26	30.67
556	J205347.2+443038	313.44678	44.51061	6.19	7.915	2.125	0.33	0.16	0.33	0.16	0.33	31.75
557	J205343.2+443108	313.43016	44.51891	5.11	15.111	5.315	0.32	0.06	0.32	0.06	0.32	31.95
558	J205340.9+443146	313.42068	44.52955	8.06	43.540	10.058	0.53	0.15	0.53	0.15	0.53	31.95
559	J205444.7+443146	313.68639	44.52948	7.60	46.772	9.622	0.01	-0.00	0.01	-0.00	0.01	30.69

Table 3. continued.

X-ray no.	CXO Id (CXOU)	XMM Id (XMMU)	RA (J2000)	Dec (J2000)	Pos. err. (arcsec)	Count rate (cts/ksec)	Rate error (cts/ksec)	HR1 ACIS	HR2 ACIS	HR1 XMM	HR2 XMM	$\log L_X$ (erg/sec)
560	J205435.3+442235	313.64711	44.54321	5.33	36.610	7.437		0.02	0.08			30.89
561	J205358.1+443238	313.49248	44.54406	4.43	25.754	3.745		0.17	-0.11			31.24
562	J205434.3+443309	313.64328	44.55263	5.11	14.533	5.091		-0.11	0.09			30.55
563	J205343.0+443345	313.42947	44.56262	3.89	11.858	2.564		0.62	0.04			30.96
564	J205340.3+443727	313.41829	44.62441	3.78	30.947	3.276		0.53	-0.15			31.18
565	J205226.7+441705	313.11152	44.28491	3.46	19.545	3.363		-0.07	0.06			30.54
566	J205211.3+441753	313.04747	44.29832	7.02	46.920	15.696		0.39	-0.22			30.90
567	J205249.8+441900	313.20785	44.31688	3.35	12.278	1.980		-0.11	0.08			30.53
568	J205301.5+441904	313.25642	44.31780	3.85	7.106	1.509		0.03	0.22			30.41
569	J205235.5+441910	313.14802	44.31953	4.68	13.853	2.209		0.06	0.14			30.36
570	J205212.7+441925	313.05309	44.32370	1.66	594.620	12.284		0.22	-0.07			31.70
571	J205212.7+442054	313.05307	44.34841	3.46	8.200	1.426		0.32	0.20			30.66
572	J205228.0+442112	313.11675	44.35352	3.71	6.192	1.209		-0.04	0.12			30.29
573	J205217.6+442114	313.07361	44.35404	3.60	6.978	1.310		0.03	-0.31			30.06
574	J205216.2+442157	313.06762	44.36590	9.50	10.814	3.334		0.03	0.14			30.49
575	J205242.7+442219	313.17823	44.37215	5.04	7.235	1.332		-0.20	0.25			29.82
576	J205146.2+442222	312.94278	44.37287	2.70	13.923	2.878		0.24	-0.31			30.39
577	J205348.5+442226	313.45239	44.37412	1.94	12.565	2.685		-0.43	-0.14			30.50
578	J205215.1+442307	313.06321	44.38536	4.18	12.262	1.588		-0.47	0.00			30.02
579	J205205.6+442334	313.02357	44.39302	3.13	10.400	1.507		-0.50	-0.11			29.95
580	J205212.1+442347	313.05077	44.39645	6.48	3.245	1.676		0.00	0.30			30.02
581	J205230.1+442410	313.12569	44.40301	2.70	4.122	0.871		0.04	0.02			29.90
582	J205208.2+442416	313.03447	44.40445	5.29	2.187	1.396		0.18	0.28			30.06
583	J205159.1+442543	312.99660	44.42872	3.82	20.294	2.188		-0.12	-0.40			30.63
584	J205225.0+442554	313.10458	44.43172	2.38	5.711	0.931		0.02	0.14			30.07
585	J205253.4+442557	313.22271	44.43265	5.58	5.182	1.148		-0.11	0.18			30.17
586	J205250.9+442556	313.21227	44.43248	4.21	2.468	0.620		-0.11	0.25			29.32
587	J205256.9+442600	313.23732	44.43361	3.82	3.599	0.752		0.02	0.16			30.22
588	J205209.6+442604	313.04005	44.43455	2.48	21.554	1.960		-0.06	-0.36			30.26
589	J205243.1+442611	313.17960	44.43640	4.28	2.634	0.681		0.10	0.10			29.82
590	J205144.6+442616	312.93622	44.43788	6.19	8.855	2.356		0.32	-0.38			30.10
591	J205232.5+442632	313.13583	44.44249	2.52	4.035	0.749		-0.01	-0.04			29.96
592	J205312.1+442635	313.30072	44.44308	3.38	5.139	0.863		0.04	0.10			30.20
593	J205331.5+442739	313.38159	44.46084	4.14	13.744	1.756		-0.04	0.18			30.55
594	J205212.6+442741	313.05289	44.46146	6.01	3.586	1.649		0.19	0.17			29.76
595	J205317.4+442802	313.32273	44.46728	3.64	15.871	1.575		0.14	0.14			30.10
596	J205215.1+442813	313.06308	44.47047	3.17	2.372	0.653		-0.05	-0.27			29.77
597	J205215.7+442814	313.21556	44.47072	3.38	4.591	0.764		0.03	0.16			30.10
598	J205235.1+442819	313.14627	44.47212	1.87	10.430	1.100		-0.31	-0.13			29.95
599	J205145.5+442836	312.93996	44.47680	7.24	10.624	2.004		0.06	0.01			30.46
600	J205314.3+442904	313.30999	44.48463	4.36	2.487	0.658		0.01	0.29			29.87
601	J205334.7+442916	313.39492	44.48793	3.74	6.579	1.320		0.02	-0.15			30.58
602	J205233.9+442917	313.14151	44.48809	5.00	10.869	1.961		-0.02	0.12			30.35

Table 3. continued.

X-ray no.	CXO Id (CXOU)	XMM Id (XMMU)	RA (J2000)	Dec (J2000)	Pos. err. (arcsec)	Count rate (cts/ksec)	Rate error (cts/ksec)	HR1 ACIS	HR2 ACIS	HR1 XMM	HR2 XMM	$\log L_X$ (erg/sec)
603	J205206.4+442921	313.02696	44.48927	3.10	4.148	1.112		0.23	-0.23			29.85
604	J205227.9+442939	313.11660	44.49420	2.27	21.445	1.631	-0.70	-0.17				
605	J205231.6+442958	313.13168	44.49968	2.23	21.377	1.616	0.15	-0.28				30.71
606	J205207.9+443003	313.03307	44.50099	1.94	55.600	3.116	0.75	0.41				31.59
607	J205220.1+443029	313.08377	44.50826	5.47	4.359	1.710	0.35	0.45				30.17
608	J205231.0+443032	313.12918	44.50910	4.28	3.195	0.829	0.16	0.24				29.93
609	J205324.2+443040	313.35107	44.51137	3.64	5.386	1.020	0.53	0.12				30.76
610	J205312.2+443103	313.30112	44.51753	4.79	5.571	0.934	0.18	0.02				30.41
611	J205200.3+443118	313.00126	44.52167	2.70	18.065	1.977	0.42	-0.07				30.74
612	J205340.5+443129	313.41888	44.52474	3.92	70.084	4.118	0.53	0.16				32.32
613	J205254.6+443134	313.22757	44.52618	2.34	5.149	0.830	0.19	-0.05				30.16
614	J205143.7+443218	312.93220	44.53852	5.11	10.419	1.976	0.07	0.04				30.25
615	J205201.3+443236	313.00546	44.54358	5.04	26.455	2.513	0.00	-0.28				30.58
616	J205307.0+443255	313.27943	44.54866	5.90	3.365	0.829	-0.04	0.34				29.99
617	J205235.1+443318	313.14653	44.55513	2.70	11.734	1.281	0.29	-0.28				30.59
618	J205315.9+443321	313.31641	44.55609	3.78	5.219	1.068	0.09	0.15				30.50
619	J205241.6+443407	313.17338	44.56865	2.45	1.660	0.533	0.22	-0.17				29.63
620	J205226.0+443426	313.10864	44.57408	2.70	15.293	1.640	0.32	-0.31				30.44
621	J205158.4+443504	312.99348	44.58445	7.31	11.147	2.148	-0.29	0.08				30.03
622	J205245.1+443524	313.18820	44.59005	2.16	3.203	0.834	0.07	-0.15				29.90
623	J205229.0+443604	313.12108	44.60123	3.38	7.386	1.238	0.19	-0.11				30.02
624	J205322.6+443608	313.34456	44.60232	5.40	6.811	1.426	0.30	0.02				30.52
625	J205250.3+443645	313.20983	44.61253	4.03	14.466	1.727	-0.73	0.32				30.09
626	J205300.7+443658	313.25295	44.61637	2.41	101.920	4.419	0.45	-0.24				29.96
627	J205226.6+443706	313.11084	44.61853	3.02	43.592	3.046	0.43	-0.19				31.10
628	J205158.3+443725	312.99300	44.62373	3.92	7.105	1.566	0.17	-0.08				30.25
629	J205224.5+443755	313.10223	44.63199	4.75	10.685	1.761	0.34	-0.14				29.96
630	J205215.4+443802	313.06420	44.63407	7.20	10.626	1.999	-0.13	0.26				
631	J205317.0+443834	313.32097	44.64297	2.23	45.448	3.400	0.60	-0.16				31.26
632	J205229.4+443840	313.12257	44.64471	2.70	5.821	1.216	0.60	-0.29				30.32
633	J205322.2+443852	313.34281	44.64800	2.84	21.781	2.603	0.12	-0.27				30.64
634	J205243.7+443859	313.18243	44.64983	4.28	4.565	1.164	0.35	-0.16				30.51
635	J205329.9+443934	313.37471	44.65962	4.00	8.368	1.900	0.27	-0.13				30.36
636	J205251.5+443952	313.21497	44.66471	4.32	15.932	2.182	0.02	0.62				30.92
637	J205336.6+443952	313.40274	44.66465	3.20	25.520	3.887	0.31	-0.13				30.79
638	J205208.2+444027	313.03421	44.67440	8.60	9.045	4.220	0.13	0.20				30.77
639	J205311.9+444033	313.29990	44.67598	8.68	7.447	3.536	0.35	0.00				30.36
640	J205256.9+444045	313.23747	44.67917	5.51	8.053	3.207	0.23	-0.15				30.32
641	J205301.1+444057	313.25483	44.68251	5.04	12.235	2.262	-0.16	0.11				30.22
642	J205329.5+444106	313.37293	44.68513	8.75	11.678	5.608	0.07	-0.16				30.27
643	J205310.3+444130	313.29302	44.69190	3.46	44.266	3.991	-0.48	-0.24				30.58
644	J205310.8+444218	313.29521	44.70508	5.04	14.061	2.593	0.10	0.01				30.58
645	J205239.9+441615	313.16647	44.27085	6.66	19.823	3.203	-0.11	0.38				31.08

Table 3. continued.

X-ray no.	CXO Id (CXOU)	XMM Id (XMMU)	RA (J2000)	Dec (J2000)	Pos. err. (arcsec)	Count rate (cts/ksec)	Rate error (cts/ksec)	HR1 ACIS	HR2 ACIS	HR1 XMM	HR2 XMM	$\log L_X$ (erg/sec)
646	J205433.9+442010	313.64149	44.33612	2.95	8.771	1.136	0.17	0.09	0.17	0.09	30.43	
647	J205431.7+442016	313.63219	44.33799	2.20	6.265	0.883	0.22	0.12	0.22	0.12	30.36	
648	J205223.1+442218	313.09652	44.37169	8.50	8.802	2.229	-0.03	0.20	-0.03	0.20	30.48	
649	J205223.8+442308	313.09921	44.38570	8.39	9.967	2.476	-0.08	0.29	-0.08	0.29	30.91	
650	J205353.4+442311	313.47279	44.38665	0.50	8068.400	19.930	-0.43	-0.52	-0.43	-0.52		
651	J205333.5+442514	313.38965	44.42063	6.37	8.268	1.222	0.01	0.19	0.01	0.19	30.27	
652	J205342.1+442658	313.42554	44.44966	5.18	17.506	1.761	-0.17	0.08	-0.17	0.08		
653	J205355.5+443038	313.48155	44.51059	8.64	12.374	3.219	0.17	0.02	0.17	0.02	30.69	
654	J205337.4+443458	313.40597	44.58292	4.57	2.630	1.347	0.35	0.16	0.35	0.16		
655	J205054.0+443808	312.72513	44.63561	4.46	17.339	2.528	0.10	-0.13	0.10	-0.13	30.73	
656	J205044.6+443838	312.68605	44.64403	5.26	6.040	1.207	-0.01	0.08	-0.01	0.08		
657	J205053.1+443856	312.72155	44.64906	3.02	3.363	0.856	0.16	0.56	0.16	0.56	30.28	
658	J205040.3+443929	312.66816	44.65827	4.61	8.472	1.309	0.28	0.43	0.28	0.43	30.03	
659	J205134.8+443939	312.89526	44.66094	4.54	40.933	6.136	0.48	0.08	0.48	0.08	31.10	
660	J205052.1+444004	312.71743	44.66793	3.46	6.326	1.088	0.52	0.23	0.52	0.23	30.67	
661	J205118.2+444027	312.82600	44.67420	4.72	11.075	1.800	0.03	-0.08	0.03	-0.08	30.40	
662	J205059.4+444047	312.74787	44.67990	2.12	64.128	4.381	0.51	-0.15	0.51	-0.15	31.31	
663	J205030.8+444054	312.62862	44.68178	2.56	16.742	1.610	0.45	0.57	0.45	0.57	30.72	
664	J205027.6+444119	312.61514	44.68881	2.81	2.775	0.624	0.29	-0.07	0.29	-0.07	29.50	
665	J205057.8+444307	312.74107	44.71880	4.43	7.593	1.090	0.29	-0.05	0.29	-0.05	30.64	
666	J205037.1+444315	312.65486	44.72085	3.46	4.876	0.842	-0.34	0.09	-0.34	0.09	29.62	
667	J205109.9+444346	312.79126	44.72964	6.44	8.110	1.228	-0.22	0.26	-0.22	0.26	29.84	
668	J205047.5+444355	312.69825	44.73204	5.26	3.817	0.755	0.18	0.14	0.18	0.14	30.39	
669	J205029.9+444548	312.62495	44.76352	5.47	2.842	0.606	0.11	0.42	0.11	0.42	29.77	
670	J205043.5+444627	312.68132	44.77426	3.28	3.838	0.599	-0.55	0.14	-0.55	0.14	29.51	
671	J204939.4+444626	312.41419	44.777401	1.84	3.554	1.296	-0.78	0.20	-0.78	0.20		
672	J205126.4+444722	312.86014	44.78963	3.71	4.071	0.799	-0.08	0.46	-0.08	0.46	30.48	
673	J205027.7+444729	312.61575	44.79153	4.10	1.863	0.442	0.27	0.31	0.27	0.31	29.73	
674	J205049.3+444753	312.70564	44.79810	2.16	13.645	0.948	0.63	0.49	0.63	0.49	30.90	
675	J205105.7+444753	312.77387	44.79816	6.98	4.352	0.773	0.12	0.13	0.12	0.13	30.82	
676	J205043.6+444805	312.68168	44.80161	2.20	3.513	0.499	0.31	0.47	0.31	0.47	29.79	
677	J205014.5+444820	312.56082	44.80582	4.86	4.486	0.767	-0.12	0.34	-0.12	0.34	29.92	
678	J205041.2+444838	312.67186	44.81073	2.84	1.580	0.357	-0.54	-0.03	-0.54	-0.03	29.13	
679	J204950.9+444913	312.46209	44.82033	3.02	2.305	0.585	0.40	0.19	0.40	0.19	29.88	
680	J205042.6+444917	312.67758	44.82150	3.82	2.005	0.418	-0.02	0.40	-0.02	0.40	29.73	
681	J205016.0+444919	312.56698	44.82216	5.26	4.001	0.794	-0.08	0.47	-0.08	0.47	29.95	
682	J205124.6+444932	312.85254	44.82556	3.13	5.523	0.796	0.54	0.25	0.54	0.25	31.17	
683	J205132.3+444933	312.88499	44.82585	1.94	2.046	0.805	1.00	0.57	1.00	0.57	30.63	
684	J205045.4+444934	312.68925	44.82633	1.91	1.616	0.336	-0.62	-0.50	-0.62	-0.50	29.14	
685	J204958.5+444937	312.49406	44.82722	1.80	3.353	0.615	0.30	0.60	0.30	0.60	29.86	
686	J205031.8+444946	312.63267	44.82955	2.20	13.947	0.991	-0.65	-0.04	-0.65	-0.04	30.07	
687	J205002.9+444946	312.51227	44.82968	4.86	5.057	0.865	-0.49	0.30	-0.49	0.30	29.63	
688	J204958.1+444952	312.49245	44.83134	5.11	14.337	1.393	-0.17	0.34	-0.17	0.34	31.21	

Table 3. continued.

X-ray no.	CXO Id (CXOU)	XMM Id (XMMU)	RA (J2000)	Dec (J2000)	Pos. err. (arcsec)	Count rate (cts/ksec)	Rate error (cts/ksec)	HR1 ACIS	HR2 ACIS	HR1 XMM	HR2 XMM	$\log L_X$ (erg/sec)
689	J205042.7+445014	312.67804	44.83741	4.03	1.611	0.367		0.10	0.26			30.01
690	J205118.2+445034	312.82605	44.84301	2.92	5.874	0.734		0.50	0.44			
691	J205039.3+445052	312.66395	44.84799	3.02	4.013	0.546		0.18	0.46			30.24
692	J205018.2+445055	312.57620	44.84881	2.56	2.628	0.501		-0.36	0.02			30.13
693	J205105.4+445058	312.77258	44.84954	2.20	1.071	0.290		0.33	-0.33			29.82
694	J205034.1+445104	312.64222	44.85129	2.30	11.214	0.882		-0.56	-0.23			29.98
695	J205211.4+445107	313.04771	44.85201	2.92	7.136	1.715		-0.39	-0.05			29.78
696	J205109.8+445124	312.79088	44.85673	3.13	4.275	0.613		0.38	0.00			31.21
697	J205051.4+445144	312.71448	44.86246	3.82	1.902	0.393		-0.32	0.17			29.21
698	J205032.3+445147	312.63468	44.86325	4.61	4.269	0.659		0.12	0.38			31.63
699	J205045.2+445201	312.68848	44.86701	7.70	3.080	0.653		0.06	0.23			30.32
700	J205047.9+445258	312.69997	44.88284	2.81	5.814	0.674		-0.61	0.05			29.69
701	J205149.6+445309	312.95684	44.88601	4.90	8.071	1.402		-0.47	0.20			29.87
702	J205108.9+445311	312.78711	44.88657	1.55	14.544	1.060		0.76	0.42			31.66
703	J205033.7+445347	312.64072	44.89647	3.92	7.109	0.812		0.28	0.43			31.05
704	J205101.5+445419	312.75664	44.90542	4.21	5.951	0.774		0.09	0.45			31.11
705	J205000.0+445421	312.50023	44.90601	5.04	5.013	0.926		-0.27	0.10			
706	J205154.4+445433	312.97707	44.90932	3.35	29.540	2.483		-0.58	0.06			30.42
707	J205045.5+445453	312.68964	44.91486	1.62	48.216	1.925		0.67	0.64			
708	J205032.8+445456	312.63691	44.91557	2.38	3.367	0.560		0.58	0.57			30.03
709	J205025.0+445509	312.60424	44.91938	2.77	31.650	1.854		-0.42	-0.07			30.43
710	J205045.6+445512	312.69035	44.92007	1.48	1.435	0.355		0.38	-0.08			
711	J205030.2+445513	312.62611	44.92050	2.02	1.586	0.363		0.60	0.36			29.63
712	J205040.0+445518	312.66689	44.92178	2.70	7.931	0.855		-0.66	0.16			29.83
713	J205105.1+445532	312.77159	44.92572	3.53	3.446	0.618		-0.42	0.16			29.47
714	J205137.5+445617	312.90630	44.93815	2.30	2.264	0.667		-0.60	0.43			30.19
715	J204943.0+445702	312.42937	44.95061	3.67	6.247	1.202		0.45	0.27			30.72
716	J205008.8+445812	312.53678	44.97020	4.25	10.012	1.321		-0.34	0.06			29.93
717	J205105.8+445950	312.77429	44.99732	5.58	4.861	1.073		-0.45	0.55			29.62
718	J205043.9+450126	312.68328	45.02394	4.46	9.305	1.363		-0.39	0.23			29.93
719	J205055.3+450335	312.73068	45.05983	2.30	44.973	3.659		-0.67	-0.40			30.58
720	J205122.5+450402	312.84381	45.06749	4.43	22.880	3.272		0.25	0.45			30.56
721	J205033.7+450434	312.64048	45.07638	1.44	4.004	0.929		-0.85	0.00			29.69

X-ray no.	<i>i</i>	<i>r</i> − <i>i</i>	<i>r</i> − <i>Hα</i>	<i>J</i>	<i>H</i>	<i>K</i>	IR excess	Hα excess	RGS11 number
1									
2				13.52	12.70	12.35			
3									
4									
5									
6				14.21	12.81	12.10			
7				13.22	11.53	10.51			98
8				15.82	15.15	14.60			
9	17.06	1.93	2.14	13.92	12.74	12.12			
10				20.00	18.12	17.21	Y	101	
11				14.92	13.32	12.63			
12									
13				14.38	12.96	12.35			
14									
15				11.25	11.06	11.00			
16									
17				14.88	11.85	9.75			116
18				19.55	17.59	16.59			
19	16.07	1.44	1.24	13.80	12.78	12.15	Y	121	
20									
21									
22									
23				16.57	13.71	12.27			
24				12.09	11.03	10.56			
25				11.27	10.21	9.66			130
26				11.86	10.94	10.51			131
27									134
28	16.45	2.38	0.66	12.85	11.39	10.87			
29				20.34	18.24	17.47			
30	14.69	1.45	0.68	12.59	11.69	11.38			
31	16.41	2.08	1.18	13.73	12.81	12.33			
32				12.75	11.56	11.10			
33				18.18	14.89	13.02			
34				14.63	13.20	12.43			
35				12.35	10.57	9.55			
36				15.52	14.87	14.40			
37				15.62	13.78	12.95			
38				13.39	12.46	12.05			
39									146
40									
41				17.76	15.88	15.03			150
42									152
43				12.14	11.09	10.48			

Table 4. Optical/NIR photometry for X-ray sources.

Table 4. continued.

X-ray no.	<i>i</i>	<i>r</i> − <i>i</i>	<i>r</i> − <i>Hα</i>	<i>J</i>	<i>H</i>	<i>K</i>	IR excess	<i>Hα</i> excess	RGS11 number
44			16.83	13.20	11.19				156
45			14.00	12.14	11.37				
46			12.93	11.95	11.64				157
47			12.48	11.55	11.11				
48			17.11	16.02	15.49				
49									
50									
51			16.45	14.02	12.69				
52				13.76	13.01	11.77			163
53				14.02	12.96	12.37			164
54	16.57	1.67	0.81	14.30	13.42	13.10			
55				13.12	12.10	11.62			166
56				12.95	11.96	11.48			167
57									
58				16.55	12.76	10.49			171
59									
60									
61				15.23	13.10	11.93			
62				15.95	12.82	11.00			
63									
64									
65				15.20	12.67	11.27			
66				15.39	13.60	12.58			
67				20.04	15.82	13.50			
68									
69									
70	15.62	1.88	1.05	12.19	11.31	10.79			177
71				13.46	12.41	11.95			178
72									
73				14.62	12.80	12.03			
74				12.64	11.18	10.20			
75				11.85	11.01	10.64			180
76				12.80	11.11	10.09			181
77									185
78									
79									
80	17.37	2.11	1.49	14.62	13.81	13.44			
81				14.69	13.58	12.90			
82				14.04	13.12	12.78			
83				12.36	11.36	10.81			188
84	17.41	2.10	1.20	14.79	13.97	13.59			
85	16.02	2.08	0.85	13.42	12.43	12.12			
86									

Table 4. continued.

X-ray no.	<i>i</i>	<i>r</i> − <i>i</i>	<i>r</i> − <i>H</i> α	<i>J</i>	<i>H</i>	<i>K</i>	IR excess	Hα excess	RGS11 number
87	13.09	0.50	0.35	12.16	11.69	11.57			
88	16.75	1.88	0.79	14.45	13.55	13.21			
89									
90	16.13	1.86	0.81	13.85	12.98	12.63			
91				13.92	12.46	11.67			
92									
93				17.36	16.34	15.98			
94				18.98	17.55	16.94			
95				13.23	12.36	12.05			
96				12.54	11.76	11.53			196
97				11.65	10.73	10.34			197
98				16.83	15.19	14.42			
99	14.77	1.24	0.85	12.58	11.65	11.15			
100				14.33	13.31	12.65			
101	17.51	1.89	1.07	15.56	14.94	14.68			
102	16.16	1.53	1.39	13.75	12.69	12.08			
103				14.63	13.49	13.04			
104									
105				13.48	12.63	12.23			
106				14.31	13.37	13.02			
107									
108	15.23	1.31	0.68	13.10	12.11	11.81			
109	14.23	1.03	0.95	12.41	11.45	10.95			
110				14.20	13.37	12.92			
111				14.79	14.09	13.69			
112	17.53	1.95	0.89	15.58	14.99	14.71			
113									
114				13.64	12.69	12.32			
115				13.34	12.28	11.77			
116	13.78	0.49	0.30	13.00	12.69	12.55			
117									
118	16.24	2.12	0.93	13.58	12.74	12.38			
119				11.99	10.86	10.04			224
120				11.99	10.86	10.04			224
121				20.42	18.64	18.19			227
122				13.12	12.08	11.59			228
123	14.52	1.28	0.55	11.83	10.81	10.18			230
124	14.68	0.96	0.55	13.37	12.75	12.55			
125				13.32	12.57	12.35			
126									
127									
128	16.37	2.11	0.93	14.04	13.32	12.82			
129				13.82	12.97	12.59			
				15.38	14.40	13.94			238

Table 4. continued.

X-ray no.	<i>i</i>	<i>r</i> − <i>i</i>	<i>r</i> − <i>H</i> α	<i>J</i>	<i>H</i>	<i>K</i>	IR excess	Hα excess	RGS11 number
130				11.79	11.57	11.40			
131	16.66	2.53	0.95	16.42	15.33	14.82			
132	16.26	1.30	0.56	13.83	13.04	12.66			
133				14.32	13.44	13.17			
134				10.87	10.15	9.94			
135									257
136	16.50	2.43	0.95	13.76	13.01	12.63			
137									
138	17.09	1.97	0.32	13.70	12.51	11.99			
139	17.05	1.88	0.93	14.79	13.92	13.58			
140	15.31	1.24	0.64	13.19	12.24	11.56	Y		
141				15.59	15.01	14.68			
142	15.82	1.38	0.69	12.28	11.31	10.87			
143	14.55	0.88	0.87	12.76	11.99	11.59	Y		259
144				14.97	14.06	13.76			
145	16.09	1.58	1.09	13.31	12.39	11.79	Y		
146				17.63	16.10	15.41			263
147	15.57	1.29	1.00	13.71	12.60	11.76	Y		
148									269
149	15.40	1.83	0.91	13.13	12.24	11.90			
150	14.16	1.17	1.17	11.88	10.96	10.30	Y		271
151	12.43	0.76	0.39	11.18	10.66	10.45			
152	14.88	1.12	1.06	12.78	11.70	10.99	Y		
153									278
154	16.20	1.43	1.26	13.85	12.83	12.25	Y		
155				15.64	14.39	13.83			
156				14.45	13.36	12.55			287
157	16.20	1.95	0.95	13.84	12.91	12.54			
158	16.49	1.92	1.17	13.88	12.85	12.22			
159									290
160									
161									
162	15.96	1.37	0.65	20.21	18.75	18.30			
163				15.10	13.69	12.75	Y		301
164				14.01	13.10	12.65			303
165				18.10	16.81	16.25			
166				14.58	13.87	13.57			
167				15.48	14.07	13.20			304
168				17.65	16.52	16.03			
169				19.69	18.57	17.68			
170	16.20	1.80	0.73	11.65	10.68	10.09			319
171				13.80	12.88	12.52			
172	13.89	1.22	0.52	11.75	10.92	10.41			328

Table 4. continued.

X-ray no.	<i>i</i>	<i>r</i> − <i>i</i>	<i>r</i> − <i>Hα</i>	<i>J</i>	<i>H</i>	<i>K</i>	IR excess	<i>Hα</i> Y	RGS11 number
173	14.89	1.14	0.93	12.85	11.94	11.20	Y	Y	334
174				15.73	14.78	14.35			
175				16.07	13.86	12.87			
176	16.10	1.57	0.83	14.46	13.83	13.59			
177				11.34	11.03	10.94			
178				17.28	15.33	14.42			
179				11.53	11.07	10.98			
180									
181									
182	17.87	1.97	0.84	14.92	13.69	13.18			
183				13.10	11.84	11.06			
184								853	
185									
186	18.19	2.11	0.95	15.19	14.02	13.56			
187									
188									
189	16.06	2.04	0.66	15.93	14.31	13.56			
190									
191									
192									
193									
194									
195									
196									
197									
198	18.03	1.88	0.96	16.10	15.49	15.16			
199									
200	17.57	2.08	1.25	13.87	12.46	11.66			
201									
202									
203									
204									
205									884
206									
207									
208									
209	17.45	1.67	0.68	14.85	13.83	13.44			
210									
211									
212									
213									
214									
215									

Table 4. continued.

X-ray no.	<i>i</i>	<i>r</i> - <i>i</i>	<i>r</i> - <i>Hα</i>	<i>J</i>	<i>H</i>	<i>K</i>	IR excess	<i>Hα</i> excess	RGS11 number
216				17.04	16.45	16.25			
217									907
218									909
219									
220	19.15	1.40	0.84	15.86	14.33	13.70			
221				13.88	13.20	12.94			
222									
223									
224									
225	15.96	2.48	1.17	13.29	12.54	12.21			
226				15.54	14.16	13.60			
227									
228									
229									
230	15.40	2.07	1.25	12.83	11.99	11.68			922
231	15.59	1.58	0.69	13.23	12.18	11.78			923
232				15.33	14.22	13.62			925
233					20.10	18.48	18.01		
234									
235									
236									
237									
238									
239	17.05	2.91	0.84	12.14	10.37	9.58			
240				9.87	9.51	9.38			
241									944
242				17.37	15.06	14.01			
243									
244									
245									
246									
247									
248									
249									
250									
251									
252									
253									
254									
255									
256									
257									
258	16.53	1.65	0.84	14.73	14.10	13.84			967
									972

Table 4. continued.

X-ray no.	<i>i</i>	<i>r</i> - <i>i</i>	<i>r</i> - <i>H</i> α	<i>J</i>	<i>H</i>	<i>K</i>	IR excess	<i>H</i> α excess	RGS11 number
259				16.33	13.85	12.72			
260									979
261									981
262									982
263									983
264									
265	17.49	2.34	0.67	13.87	12.55	11.99			
266									
267									
268									
269									
270	13.89	0.53	0.31	13.00	12.51	12.42			
271									
272	16.57	1.96	0.98	14.19	13.46	13.10			
273									
274									
275									
276									
277									
278	16.53	2.34	1.37	13.84	13.08	12.59			997
279									
280									998
281									
282	16.47	1.59	0.86	14.30	12.80	11.91			1005
283									
284									
285									
286									
287									
288									
289									
290									
291	17.89	2.52	0.86	13.75	12.06	11.19			1018
292									1021
293									1023
294									1027
295									
296									
297									
298									
299									
300									
301									1049

Table 4. continued.

X-ray no.	<i>i</i>	<i>r</i> − <i>i</i>	<i>r</i> − <i>Hα</i>	<i>J</i>	<i>H</i>	<i>K</i>	IR excess	<i>Hα</i> excess	RGS11 number
302									1051
303	16.83	14.45							1065
304	15.23	13.11							1067
305	15.89	13.98							
306									
307									
308									
309	16.44	13.39							
310	15.12	13.08							
311	16.14	13.81							1069
312	18.22	2.58	1.09						
313									
314	16.35	13.60							
315	16.66	14.14							1079
316									
317	12.12	11.52							
318	19.92	18.37							
319									
320	14.21	12.47							
321									
322									
323									
324									
325	14.75	0.93	0.50						
326									
327									
328	17.28	1.97	0.91						
329									
330									
331									
332	15.32	1.41	0.76						
333									
334	17.12	2.47	1.54						
335									
336									
337									
338									
339									
340									
341									
342									
343									
344									

Table 4. continued.

X-ray no.	<i>i</i>	<i>r</i> − <i>i</i>	<i>r</i> − <i>Hα</i>	<i>J</i>	<i>H</i>	<i>K</i>	IR excess	<i>Hα</i> excess	RGS11 number
345									
346	12.69	11.49	10.92						1179
347	14.57	13.82	13.33						
348	1.51	1.31	12.80	11.49	10.71	Y	Y	Y	1185
349			14.09	12.70	11.98				
350			12.77	11.81	11.34				
351									
352			15.68	13.54	12.09				1188
353									
354									
355			10.56	9.62	8.84				1190
356									
357	14.48	1.36	0.83	12.23	11.16	10.69	Y	Y	1192
358									
359									
360	16.88	1.88	1.31	13.60	12.40	11.73	Y	Y	1196
361									
362	16.47	1.27	1.06	13.85	12.82	12.14	Y	Y	1198
363									
364									
365	16.88	1.87	1.16	15.04	13.84	13.05	Y	Y	
366	15.79	1.66	1.10	13.76	12.82	12.37	Y	Y	1203
367									
368									
369	16.52	1.74	0.88	18.61	16.90	16.14			
370									
371									
372				15.25	13.07	11.35	Y		
373				12.00	11.43	11.28			
374	16.84	1.55	0.63	14.33	13.30	12.91			
375									
376									
377									
378	16.07	1.79	0.51	13.27	12.12	11.67			
379					5.09	4.46	4.45		
380	18.06	1.40	0.85	15.94	15.10	14.78			
381	14.42	2.16	0.55	10.50	8.94	8.23			
382	17.54	1.14	0.52	15.90	15.23	14.81			
383	14.56	0.73	0.42	13.54	12.93	12.81			
384					10.71	10.44	10.41		
385					17.85	16.69	16.22		
386					13.88	12.77	12.37		
387	16.53	1.60	0.61						

Table 4. continued.

X-ray no.	<i>i</i>	<i>r</i> − <i>i</i>	<i>r</i> − <i>Hα</i>	<i>J</i>	<i>H</i>	<i>K</i>	IR excess	<i>Hα</i> excess	RGS11 number
388	16.66	2.06	1.01	13.13	12.52	12.26			
389	17.48	2.07	0.98	12.67	11.48	10.73			
390	17.05	1.82	1.06	15.42	14.81	14.49			
391	17.37	1.41	0.54	15.24	14.62	14.35			
392	16.80	1.90	1.00	16.84	15.76	15.25			
393				10.83	10.45	10.40			
394				17.08	15.93	15.38			
395				14.95	14.34	14.05			
396	15.52	1.65	0.88	13.85	13.28	13.01			
397	16.75	1.85	0.89	14.96	14.37	14.07			
398	17.79	1.54	0.41	15.30	14.38	13.97			
399	18.03	1.13	0.41	16.75	15.74	15.30			
400									
401	18.17	1.40	0.58	13.42	12.49	12.17			
402				16.40	15.65	15.31			
403									
404	16.94	1.75	0.68	14.21	13.11	12.66			
405	16.22	1.92	0.99	14.22	13.62	13.33			
406									
407									
408	18.13	1.11	0.39	11.71	10.91	10.52			
409									
410	15.55	1.01	0.47	13.57	12.73	12.44			
411				13.98	13.22	12.98			
412									
413									
414	16.10	1.20	1.15	7.67	7.08	6.94			
415				14.34	13.41	12.96			
416									
417									
418	17.03	1.61	0.75	14.79	13.89	13.58			
419	15.75	1.09	0.58	16.88	16.11	15.79			
420	15.32	0.89	0.34	11.94	11.71	11.66			
421	18.22	1.24	0.62	16.30	15.52	15.23			
422	16.39	1.70	0.72	13.93	12.92	12.54			
423	16.93	1.02	0.45	12.21	11.79	11.71			
424	16.34	1.49	0.62	16.67	16.03	15.76			
425	17.70	1.13	0.28	13.05	12.50	12.38			
426				13.04	12.19	11.91			
427	17.96	1.10	0.42	16.28	15.70	15.51			
428	13.68	0.88	0.41	12.21	11.40	10.89			
429	18.49	1.11	0.41	13.10	12.49	12.28			
430				12.16	11.42	11.24			

Table 4. continued.

X-ray no.	<i>i</i>	<i>r</i> − <i>i</i>	<i>r</i> − <i>Hα</i>	<i>J</i>	<i>H</i>	<i>K</i>	IR excess	<i>Hα</i> excess	RGS11 number
431	15.24	1.33	1.25	13.11	11.87	11.05	Y	Y	1131
432				13.83	12.78	12.29			1147
433				13.35	12.24	11.69			1145
434				15.93	15.31	15.03			
435	17.94	1.93	1.04						
436	14.64	0.80	0.47	13.43	12.76	12.63			1099
437				15.10	13.61	12.99			
438				11.46	11.12	11.05			
439	15.74	1.26	0.83	13.88	13.06	12.64	Y	Y	1138
440				13.97	13.02	12.67			
441	15.29	1.14	0.63	13.80	13.09	12.90			
442	14.32	1.71	0.92	12.56	11.96	11.72			
443				13.75	13.16	12.91			
444				11.65	11.38	11.30			
445	17.04	1.91	0.61	15.41	13.60	12.71	Y	Y	1062
446				15.23	13.07	12.11			
447	14.62	1.26	0.61	12.75	11.94	11.69			
448				13.79	12.37	11.79			
449				14.72	13.86	13.63			
450				10.55	9.85	9.44			1230
451	13.91	0.66	0.42	12.90	12.32	12.20			
452				17.14	16.13	15.69			
453	17.12	1.75	0.82	15.34	14.67	14.34			
454	17.05	0.62	1.38	14.13	12.48	11.23	Y	Y	1212
455				13.64	12.92	12.72			
456				16.78	15.77	15.33			
457	15.27	1.08	1.33						
458				12.71	11.87	11.62			
459	15.87	1.68	0.64	15.43	14.22	13.75			
460				13.58	13.02	12.77			
461	16.79	2.05	0.64	13.99	12.96	12.54			
462	18.06	1.60	0.12	16.49	14.89	14.23	Y	Y	
463	16.10	1.91	1.05	14.11	13.53	13.24			
464				10.35	9.79	9.64			
465				10.47	10.13	10.14			
466				10.54	10.28	10.26			
467	18.17	1.56	0.82	16.04	14.23	13.43	Y	Y	
468				13.47	12.67	12.34			
469	17.87	1.88	0.57	13.84	13.24	12.99			
470				16.95	16.31	16.00			
471	18.19	1.75	0.60	15.77	14.88	14.43			
472	14.01	0.69	0.42	12.93	12.39	12.15			
473	13.16	0.52	0.38	12.21	11.73	11.63			

Table 4. continued.

X-ray no.	<i>i</i>	<i>r</i> − <i>i</i>	<i>r</i> − <i>Hα</i>	<i>J</i>	<i>H</i>	<i>K</i>	IR excess	<i>Hα</i> excess	RGS11 number
474	15.27	1.75	0.94	13.41	12.85	12.57			
475				18.03	16.92	16.37			
476				20.47	18.59	17.66			
477				16.73	15.73	15.29			
478	16.78	1.20	0.69	15.30	14.52	14.29			
479				16.60	14.37	13.20			
480	18.05	2.40	0.88	14.41	13.37	13.00			
481	14.63	0.57	0.34	12.19	10.99	10.52			
482				19.80	18.26	17.39			
483				13.56	12.84	12.49			
484				13.81	12.80	12.44			
485				12.97	12.34	12.12			
486				20.05	18.49	17.74			
487	17.30	1.93	0.99	15.32	14.75	14.44			
488				11.91	11.45	11.33			
489				16.61	15.70	15.28			
490				8.08	7.66	7.48			
491				13.54	12.98	12.88			
492	17.13	1.90	0.59	14.51	13.58	13.18			
493				18.56	17.33	16.82			
494				15.76	14.54	14.03			
495				15.24	13.78	13.16			
496	15.72	1.43	0.76	14.10	13.46	13.22			
497									
498				16.20	15.35	14.85			
499	13.29	0.90	0.40	11.91	11.30	11.19			
500				20.90	18.51	17.55			
501				17.82	16.57	16.05			
502				15.50	13.39	12.49			
503				14.41	13.76	13.52			
504				13.39	12.26	11.92			
505				14.99	13.29	12.56			
506	18.33	1.81	0.83	13.60	12.58	12.21			
507				13.40	12.24	11.64			
508				14.26	13.22	12.85			
509									
510				19.91	16.18	14.15			
511				14.68	14.10	13.80			
512				13.42	12.84	12.70			
513				17.27	15.80	15.22			
514				12.35	12.08	11.94			
515									
516	14.18	1.37	0.73	15.80	14.51	13.98			
								Y	

Table 4. continued.

X-ray no.	<i>i</i>	<i>r</i> − <i>i</i>	<i>r</i> − <i>Hα</i>	<i>J</i>	<i>H</i>	<i>K</i>	IR excess	<i>Hα</i> excess	RGS11 number
517	16.40	2.05	0.61	11.51	10.59	10.19			
518	14.52	1.17	0.48	14.58	12.91	12.19			553
519				16.36	15.24	14.78			
520				15.14	14.00	13.43			
521	16.17	1.55	0.64	15.97	14.86	14.25			485
522				12.93	11.99	11.67			
523	15.94	2.06	0.53	12.41	11.19	10.59			
524	12.65	0.97	0.46	11.16	10.49	10.31			541
525				14.32	13.00	12.11			
526				16.07	14.56	13.88			
527				16.56	15.14	14.51			
528				16.44	15.21	14.65			
529									
530									
531	15.16	1.55	0.83	9.40	9.03	8.84			
532				13.50	12.92	12.65			
533									
534	17.05	1.62	0.83	15.35	14.71	14.43			
535				12.12	11.18	10.70			591
536				13.05	11.32	10.36			573
537				15.85	14.66	14.15			
538				11.90	11.63	11.58			
539				13.56	12.60	12.18			
540	15.27	1.63	0.76	12.31	11.18	10.55			617
541	16.47	1.78	0.61	13.72	12.63	12.22			680
542				13.70	12.16	11.30			
543				11.21	10.84	10.73			
544	14.29	1.57	0.59	11.78	10.83	10.45			
545	16.58	1.97	0.74	13.79	12.65	12.26			639
546				12.78	11.62	11.20			
547				9.72	9.21	9.00			
548	16.88	2.08	0.82	14.10	13.08	12.69			568
549	16.82	1.66	0.59	13.93	12.81	12.35			
550				17.24	15.84	15.44			
551				12.54	11.62	11.28			
552	17.02	1.46	0.70	17.42	15.51	14.66			634
553				16.47	15.44	14.91			
554				12.33	11.27	10.86			
555									
556	16.60	1.45	0.75	13.88	12.38	11.76			
557				17.33	14.17	12.63			
558	16.01	2.81	0.72	14.72	12.29	10.69			
559	13.09	1.19	0.50	11.25	10.54	10.29			729

Table 4. continued.

X-ray no.	<i>i</i>	<i>r</i> − <i>i</i>	<i>r</i> − <i>Hα</i>	<i>J</i>	<i>H</i>	<i>K</i>	IR excess	Hα excess	RGS11 number
560	15.85	1.53	0.64	13.43	12.41	12.10			
561	14.12	1.66	0.61	15.99	14.38	13.66	Y		
562	15.78	1.67	0.66	13.14	12.13	11.71			
563				12.99	11.30	10.49			
564	16.14	2.34	0.69	12.37	11.00	10.42			
565				11.33	10.52	9.98			439
566	17.06	2.13	0.96	12.90	11.96	11.71			
567				12.56	11.52	10.96			500
568				13.32	12.17	11.47			524
569	15.12	1.43	0.70	12.91	12.00	11.73			
570				13.58	13.50	13.33			
571	15.07	1.44	0.62	13.36	11.94	11.07			405
572	15.65	1.22	1.17	13.73	12.60	12.04			
573	15.66	1.34	0.62	13.45	12.54	12.27			
574				14.78	13.67	13.21			
575	16.89	1.88	0.97	14.92	14.31	13.99			487
576	15.22	1.50	0.65	12.62	11.72	11.35			
577				16.15	15.14	14.67			
578				13.74	13.15	12.88			
579				11.73	11.48	11.39			
580	17.36	1.70	0.55	17.10	15.97	15.38			
581	17.70	2.30	1.12	14.97	14.03	13.65			
582	16.47	2.31	0.34	12.71	11.31	10.72			
583	17.15	1.29	0.47	11.80	10.89	10.39			374
584	17.19	2.01	0.89	14.54	13.59	13.18			
585				14.95	13.82	13.37			501
586				11.64	11.37	11.29			501
587				13.71	12.38	11.78			514
588				7.13	6.86	6.54			402
589	18.15	1.62	0.69	15.91	14.99	14.35			
590	15.80	1.23	0.57	13.86	13.04	12.75			
591	15.87	1.67	0.64	13.25	12.21	11.89			
592				13.59	12.40	11.95			
593	16.94	2.26	0.78	13.90	12.86	12.42			
594				16.53	15.67	15.32			
595									564
596	15.88	1.28	1.45	13.20	12.21	11.73			413
597	16.77	1.79	0.77	14.04	12.92	12.51			
598	16.31	1.64	0.86	14.52	13.94	13.67			
599	16.30	1.59	1.11	14.00	12.90	12.20			341
600	16.19	1.66	0.73	13.68	12.54	12.04			556
601				12.75	11.37	10.58			605
602	15.85	1.56	0.59	13.53	12.55	12.20			

Table 4. continued.

X-ray no.	<i>i</i>	<i>r</i> − <i>i</i>	<i>r</i> − <i>Hα</i>	<i>J</i>	<i>H</i>	<i>K</i>	IR excess	<i>Hα</i> excess	RGS11 number
603	15.98	1.48	0.63	13.77	12.89	12.55			
604									
605	16.72	2.12	0.91	14.04	13.01	12.63			
606				20.29	18.47	18.10			
607	17.71	1.61	0.88	14.49	13.32	12.75			397
608	17.19	1.85	0.64	14.37	13.33	12.83			421
609				15.64	13.77	12.75			
610				13.35	12.05	11.36			547
611	15.57	1.82	0.62	12.52	11.33	10.91			
612	16.01	2.81	0.72	16.10	13.16	11.40			
613	16.42	1.92	0.72	13.31	12.18	11.77			
614				14.20	13.27	12.98			
615	15.92	1.64	0.55	12.84	11.99	11.75			
616				16.12	15.06	14.47			
617	15.93	1.94	0.76	12.79	11.62	11.07			461
618				15.22	13.72	13.05			
619	17.37	1.73	0.83	14.66	13.61	13.19			
620				12.02	11.10	10.75			
621	14.75	1.14	0.64	13.34	12.63	12.45			
622	16.82	1.70	0.64	14.20	13.16	12.76			
623	14.58	1.53	0.55	12.35	11.54	11.22			
624				14.17	12.80	12.21			
625				11.01	10.71	10.65			
626									
627	14.86	1.90	0.66	11.92	10.77	10.35			
628	15.96	1.67	0.68	13.30	12.25	11.88			
629				8.28	7.84	7.64			
630				10.96	10.63	10.52			
631				12.39	11.13	10.52			563
632	16.60	2.07	0.64	13.57	12.29	11.85			
633	14.33	1.57	0.61	11.88	10.88	10.58			
634				14.87	13.28	12.41			
635	17.05	2.13	0.72	13.89	12.80	12.34			
636				15.35	13.95	13.36			
637	15.18	1.61	0.60	12.77	11.72	11.38			
638	16.80	2.58	0.66	12.48	10.86	10.25			
639	16.87	1.89	0.62	13.77	12.58	12.15			
640	17.60	1.44	0.58	12.88	11.82	11.38			515
641				13.34	12.57	12.21			
642	16.14	1.99	0.65	11.21	10.35	10.01			
643				9.47	9.39	9.36			
644	16.58	2.14	0.81	13.55	12.45	12.02			
645	17.08	1.66	0.44	13.10	11.58	10.97			

Table 4. continued.

X-ray no.	<i>i</i>	<i>r</i> − <i>i</i>	<i>r</i> − <i>Hα</i>	<i>J</i>	<i>H</i>	<i>K</i>	IR excess	<i>Hα</i> excess	RGS11 number
646	16.30	1.80	0.70	13.50	12.33	11.86			
647	15.94	2.06	0.53	12.41	11.19	10.59			
648	17.25	1.55	0.66	16.69	15.50	14.93			
649	17.96	1.34	0.76	17.20	15.43	14.67	Y		
650									
651				13.68	12.68	12.30			626
652	16.06	1.82	0.74	14.80	13.52	12.97			656
653									
654	15.25	1.30	0.90	13.07	12.02	11.31			
655							Y		
656									
657				16.65	15.26	14.57			
658				16.12	15.38	15.02			
659	15.97	1.84	0.74	13.05	11.88	11.41			
660				16.28	14.57	13.85			
661	15.32	1.69	0.64	12.87	11.85	11.50			
662	15.23	1.54	0.73	12.71	11.59	10.98			203
663				16.06	14.93	14.37			
664				11.06	10.37	10.02			
665	17.05	2.06	0.86	13.52	12.14	11.38			193
666	16.99	1.81	1.05	15.30	14.71	14.42			
667				16.51	15.97	15.71			248
668				14.20	12.71	11.88			159
669	16.13	1.45	0.43	16.13	15.15	14.78			
670				10.86	10.28	10.18			
671									
672				18.72	17.01	16.30			
673				17.11	16.00	15.50			
674				17.75	16.30	15.65			
675				15.96	13.94	12.77			229
676				15.93	15.07	14.64			
677				16.26	15.26	15.03			
678				11.52	11.26	11.24			
679				16.52	15.36	14.80			
680				16.42	15.36	14.87			
681				16.41	15.44	15.00			
682				15.23	12.52	11.01			289
683				15.93	13.46	12.33			
684				11.75	11.42	11.36			
685				16.61	15.65	15.21			
686	15.83	1.83	0.96	14.07	13.49	13.23			
687				9.14	8.89	8.87			
688	17.57	1.73	0.52	17.55	15.56	14.66	Y		

Table 4. continued.

X-ray no.	<i>i</i>	<i>r</i> − <i>i</i>	<i>r</i> − <i>Hα</i>	<i>J</i>	<i>H</i>	<i>K</i>	IR excess	<i>Hα</i> excess	RGS11 number
689	14.24	12.69							
690									267
691	19.32	17.86	17.54						
692	18.36	16.96	16.40						
693	14.35	12.80	12.19						
694	16.93	1.87	1.05	15.23	14.62	14.34			
695				10.30	9.88	9.74			
696	17.10	14.02	12.30						244
697				11.02	10.70	10.62			
698	15.74	0.93	0.46	20.64	16.79	14.98	Y		
699	15.17	0.95	0.54	16.24	14.61	13.88	Y		
700	15.43	1.72	0.90	13.61	13.02	12.76			
701				12.15	11.49	11.25	347		
702				16.71	13.86	12.17	240		
703				17.29	15.14	14.17			
704				16.33	13.81	12.65			
705	12.74	0.51	0.33						
706				12.53	11.88	11.64			
707				17.09	15.93	15.40			
708				14.69	14.13	13.89	108		
709							155		
710									
711				17.60	16.52	16.07			
712	15.50	1.98	0.99	13.60	13.06	12.77			
713	16.60	2.02	0.99	14.66	14.10	13.79			
714				17.49	15.86	15.15			
715				16.86	15.07	14.28			
716	17.33	2.02	1.00	15.32	14.72	14.42			
717				11.92	11.50	11.41			
718	15.30	1.01	0.59	14.02	13.34	13.15			
719	12.21	1.76	0.88	10.45	9.87	9.59			
720	16.46	1.34	0.35	15.90	15.10	14.67			
721	17.10	1.49	0.45	14.90	14.15	13.84			